MACHINE AUGMENTED COMPOSITE MATERIALS FOR DAMPING PURPOSES

A Thesis

by

DAVID MATTHEW MCCUTCHEON

Submitted to the Office of Graduate Studies of
Texas A&M University
in partial fulfillment of the requirements for the degree of

MASTER OF SCIENCE

December 2004

Major Subject: Mechanical Engineering

MACHINE AUGMENTED COMPOSITE MATERIALS FOR DAMPING PURPOSES

A Thesis

by

DAVID MATTHEW MCCUTCHEON

Submitted to the Office of Graduate Studies of
Texas A&M University
in partial fulfillment of the requirements for the degree of

MASTER OF SCIENCE

Approved as to style and content by:

J. N. Reddy (Co-Chair of Committee)	William Perry (Member)
Terry Creasy (Co-Chair of Committee)	Dennis O'Neal (Head of Department)

December 2004

Major Subject: Mechanical Engineering

ABSTRACT

Machine Augmented Composite Materials for Damping Purposes. (December 2004)

David Matthew McCutcheon, B.S., Arkansas Tech University

Co-Chairs of Advisory Committee: Dr. J. N. Reddy
Dr. Terry Creasy

In this study the energy dissipation performance of machine augmented composite (MAC) materials is investigated. MAC materials are formed by inserting simple machines into a matrix material. In this work the machines take the form of fluid filled tubes, and the tube cross-sectional geometry induces fluid flow when it is deformed in its plane. This flow dissipates mechanical energy, and thus provides the composite material with attractive damping properties. The objective of this study is to gain insight into the geometry, the material property combinations, and the boundary conditions that are effective in producing high damping MAC materials. Particular attention is given to tube geometry and to dimensionless parameters that govern the energy dissipation efficiency of a MAC lamina. An important dimensionless parameter is the ratio of solid elastic moduli to the product of the driving frequency and the fluid dynamic viscosity. This is a measure of the ratio of elastic forces in the solid material to the viscous forces in the fluid material that makes up a MAC lamina. Governing equations and simulation methods are discussed. Simplified equations are derived to predict the pressure generated when a tube/matrix cell is squeezed with zero pressure end conditions. Transient, three dimensional finite element models are also used to predict the performance of the damping MAC materials with zero pressure at the ends of the tubes. For the geometry and material properties considered, the highest energy dissipation efficiency predicted by these models is approximately 0.8 out of a maximum of 1.0.

TABLE OF CONTENTS

Page

Page

LIST OF FIGURES

FIGURE Page

FIGURE Page

FIGURE Page

FIGURE Page

LIST OF TABLES

TABLE Page

1. INTRODUCTION

1.1. Overview

The machine augmented composite (MAC) is a new class of material. Hawkins [1] first introduced these materials. In MAC materials conventional fiber and particulate reinforcements are replaced by embedded simple machines. The machines may take on many different forms and serve to modify power, force, or motion in different ways. Also, a given composite lamina may contain multiple types of simple machines. Alternatively, lamina containing only one type of simple machine may be stacked to form composite laminates. These methods may also be used in conjunction. This flexibility allows for the development of composite materials that possess multifunctional properties. Multifunctional materials are those that accomplish multiple performance objectives in a single system.

Most conventional structural materials do not simultaneously possess good damping properties, high stiffness, high strength, and low density. For example, most metals have high stiffness and strength, but they are also very dense. In addition, many metals do not possess attractive damping properties. On the other hand, common elastomers possess good damping characteristics and low density, but they have relatively low stiffness and strength. Conventional composite materials have large stiffness to density ratios, but many lack good damping properties. This lack of multifunctionality in common materials is why there is a need to study and develop new material systems such as MAC materials.

The mechanical response of linearly viscoelastic materials subjected to one dimensional, sinusoidal excitation can be described by the use of a single complex modulus or stiffness. The complex stiffness consists of a real part and an imaginary part. The real part is referred to as the storage modulus, and the imaginary part is referred to

---

This thesis follows the style and format of the *International Journal of Numerical Methods in Engineering.*

as the loss modulus. For a purely elastic material, the loss modulus is zero. Conversely, for a purely viscous material, the storage modulus is zero. If a sinusoidal strain is applied to a linearly viscoelastic material, a sinusoidal stress is produced that leads the applied strain by a phase angle (δ). The converse is also true. If a sinusoidal stress is applied to a linearly viscoelastic material, a sinusoidal strain is produced that lags the applied stress by a phase angle (δ). The tangent of the phase angle (tan δ) is referred to as the loss factor or loss tangent and represents the ratio of the loss modulus to the storage modulus [2]. The magnitude of the complex stiffness is determined by computing the square root of the sum of the squares of the storage modulus and the loss modulus.

1.2. Objective

The development MAC materials that exhibit good damping properties, high stiffness, high strength, and low density is desired. The method by which this is to be accomplished is by inserting simple machines, which take the form of long tubes filled with viscous fluid, into a matrix material. The tube cross sectional geometry is specially designed to induce substantial fluid flow when the tubes are squeezed or compressed. Incompressible or nearly incompressible matrix material is used in order to maximize the volume change of the tube cavities. The tube material may need to possess high ductility to accommodate large strains that cause the displacement of a large quantity of viscous fluid.

Before multifunctional MAC materials can be designed and produced, the physics governing the interaction of the different materials making up a MAC material lamina must be thoroughly understood. The objective of this study is to gain insight into the dependence of MAC material mechanical properties on tube geometry, tube configuration, MAC lamina loading, and the material properties of the MAC material constituents. This is accomplished by numerical tests and parametric studies carried out using the finite element method.

1.3. Literature Review

1.3.1. Material Performance

The tan δ, often referred to as the loss tangent [2], and the specific damping capacity are commonly used measures of a linearly viscoelastic material's ability to dissipate energy. Lee and Hartman [3] derived the relationship between two definitions of specific damping capacity and the loss angle (δ) for arbitrary large δ. However, the relationships are only valid for sinusoidal stress and strain that oscillate about zero. They point out that the most common way by which specific damping capacity is determined is by a calculation based on a measured value of loss angle. The authors found that the mathematical relationship most commonly used is only accurate for loss angle values less than 0.01 radians. They also suggest a new definition for specific damping capacity. The most commonly used definition is the ratio of energy dissipated to the maximum energy stored through one cycle of harmonic excitation. The proposed definition is the ratio of energy dissipated to work done (energy input) per cycle.

It is desirable for a structural material to possess both high stiffness and high loss tangent. Chen and Lakes [4] and Brodt and Lakes [5] predicted the complex stiffness and tan δ of various types of composite materials that consist of two linearly viscoelastic constituents. They used the correspondence principle of linear viscoelasticity to modify previous results obtained for linear elastic constituents. They compared results by the position of the predicted effective material properties on a stiffness-loss map. The larger the product of the magnitude of a composite material's complex stiffness and tan δ, the more effective the material is in structural applications. Their results show that Reuss type composites consisting of a stiff, low loss phase and a compliant, high loss phase exhibit both high stiffness and high loss. For best results a small volume fraction of high loss phase should be used with a high stiffness phase. Figure 1.1 depicts an example of a stiffness-loss map, which was produced by Lakes [6], for various types of composite materials. Figure 1.2 is a stiffness-loss map, which was produced by Lakes, showing the positions held by various materials.

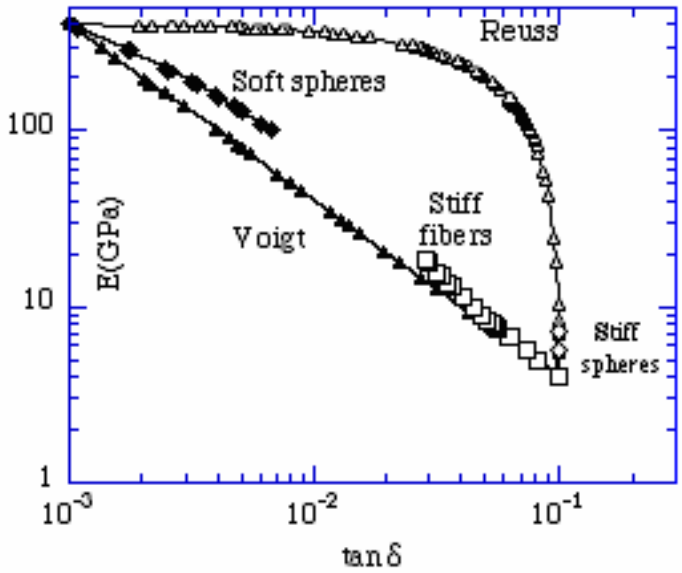

Figure 1.1. Stiffness-loss map for various types of composite materials (Printed with permission from R. S. Lakes [6]).

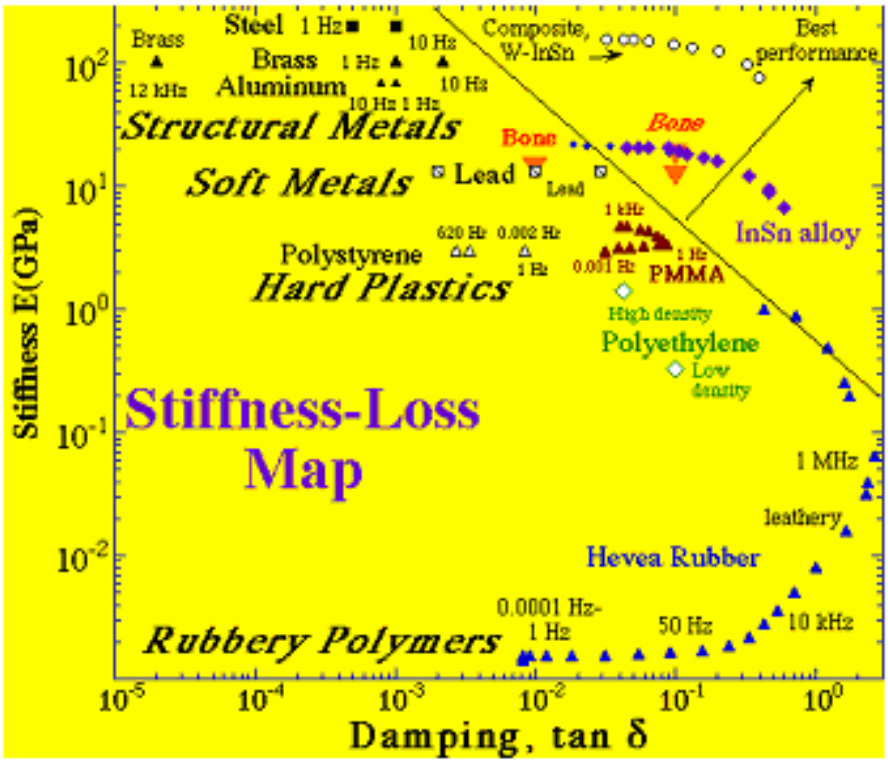

Figure 1.2. Stiffness-loss map with values for various materials plotted (Printed with permission from R. S. Lakes [6]).

1.3.2. Fluid-Structure Interaction Problem Solution Methods

Fluid-structure interaction (FSI) between the viscous fluid and the elastic tube in a MAC material is a complex multi-physics problem. This type of problem is also referred to as a coupled field problem. Numerical techniques such as finite element, boundary element, finite difference, or finite volume methods are often used in conjunction with mesh partitioning to obtain approximate solutions of fluid-structure interaction problems. Different numerical methods might be used for the solid domain and the fluid domain. For example, the finite element method might be used for the solid domain while the finite volume method might be used for the fluid domain. Felippa et al. [7] provide a tutorial article that reviews the use of partitioned analysis for several coupled mechanical systems. Deparis et al. [8] outline a fixed point algorithm that combines Block-Gauss-Seidel iterations with a transpiration formulation. The structural domain was modeled with a Lagrangian formulation, and the fluid domain was modeled with an arbitrary Lagrangian–Eulerian formulation. Their results show that this method is much more efficient than other commonly used methods.

Kuhl et al. [9] outlined an arbitrary Lagrangian–Eulerian finite element formulation for fluid-structure interaction problems. The generalized α-method is used for the time derivatives of the fluid and structural differential equations. This is an implicit finite difference method. The formulation carries nodal velocities as primary degrees of freedom for both the fluid and structural domain in order to ease coupling of the two domains.

Fluid flow in collapsible tubes is related to the mechanism by which damping is introduced into (MAC) materials. Heil [10] performed analysis and experiments concerning viscous flow in elastic tubes. The work focused on the flow field and structural deformation occurring when a negative fluid pressure causes an elastic tube to collapse inwardly. The fluid flow was modeled by three-dimensional Stoke's flow equations, and the structural deformation was described by geometrically nonlinear elastic shell theory. Finite element analysis was used to obtain numerical results.

Xu and Accorsi [11] discussed mesh update procedures for fluid-structure interaction problems based on a pseudo-solid model. A homogenous analysis was performed on the pseudo-solid representing the fluid mesh with prescribed boundary displacements. Then, different element properties and external forces were calculated based on the results of the prior analysis. The non-homogenous pseudo-solid model was solved with the goal of maintaining element aspect ratio while preserving element volume.

2. CONTINUUM MECHANICS OF FLUID-STRUCTURE INTERACTION

Understanding the foundations of the formulations employed in this study requires an introduction to the arbitrary Lagrangian-Eulerian (ALE) continuum mechanics that govern fluid-structure interaction. Much of the derivation below follows from Reference [12]. All derivations and computations are performed under an isothermal assumption, i.e. temperature changes are negligible.

In this study, the order of a tensor is represented by the number of arrows above a given character or the number of subscript indices following a given character. For example, $\vec{\vec{\sigma}}$ represents the same second order tensor as σ_{ij}. Einstein's summation convention is in effect unless otherwise stated.

Figure 2.1 shows three domains used in arbitrary Lagrangian-Eulerian continuum mechanics. These are the material, the reference, and the spatial (current) domains. In practice the material domain is most often the configuration of a continuum that is considered undeformed. The $\vec{X}$ coordinates are components of the position vector of a material particle in the undeformed configuration. The spatial domain is the current, deformed configuration of a continuum. The $\vec{x}$ coordinates are components of the position vector of a material particle in the deformed configuration at a given time (t). The reference domain or frame can be chosen arbitrarily, and computations that use a reference frame that is neither material nor spatial are referred to as arbitrary Lagrangian-Eulerian formulations. In ALE formulations $(\vec{\aleph}, t)$ are the independent variables. The $\vec{\aleph}$ coordinates are components of the position vector of a material particle in the reference configuration. The three coordinates are related by the mapping functions shown in Figure 2.1. Each mapping is assumed to be one-to-one, continuous, invertible, and to have continuous derivatives up to the necessary order.

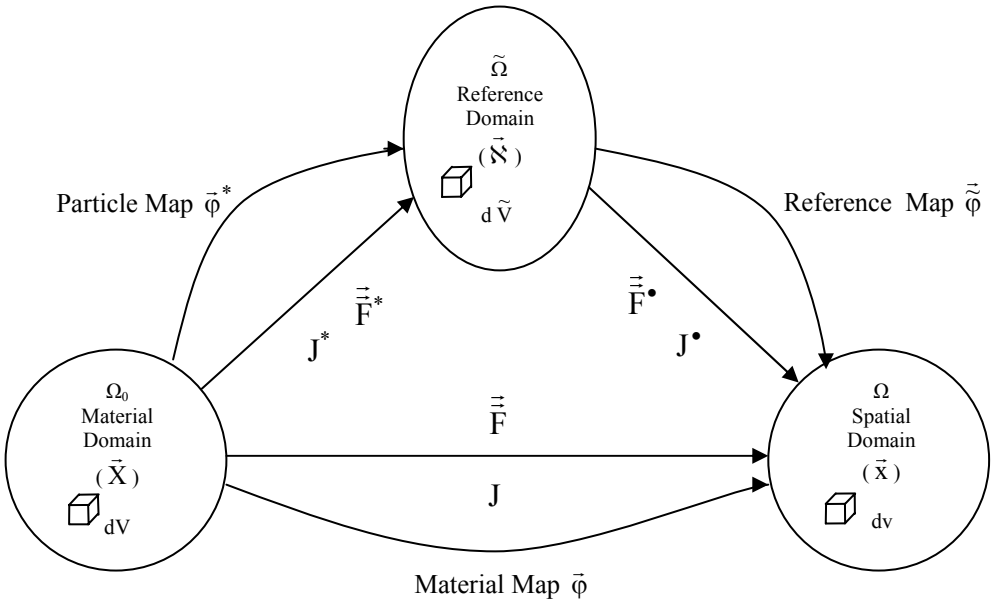

Figure 2.1. Material, reference, and spatial domains and mappings.

Lagrangian and Eulerian formulations are special cases of ALE formulations. For structural computations, Lagrangian formulations are commonly used. Lagrangian formulations use $(\vec{X}, t)$ as independent variables. Therefore, the reference coordinate is equal to the material coordinate ($\vec{\aleph} = \vec{X}$).

For fluid flow computations, Eulerian formulations are commonly used. Eulerian formulations use $(\vec{x}, t)$ as independent variables. Therefore, the reference coordinate is equal to the spatial coordinate ($\vec{\aleph} = \vec{x}$). In fluid-structure interaction problems, a purely Eulerian formulation for the fluid computation suffers because the boundaries of the fluid domain deform when the structure deforms. The ALE formulation is very useful in this situation.

For this discussion the symbols $\vec{\nabla}_X$, $\vec{\nabla}_{\aleph}$, and $\vec{\nabla}_x$ represent the gradient operator in terms of the material, the reference, and the spatial coordinates respectively. The tensor $\vec{\vec{F}}$ represents the gradient of spatial coordinates with respect to material coordinates.

The tensor $\vec{\vec{F}}^{*}$ represents the gradient of reference coordinates with respect to material coordinates, and the tensor $\vec{\vec{F}}^{\bullet}$ represents the gradient of spatial coordinates with respect to reference coordinates. The symbols J, J^{*}, and $J^{\bullet}$ represent the determinants of $\vec{\vec{F}}$, $\vec{\vec{F}}^{*}$, and $\vec{\vec{F}}^{\bullet}$. Also, subscripts used in partial derivatives indicate the derivative is taken with the subscript variable held constant.

Equation (2.1) describes the material motion. Since numerical analysis is used in this study, it is assumed that a grid or mesh exists. The mesh motion is described by Equation (2.2). The reference coordinate mapping is described by Equation (2.3).

$$\vec{x} = \vec{\varphi}(\vec{X}, t) \tag{2.1}$$

$$\vec{x} = \vec{\tilde{\varphi}}(\vec{\aleph}, t) \tag{2.2}$$

$$\vec{\aleph} = \vec{\varphi}^{*}(\vec{X}, t) = \vec{\tilde{\varphi}}^{-1}(\vec{\varphi}(\vec{X}, t), t) = \vec{\tilde{\varphi}}^{-1}(\vec{x}, t) \tag{2.3}$$

The mesh displacements ($\vec{\tilde{u}}$), mesh velocities ($\vec{\tilde{v}}$), and mesh accelerations ($\vec{\tilde{a}}$) are given by Equations (2.4), (2.5), and (2.6) respectively.

$$\vec{\tilde{u}} = \vec{x} - \vec{\aleph} = \vec{\tilde{\varphi}}(\vec{\aleph}, t) - \vec{\aleph} \tag{2.4}$$

$$\vec{\tilde{v}} = \frac{\partial_{\aleph} \vec{\tilde{u}}(\vec{\aleph}, t)}{\partial t} = \frac{\partial_{\aleph} \vec{\tilde{\varphi}}(\vec{\aleph}, t)}{\partial t} \tag{2.5}$$

$$\vec{\tilde{a}} = \frac{\partial^{2}_{\aleph} \vec{\tilde{u}}(\vec{\aleph}, t)}{\partial t^{2}} = \frac{\partial_{\aleph} \vec{\tilde{v}}(\vec{\aleph}, t)}{\partial t} \tag{2.6}$$

The material displacement and velocity are given by Equations (2.7) and (2.8) respectively.

$$\vec{u} = \vec{x} - \vec{X} \tag{2.7}$$

$$v_i = \frac{\partial_X (x_i(\vec{X},t) - X_i)}{\partial t} = \frac{\partial_{\aleph} \tilde{\varphi}_i(\vec{\aleph},t)}{\partial t} + \frac{\partial \tilde{\varphi}_i(\vec{\aleph},t)}{\partial \aleph_j} \frac{\partial_X \varphi_j^*(\vec{X},t)}{\partial t} \tag{2.8}$$

The convective velocity of material through the mesh is given by Equation (2.9). This form is obtained by using Equations (2.5) and (2.8).

$$c_i = v_i - \tilde{v}_i = \frac{\partial x_i(\vec{\aleph},t)}{\partial \aleph_j} \frac{\partial_X \aleph_j(\vec{X},t)}{\partial t} \tag{2.9}$$

The equations needed to form a material time derivative containing a spatial gradient of a function $\bullet(\vec{\aleph},t)$ are shown in Equations (2.10)-(2.11). These equations are used in the development of the material acceleration needed for the equations for conservation of linear momentum.

$$\frac{D(\bullet)}{Dt} = \frac{\partial_{\aleph}(\bullet)}{\partial t} + \frac{\partial(\bullet)}{\partial \aleph_i} \frac{\partial_X \aleph_i}{\partial t} \tag{2.10}$$

$$\frac{\partial(\bullet(\vec{\aleph},t))}{\partial \aleph_i} \frac{\partial_X \aleph_i}{\partial t} = \frac{\partial(\bullet(\vec{\tilde{\varphi}}^{-1}(\vec{x},t),t))}{\partial x_j} \frac{\partial x_j}{\partial \aleph_i} \frac{\partial_X \aleph_i}{\partial t} = \frac{\partial(\bullet)}{\partial x_j} c_j = \vec{c} \cdot \vec{\nabla}_x(\bullet) \tag{2.11}$$

Suppose that a continuum containing both solid and fluid regions is described by the domains Ω_0, $\tilde{\Omega}$, and Ω and the boundaries Γ_0, $\tilde{\Gamma}$, and Γ. The domain Ω is the union of Ω_s and Ω_f. The symbols Ω_s and Ω_f represent the spatial domains of solid and

fluid continua respectively. Definitions of Ω_0 and $\widetilde{\Omega}$ follow the same logic. The boundary Γ is the union of Γ_s and Γ_f less their intersection ($\Gamma_{s\cap f}$). The symbols Γ_s and Γ_f represent the spatial boundaries of solid and fluid continua respectively. Definitions of Γ_0 and $\widetilde{\Gamma}$ follow the same logic. The solid and fluid domains may contain additional sub-domains, such as areas with different material properties. The previously discussed relations are summarized in Equations (2.12)-(2.17).

$$\Omega_0 = \Omega_{0s} \cup \Omega_{0f} \tag{2.12}$$

$$\widetilde{\Omega} = \widetilde{\Omega}_s \cup \widetilde{\Omega}_f \tag{2.13}$$

$$\Omega = \Omega_s \cup \Omega_f \tag{2.14}$$

$$\Gamma_0 = \left(\Gamma_{0s} \cup \Gamma_{0f}\right) \setminus \left(\Gamma_{0s} \cap \Gamma_{0f}\right) \tag{2.15}$$

$$\widetilde{\Gamma} = \left(\widetilde{\Gamma}_s \cup \widetilde{\Gamma}_f\right) \setminus \left(\widetilde{\Gamma}_s \cap \widetilde{\Gamma}_f\right) \tag{2.16}$$

$$\Gamma = \left(\Gamma_s \cup \Gamma_f\right) \setminus \left(\Gamma_s \cap \Gamma_f\right) \tag{2.17}$$

2.1 Governing Equations for Lagrangian Description of Solid Continuum

The governing continuity equation for the Lagrangian description is Equation (2.18). Here, ρ is the current material density, and ρ_0 is the initial material density.

$$\rho J = \rho_0 \tag{2.18}$$

The differential equation governing conservation of linear momentum for the Lagrangian description is Equation (2.19). This equation may be pushed forward to

contain spatial derivatives. This version is given as Equation (2.20). Although this version contains spatial derivatives, the formulation is still Lagrangian since the deformation and strain are measured in reference to the material coordinates.

$$\rho_0 \frac{\partial^2 \vec{u}}{\partial t^2} = \vec{\nabla}_X \cdot \vec{\vec{P}} + \rho_0 \vec{f} \quad \text{In} \quad \Omega_{0s} \tag{2.19}$$

$$\rho \frac{\partial^2 \vec{u}}{\partial t^2} = \vec{\nabla}_x \cdot \vec{\vec{\sigma}} + \rho \vec{f} \quad \text{In} \quad \Omega_s \tag{2.20}$$

Formulations using Equation (2.19) are called total Lagrangian formulations, and formulations using Equation (2.20) are called updated Lagrangian formulations. The symbol $\vec{f}$ represents a vector-valued function of body forces per unit mass. The tensors $\vec{\vec{P}}$ and $\vec{\vec{\sigma}}$ represent the first Piola-Kirchhoff stress tensor and the Cauchy stress tensor respectively. The first Piola-Kirchhoff stress tenor can be interpreted as the current force per unit of undeformed area. Since this tensor relates quantities in the material configuration to quantities in the spatial configuration, it is known as a two point tensor [13]. The Cauchy stress tensor can be interpreted as the current force per unit deformed area or true stress. The first Piola-Kirchhoff stress tensor in Equation (2.19) is often replaced by the definition given by Equation (2.21) [12]. Here, $\vec{\vec{S}}$ is the second Piola-Kirchhoff stress tensor and can be interpreted as the material force per unit of undeformed area. This substitution is convenient because the second Piola-Kirchhoff stress tensor is symmetric, while the first Piola-Kirchhoff stress tensor in not. Also, many hyperelastic constitutive equations are given in terms of the second Piola-Kirchhoff stress tensor.

$$P_{ij} = S_{ik} F_{kj}^T \tag{2.21}$$

Two solid material constitutive models are used in this study for situations with large deformations. The polymer tube material is modeled as a Saint Venant-Kirchhoff material. The elastomer matrix material is modeled as a Neo-Hookean material. The constitutive equations for these material models are described below.

The Saint Venant-Kirchhoff material model is a linear hyperelastic model that is useful in dealing with small strains and large rotations [12]. The constitutive equation is given by Equation (2.22).

$$S_{ij} = C_{ijkl} E_{kl} \tag{2.22}$$

Here, $\vec{\vec{S}}$ is the second Piola-Kirchhoff stress tensor, $\vec{\vec{\vec{\vec{C}}}}$ is the fourth order elasticity tensor containing elastic moduli in the undeformed configuration, and $\vec{\vec{E}}$ is the Green-Lagrange strain. The Green-Lagrange strain is related to the deformation gradient $\vec{\vec{F}}$ as shown by Equation (2.23) [12]. Also, $\vec{\vec{\delta}}$ is the Kroneker Delta.

$$E_{ij} = \frac{1}{2}\left(F_{ik}^{T} F_{kj} - \delta_{ij}\right) = \frac{1}{2}\left(\frac{\partial u_i}{\partial X_j} + \frac{\partial u_j}{\partial X_i} + \frac{\partial u_k}{\partial X_i}\frac{\partial u_k}{\partial X_j}\right) \tag{2.23}$$

The Neo-Hookean material model is a nonlinear hyperelastic model that is useful in dealing with small to moderate deformations of elastomers. The constitutive equation for this material model is described by Equations (2.24)-(2.26) (see [12]).

$$S_{ij} = \lambda_0 \ln(J) c_{ij}^{-1} + G_0\left(\delta_{ij} + c_{ij}^{-1}\right) = C_{ijkl} E_{kl} \tag{2.24}$$

$$C_{ijkl} = \lambda_0 c_{ij}^{-1} c_{kl}^{-1} + \left(G_0 - \lambda_0 \ln(J)\right)\left(c_{ik}^{-1} c_{jl}^{-1} + c_{il}^{-1} c_{kj}^{-1}\right) \tag{2.25}$$

$$c_{ij} = F_{ik}^{T} F_{kj} = \left(\frac{\partial u_i}{\partial X_j} + \frac{\partial u_j}{\partial X_i} + \frac{\partial u_k}{\partial X_i} \frac{\partial u_k}{\partial X_j} + \delta_{ij} \right) \tag{2.26}$$

Here, $\vec{\vec{c}}$ is the right Cauchy-Green deformation tensor, $\vec{\vec{\vec{\vec{C}}}}$ is the fourth order elasticity tensor containing nonlinear elastic moduli. The symbol λ_0 represents the Lame constant of the material in the undeformed configuration, and G_0 is the shear modulus of the material in the undeformed configuration.

2.2. Governing Equations for ALE Description of Fluid Continuum

Equation (2.27) is the continuity equation governing the flow of an incompressible fluid [12]. This equation enforces that the velocity field is divergence free. The differential equation governing conservation of linear momentum for an ALE formulation is given as Equation (2.28) [12]. The only difference between this equation and that of the Eulerian formulation is the appearance of the convective velocity in the material time derivative.

$$\vec{\nabla}_x \cdot \vec{v} = 0 \quad \text{In} \quad \Omega_f \tag{2.27}$$

$$\rho \left(\frac{\partial_{\mathcal{N}} \vec{v}}{\partial t} + (\vec{c}) \cdot \vec{\nabla}_x \vec{v} \right) = \vec{\nabla}_x \cdot \vec{\vec{\sigma}} + \rho \vec{f} \quad \text{In} \quad \Omega_f \tag{2.28}$$

The constitutive equation for an incompressible Newtonian fluid is given by Equation (2.29).

$$\sigma_{ij} = 2\mu e_{ij} - p\delta_{ij} \tag{2.29}$$

Here, $\vec{\vec{e}}$ is the strain rate tensor and is defined by Equation (2.30), μ is the dynamic viscosity of the fluid, and p is the fluid pressure. When Equation (2.29) and Equation

(2.30) are substituted into Equation (2.28), the ALE form of the Navier-Stokes equations for an incompressible Newtonian fluid are formed.

$$e_{ij} = \frac{1}{2}\left(\frac{\partial v_i}{\partial x_j} + \frac{\partial v_j}{\partial x_i} \right) \tag{2.30}$$

2.3. Fluid-Solid Interfaces

Finally, the fluid and structure domains are coupled through their common interfaces, i.e. a motion of the solid interface causes motion of the fluid interface. When the no-slip boundary condition is assumed, continuity of both normal and tangential velocity components is enforced. This is shown by Equation (2.31). Also, the traction vectors acting on the fluid side of the fluid-solid interface are balanced by equal but opposite traction vectors acting on the solid side of the fluid-solid interface. This is shown by Equation (2.32). Here, $\vec{n}^{Solid}$ and $\vec{n}^{Fluid}$ are the unit outward normal vectors to the solid and fluid interfaces respectively.

$$v_i^{Solid} = v_i^{Fluid} \quad \text{On} \quad \Gamma_{s \cap f} \tag{2.31}$$

$$\sigma_{ji}^{Solid} n_j^{Solid} = -\sigma_{ji}^{Fluid} n_j^{Fluid} \quad \text{On} \quad \Gamma_{s \cap f} \tag{2.32}$$

3. STUDY OF TUBE GEOMETRY

The study of the effects of tube geometry on structural behavior appears in two sections. First, finite element models are used to predict tube deformation and Von Mises stress levels as attempts are made to reduce the stress levels by changing the tube cross sectional geometry. Von Mises stress values are compared since a single value represents the effects of the entire stress tensor at a point. Second, a finite element model is used to predict the deformation and stress levels when a tube is embedded in an elastomer matrix. Two sets of matrix material properties are used.

3.1. Geometry Study of a Solitary Tube

As a starting point, it is desired to develop a tube geometry that withstands large deformations that will produce substantial fluid flow within the tube. The tube geometry should attain significant internal volume change when compressed. Therefore, a structure is proposed that has sidewalls that curve inward. The curvature makes the sidewalls deflect toward the interior of the tube when the top surface is depressed.

The study begins with a baseline geometry with alterations made to reduce stress levels produced when the tubes are depressed to make the side walls touch. ANSYS 6.1 finite element software was used to conduct a numerical study of the mechanical behavior of various tube geometries. Of interest are the magnitude and the location of maximum stresses and the amount of applied displacement needed to cause the sidewalls to touch one another. The tube geometry used for the starting point of the analysis is shown in Figure 3.1. The shape alterations studied are depicted in Figures 3.2 through 3.4. From this point forward, the numerical models corresponding to the geometries shown in Figures 3.1 through 3.4 are referred to as Models 1 through 4, respectively.

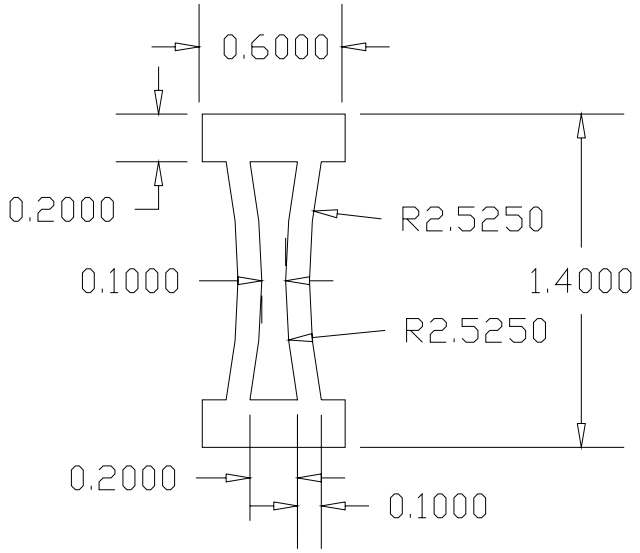

Figure 3.1. Dimensions in millimeters of the baseline (Model 1) tube geometry.

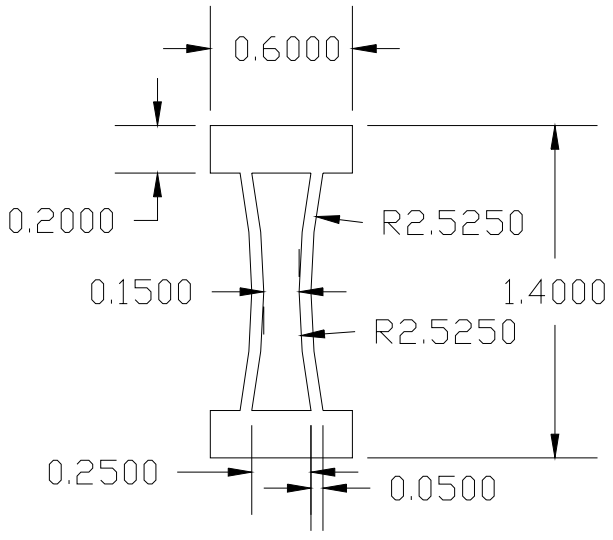

Figure 3.2. Dimensions in millimeters of the Model 2 geometry.

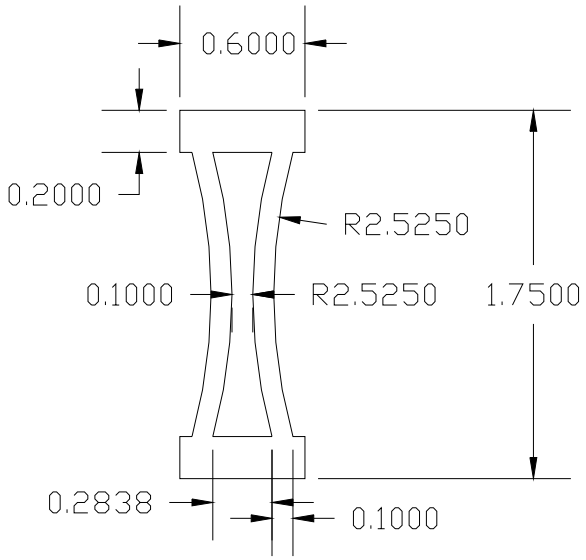

Figure 3.3. Dimensions in millimeters of the Model 3 geometry.

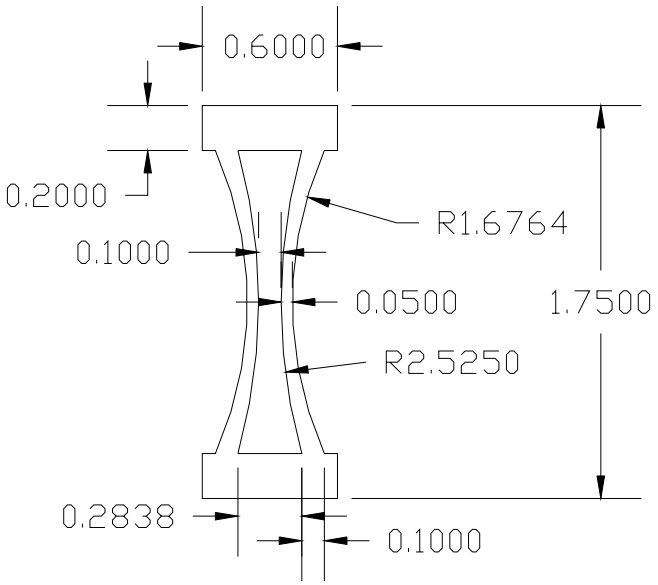

Figure 3.4. Dimensions in millimeters of Model 4 geometry.

3.1.1. Boundary Conditions

The boundary conditions used in the analysis of this section are shown in Figure 3.5. On the top surface of each 2-D model a -0.04 mm y-displacement value was used to move all nodes, and the x-displacement at the center node was set to zero. On the bottom surface of each model, the y-displacement of each node was set to zero, and the x-displacement at the center node is set to zero. Contact elements were used to line the interior of the sidewalls of the tubes to prevent the sidewalls from passing through one another. The plane strain assumption was used for each model.

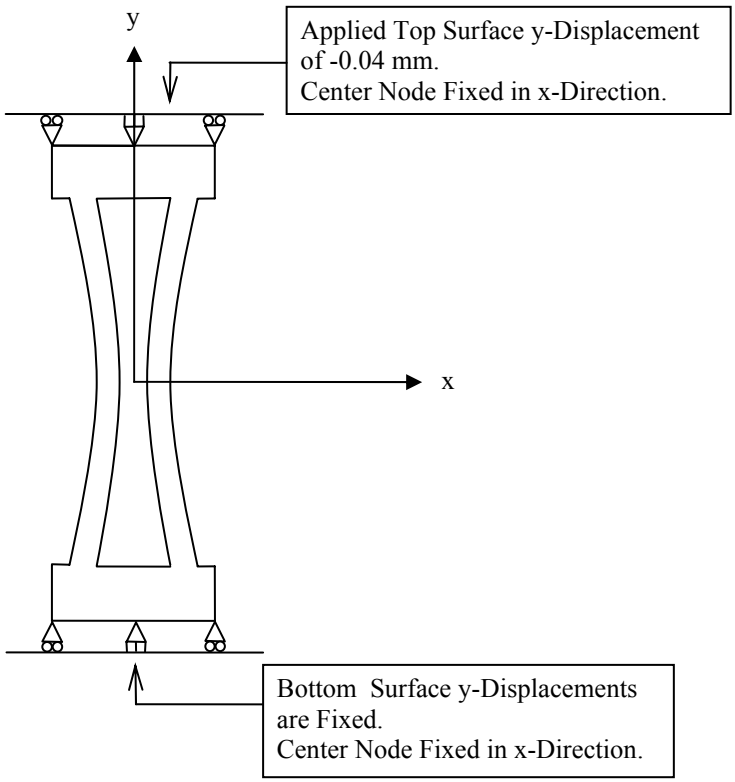

Figure 3.5. Boundary conditions used for Section 3.1.

3.1.2. Material Properties and Constitutive Models Used in the Analyses

The material properties used in the analysis of this section appear in Table 3.1. In the study, the Saint Venant-Kirchhoff constitutive model was used to represent the stress-strain relationship of the tube material. This is a linear constitutive model. The material was also assumed to be isotropic. Nonlinear geometric effects were included in the models. For information on the governing differential equations for conservation of linear momentum when this constitutive model is used, see Section 2.1.

The modulus of elasticity of the tube material is 2000 MPa and the Poisson's ratio is 0.35 for each analysis. The length unit used for the models was the millimeter. Therefore, all moduli were input in MPa. This produces momentum equations with units of N/mm^3.

Table 3.1. Material properties used in Models 1-4.

Modulus of Elasticity-E (MPa)	**Poisson's Ratio-ν**
2000	0.35

3.1.3. Element Selection

Table 3.2 shows element sketches, attributes, and the number of each type used in the finite element model. The element type that models the tube material is the PLANE42 continuum element with the plane strain option (KEYOPT (3) = 2) [14]. Extra displacement shapes were included to improve bending behavior (KEYOPT(2) = 0). With these options selected, the PLANE42 is a plane strain, 4-node quadrilateral finite element. The element uses an incompatible-modes displacement formulation that is bilinear in displacements with x- and y-displacement degrees of freedom at each node. The contact elements CONTA171 and TARGE169 model the surface-to-surface contact interaction between the tube sidewalls. These elements use an augmented Lagrangian formulation to enforce the no-penetration condition when the sidewalls touch. The augmented Lagrangian formulation can be viewed as a combination of Lagrangian multiplier and penalty parameter methods that enforces a constraint equation. Therefore,

a small amount of penetration of the contact surface into the target surface was allowed. The surface-to-surface friction coefficient was set to zero.

Table 3.2. Finite element types and attributes used in tube models.

Element Type	Number in Mesh	Number of Nodes	Degrees of Freedom	Sketch
PLANE42 KEYOPT(2)=0 KEYOPT(3)=2 Plane Strain, Displacement Formulation, Quadrilateral, Continuum Element	Model 1 2440	4	Linear x- and y-Displacements	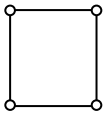
	Model 2 3500			
	Model 3 5240			
	Model 4 5280			
CONTA171 2-D Surface-to-Surface Contact Line Element		2	Linear x- and y-Displacements	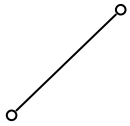
TARGE169 2-D Surface-to-Surface Target Line Element		2	Linear x- and y-Displacements	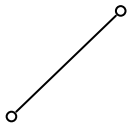

3.1.4. Numerical Results

Figure 3.6 is a contour plot of the Von Mises stress for Model 1 when the interior surfaces of the tube sidewalls first make contact with one another. The walls of the baseline shape come into contact with a top surface y-displacement of -0.035 mm. The highest stresses occur at the interior corners; see area above Location A in Figure 3.6. Location A is 0.01 mm down the inner sidewall from the corner. The high stress at the sharp tip of the inner corners is not surprising since reentrant corners tend to produce stress singularities in linearly elastic materials. The material properties used are consistent with hard, tough thermoplastic polymers such as nylon 6/6 [15]. The actual material may exhibit nonlinear behavior in the corner region that is not considered in this

model. Nonlinear stiffness reducing material behavior in this region would help relieve the high stress. Also, an actual tube corner will not be sharp, but it will have a radius, ensuring a bounded stress concentration and not a stress singularity exists. For best reliability a material with high fracture toughness should be used for the tube material. The stress at the inner corners may not be fully resolved for the models presented, but stress values a small distance away from the corners are converged. Another area of high stress is at the outer surface, half way up the vertical sidewalls; see Location B in Figure 3.6. The stress values for the baseline shape are high compared to the strength of most polymers. Since most polymers are not especially strong, keeping the maximum Von Mises stresses well below 100 MPa at Locations A and B is desirable.

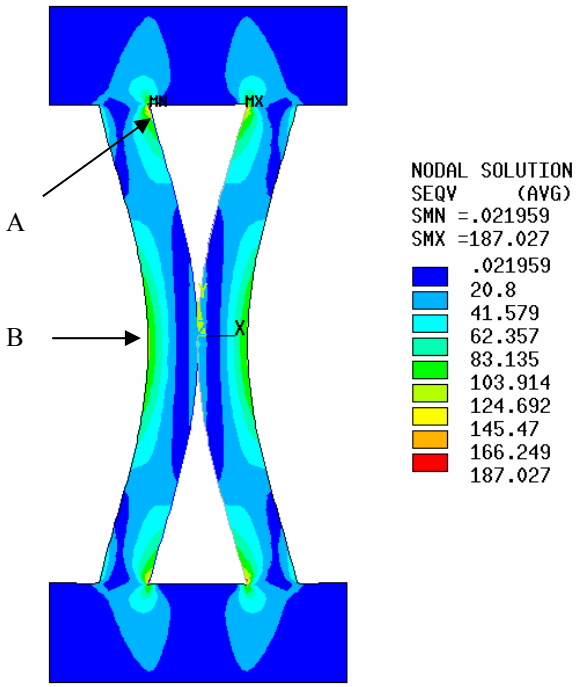

Figure 3.6. Baseline geometry Von Mises stress (MPa) for -0.035 mm displacement of top surface.

Figure 3.7 is a contour plot of the Von Mises stress for Model 2 when the interior sidewalls first contact one another. The baseline geometry was altered by halving the sidewall thickness. Contact of the sidewalls first occurs at a top surface, y-displacement of -0.035 mm, which is the same value required for contact of the sidewalls of Model 1. The same areas experience high Von Mises stresses, but the stress values at Location A and B are approximately 43% lower. The stress values are still higher than desired. Reducing the sidewall thickness lowers the tube's structural stiffness, stability, and toughness; these are adverse effects. Therefore, further geometry alterations are necessary.

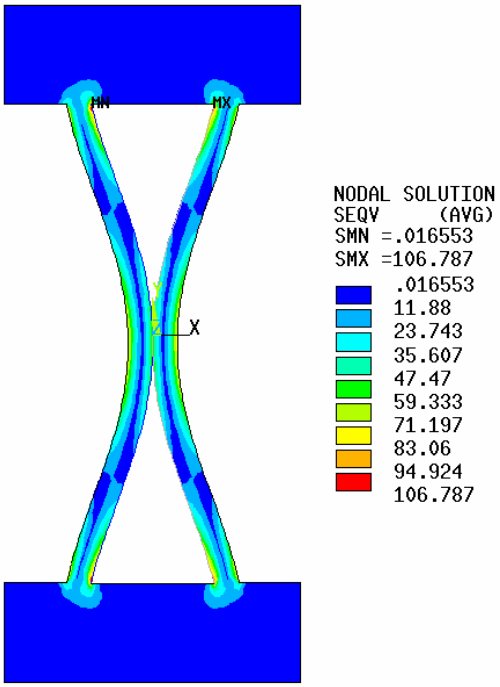

Figure 3.7. Model 2 geometry Von Mises stress (MPa) for -0.035 mm displacement of the top surface.

Figure 3.8 is a contour plot of the Von Mises stress for Model 3 when the sidewalls first contact one another. The tube height is 125% of the baseline value. The sidewall thickness and curvature match the baseline values. Contact of the sidewalls first occurs

at a top surface y-displacement of -0.030 mm. This value is less than that needed for the previous two geometries. This is partially due to the fact that the sidewalls complete more of an arc. The longer arc length causes the vertical forces acting on the sidewalls to be more eccentric when compared to the center of the sidewalls. In contrast to Model 2, the Von Mises stress at Location B is lower, but the Von Mises stress at Location A is higher. The stresses are still higher than desired.

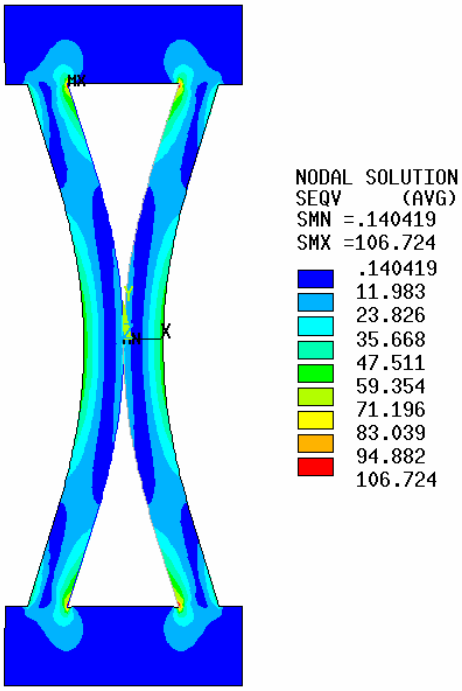

Figure 3.8. Model 3 geometry Von Mises stress (MPa) for -0.030 mm displacement of the top surface.

Figure 3.9 is a contour plot of the Von Mises stress for Model 4 when the sidewalls first contact one another. In order to produce the Model 4 geometry, the Model 3 geometry was altered by halving the thickness of the vertical sidewalls at a position half way up the walls while keeping the same sidewall base thickness. This was accomplished by reducing the radius of curvature of the outer surface of the sidewalls. Contact of the sidewalls first occurs at a top surface y-displacement of -0.025 mm. This

value is less than that of the previous geometries due to the decreased thickness of the middle of the sidewalls. The Von Mises stress values for this geometry are approximately 25% of the Von Mises stress values for the baseline geometry at Locations A and B. Also, the Von Mises stress values at Location A and Location B are of approximately the same magnitude. The highest Von Mises stress given by the model for the locations of interest up to sidewall contact is approximately 50 MPa. This value is acceptable and is a great improvement over any of the other three geometries.

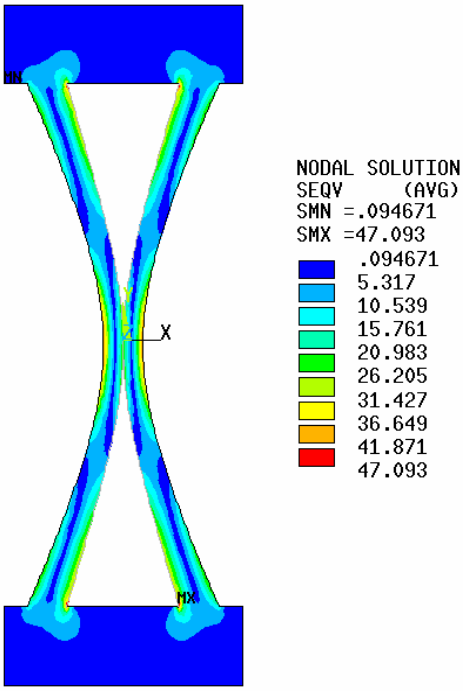

Figure 3.9. Model 4 geometry Von Mises stress (MPa) for -0.025 mm displacement of the top surface.

Stress values at Locations A and B versus top surface displacement for all four geometries appear in Figures 3.10 and 3.11. From the figures, the superiority of the geometry used in Model 4 is apparent. The Von Mises stress values shown remain relatively low even up to a top surface displacement well past that need to cause sidewall contact.

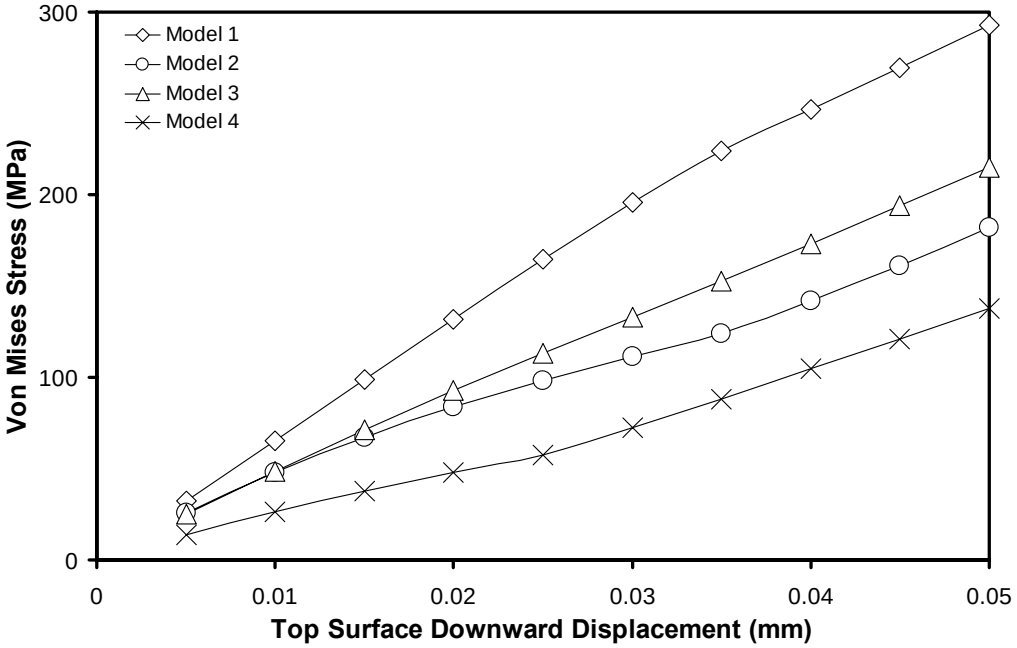

Figure 3.10. Plot of Von Mises stress at 0.01 mm down wall from top corner (LocationA).

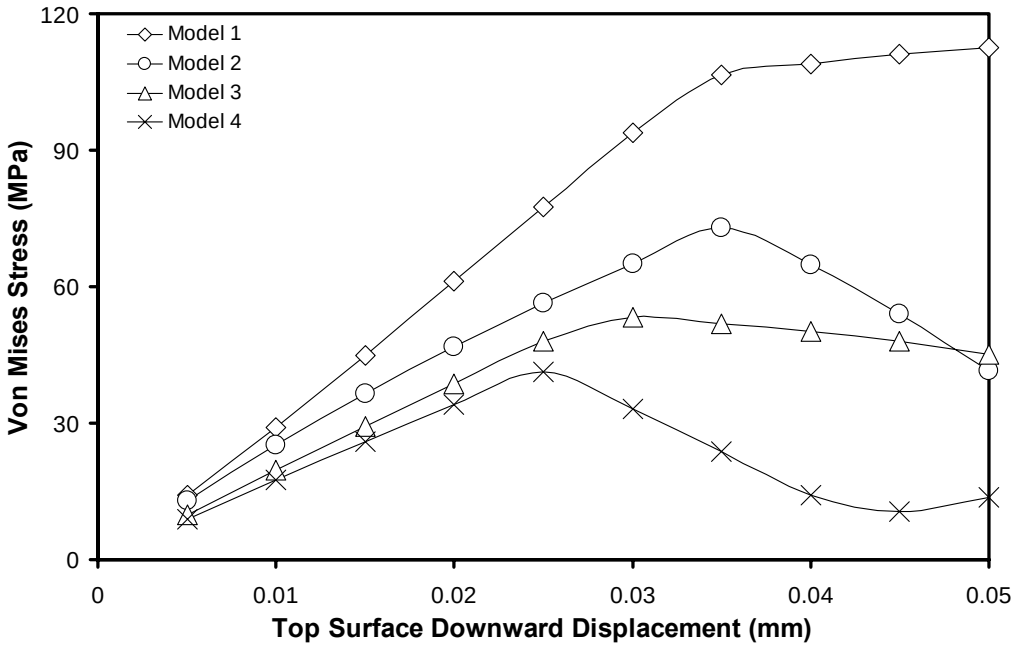

Figure 3.11. Von Mises stress at the outer surface of the middle of the vertical sidewall (Location B).

3.2. Deformation and Stress in a Tube/Matrix Cell

For the study of the matrix material properties, the tube/matrix cell dimensions are 1 mm wide and 2 mm tall. The tube geometry shown in Figure 3.4 is used for this analysis. The tube volume fraction is 0.209. The cavity volume fraction is 0.109. The ANSYS 6.1 finite element software is used for the analyses.

3.2.1. Boundary Conditions

Figure 3.12 shows the boundary conditions and material regions used for the analysis. Symmetry planes exist, and because of them it is sufficient to model only the top half of a tube/matrix cell. Modeling the top half of the tube/matrix cell allows for the inclusion of contact elements. This is not possible if only one quadrant or only the left or right half is modeled. Since the bottom surface of the model is a symmetry plane and is perpendicular to the y-axis, the y-displacement degrees of freedom along this surface were set to zero. The outer vertical edges of the tube/matrix cell are also symmetry planes. Therefore, the x-displacements of these surfaces were set to zero. This is consistent with a large array of tube/matrix cells. A y-displacement of -0.040 mm moves the top surface, and the plane strain assumption was used.

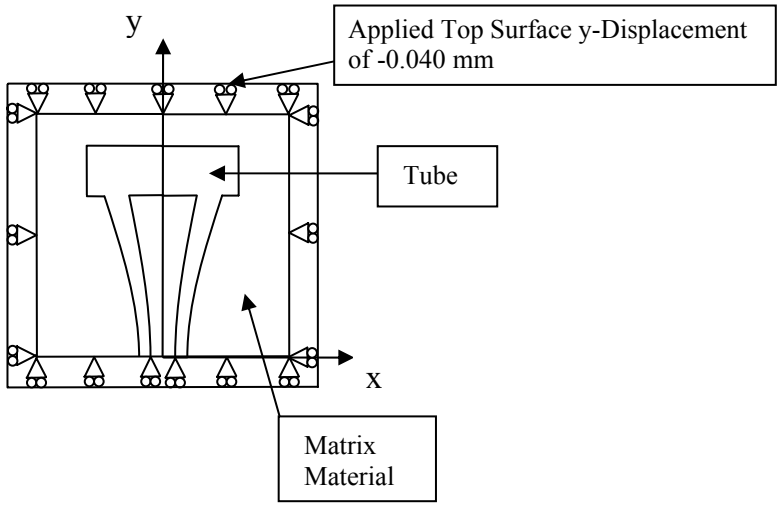

Figure 3.12. Material regions and boundary conditions used for the tube/matrix cell finite element model of Section 3.2.

3.2.2. Material Properties and Constitutive Models Used in the Analyses

The goal here is to understand the effects of changing the magnitude of material properties of the matrix. Table 3.3 summarizes the material properties used. The Saint Venant-Kirchhoff constitutive model describes the stress-strain response of the tube material. The tube material is isotropic. The Neo-Hookean constitutive model describes the stress-strain response of the elastomer matrix material. This is a nonlinear hyperelastic model for isotropic materials. The Neo-Hookean constitutive model is accurate for stretches up to 140 % [16]. There are other constitutive models, such as the Ogden model, that are accurate to larger stretches, but the Neo-Hookean model requires less experimental data. For an incompressible material, only the shear modulus in the undeformed configuration is required. This makes the Neo-Hookean constitutive model advantageous because extensive test data is not available. The governing differential equations for conservation of linear momentum with these constitutive models used are given in Section 2.1.

For each analysis the modulus of elasticity of the tube material is 2000 MPa, and the Poisson's ratio is 0.35. These properties are consistent with common thermoplastics

such as nylon 6/6 [17]. Two different matrix material property sets are studied. Both matrix materials are modeled as incompressible materials. Therefore, the Poisson's ratio of each is ½. For Matrix Material 1 the shear modulus is 10 MPa. For Matrix Material 2 the shear modulus is 1 MPa. From these properties the modulus of elasticity for each matrix material is 30 MPa and 3 MPa for Matrix Material 1 and Matrix Material 2 respectively. The material properties of Matrix Material 1 are consistent with polyurethane elastomers [18]. The material properties of Matrix Material 2 are consistent with many other types to elastomers. Again, millimeters are used as the length scale for the models, and therefore, all moduli must be input in MPa to produce momentum equations with the units N/mm^3. Nonlinear geometric effects are considered.

Table 3.3. Material properties used in tube/matrix cell study of Section 3.2.

Material Type	**Modulus (MPa)**	**Poisson's Ratio-ν**
Tube Material	Modulus of Elasticity-2000	0.35
Matrix Material 1	Shear Modulus-10	½
Matrix Material 2	Shear Modulus-1	½

3.2.3. Element Selection

Table 3.4 lists information about the type and number of elements in the finite element model. The ANSYS element type that models the tube material is the PLANE42 continuum element with the plane strain option activated (KEYOPT (3) = 2) [14]. Extra displacement shapes were included to improve bending behavior (KEYOPT(2) = 0). With these options, PLANE42 is a plane strain, 4-node quadrilateral finite element. It uses an incompatible-modes displacement formulation and is bilinear in displacements with x- and y-displacement degrees of freedom at each node.

The ANSYS element type that models the matrix material is the PLANE182 continuum element with the plane strain option activated (KEYOPT(3) = 2) and mixed u-p formulation chosen (KEYOPT(6) = 1) with B-bar method integration selected (KEYOPT(2) = 1), i.e. selective reduced integration of volumetric strain terms. With

these options selected, this is a plane strain, 4-node quadrilateral finite element. Its mixed u-p formulation is bilinear in displacement and constant in pressure. Both x- and y-displacement degrees of freedom are carried at each node and element constant pressure is carried as a Lagrangian multiplier.

The contact elements CONTA171 and TARGE169 model the surface-to-surface contact interaction between the tube sidewalls. These elements use an augmented Lagrangian formulation that enforces the no-penetration constraint condition when the sidewalls touch. The surface-to-surface friction coefficient was set to zero.

Table 3.4. Finite element types and attributes used in Section 3.2.

Element Type	**Number in Mesh**	**Number of Nodes**	**Degrees of Freedom**	**Sketch**
PLANE42 KEYOPT(2)=0 KEYOPT(3)=2 Plane Strain, Displacement Formulation, Quadrilateral, Continuum Element	3120	4	Linear x- and y-Displacements	
PLANE182 KEYOPT(2)=1 KEYOPT(3)=2 KEYOPT(6)=1 Plane Strain, Mixed u-p Formulation, Quadrilateral, Continuum Element	5766	4	Linear x- and y-Displacements	
		1 Internal	Element Constant Pressure	
CONTA171 2-D Surface-to-Surface Contact Line Element	70	2	Linear x- and y-Displacements	
TARGE169 2-D Surface-to-Surface Target Line Element	70	2	Linear x- and y-Displacements	

3.2.4. Numerical Results

Figures 3.13 and 3.14 are contour plots of the Von Mises stress at the time of sidewall contact, -0.036 mm top surface y-displacement, for Matrix Material 1 and 2 respectively. The Von Mises stress at the time of sidewall contact is larger for both cases when matrix material is present as compared to the case without matrix material.

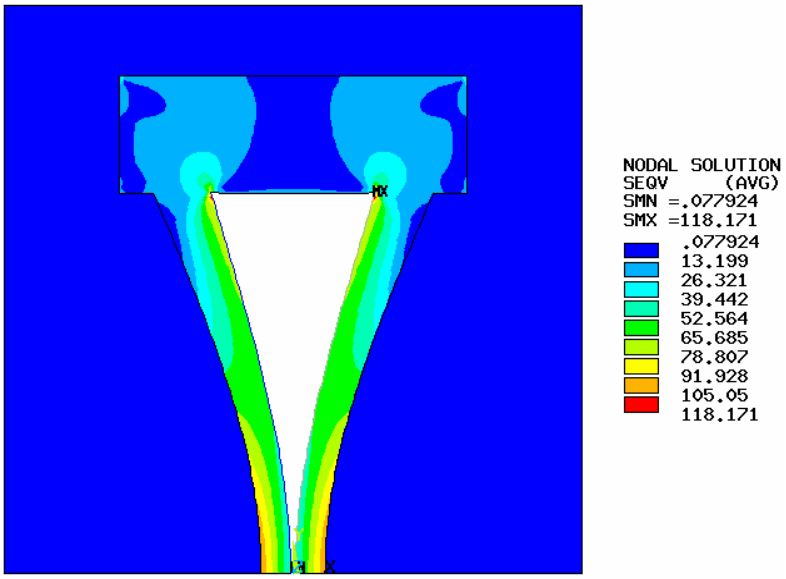

Figure 3.13. Contour plot of Von Mises stress with top surface y-displacement of -0.036 mm and matrix shear modulus of 10 MPa.

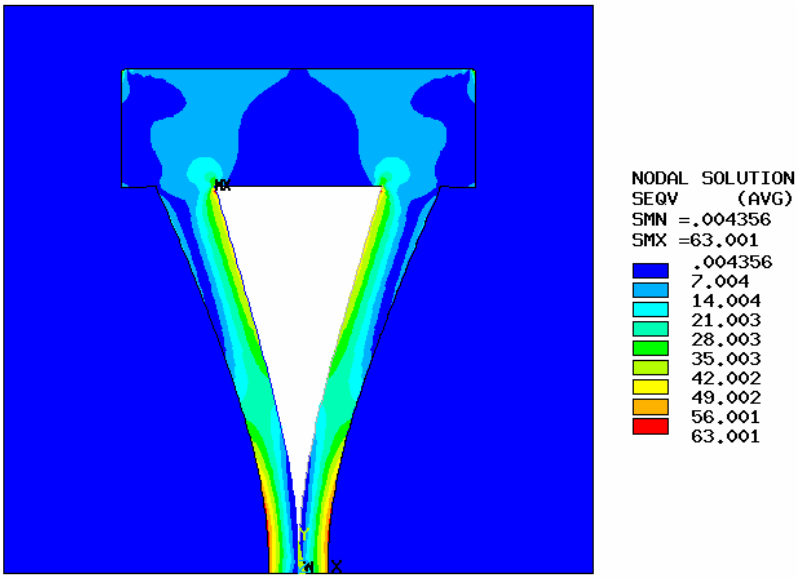

Figure 3.14. Contour plot of Von Mises stress with top surface y-displacement of -0.036 mm and matrix shear modulus of 1 MPa.

The highest values again appear at the outer surface of the middle of the sidewalls and the inside corners. The high stresses at the inside corners are localized, since the values rapidly drop to a lower value with increased distance from the corners. This drop is shown in Figure 3.15 for both models. No material nonlinearities are considered in the tube material. A stiffness reducing material nonlinearity in the tube material could possibly relieve the high stress at the sharp corner. Also, an actual tube corner will have a radius that is not considered in this model.

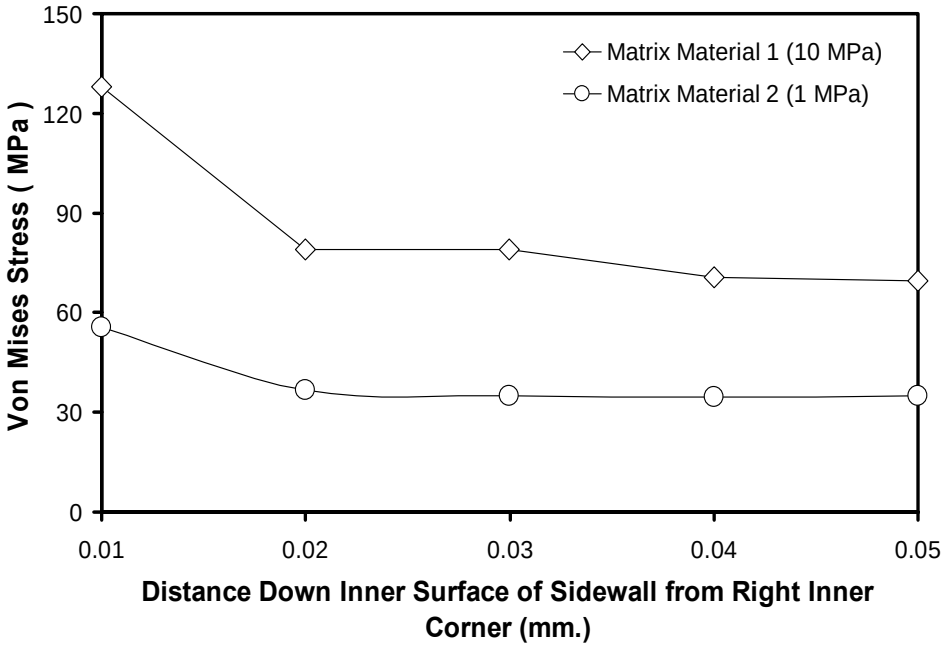

Figure 3.15. Von Mises stress on inner surface of sidewall.

For identification purposes, the outer surface of the middle of the right sidewall is now referred to as Location 1. In addition, a position 0.01 mm down the inner sidewall surface from the right inside corner is now referred to as Location 2. Figure 3.16 shows these locations.

Figure 3.17 is a plot of the Von Mises stresses at Locations 1 and 2 as a function of top surface downward displacement for models with Matrix Material 1 and Matrix Material 2. Note that, if the top surface downward displacement magnitude is kept below 0.025 millimeters, the stress values at Location 1 and Location 2 remain within reasonable levels when either matrix material is used. This is equivalent to -2.5 % through-the-thickness engineering strain. However, larger strain values may be applied without inducing high stress values at these locations if a more compliant matrix material is used. The best imaginable case is that adequate damping could be produced by some phenomenon without the need for large strains.

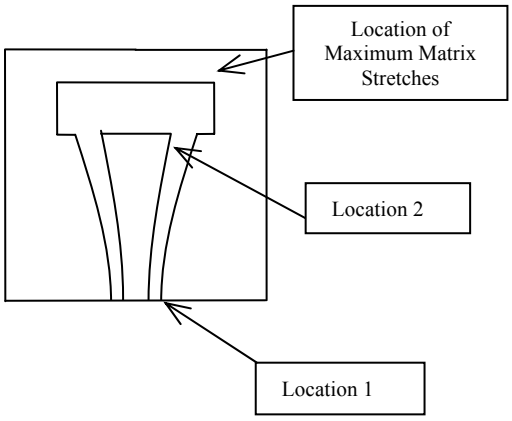

Figure 3.16. Locations of high stress and strain values.

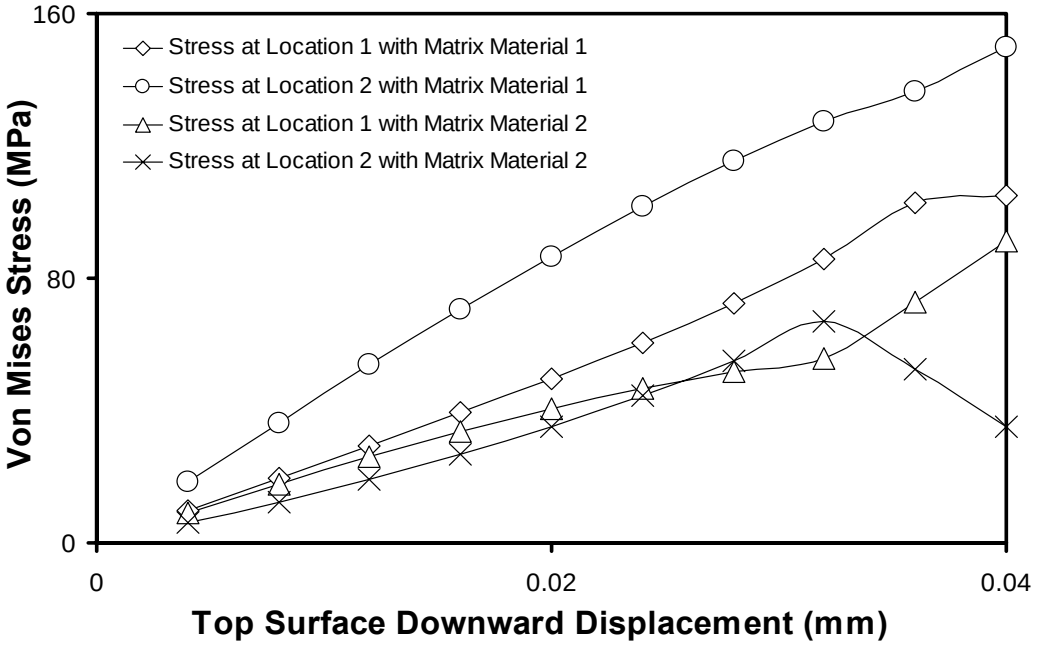

Figure 3.17. Von Mises stress in tube/matrix cell.

The principal stresses, the maximum shear stresses, and the Von Mises stress at Location 1 and Location 2 for a top surface y-displacement of -0.032 mm appear in Table 3.5. This is just prior to sidewall contact for both models. The values for the softer matrix are lower, especially at Location 2.

Table 3.5. Stress values at -0.032 mm top surface displacement.

Stress Type	**Tube in Matrix 1**		**Tube in Matrix 2**	
	Location 1	Location 2	Location 1	Location 2
Principle Stress-1 (MPa)	3.07	-10.75	0.71	-4.25
Principle Stress-2 (MPa)	-32.10	-58.28	-26.14	-25.06
Principle Stress-3 (MPa)	-94.80	-155.77	-75.40	-67.35
Max. Shear Stress (MPa)	48.93	72.51	38.05	31.55
Von Mises Stress (MPa)	85.86	127.34	66.85	55.69

Maximum strains occurring in the matrix material are near the upper outside corners of the tube. This location is shown in Figure 3.16. The corners in this model have sharp edges. Giving the corners a radius could reduce the strains in these areas. Table 3.6 shows the principal stretches in the matrix material near the upper right outside corner of the tubes for a top surface y-displacement of -0.032 mm. The results show that the maximum matrix principle stretches are larger for the model with the softer matrix. The selection of appropriate matrix stiffness properties for an application depends on the desired stiffness, the maximum applied through-the-thickness strain, and the stress limits of the tube and matrix materials.

Table 3.6. Maximum matrix principle stretches for applied top surface y-displacement of -0.032 mm.

	Matrix Material 1	**Matrix Material 2**
Principle Strain-1	0.132448	0.721483
Principal Strain-2	0	0
Principal Strain-3	-0.132448	-0.721483

3.2.5. Determining Effective Through-the-thickness Stiffness

Finding the through-the-thickness stiffness from the material properties of the tube and the matrix is not an easy analytical task. This is due to the complex tube shape and the material void inside the tube. Therefore, the stiffness was determined by finite element analysis. The value obtained is considered a constrained modulus of a single tube/matrix cell or the apparent modulus of a large array of tube/matrix cells compressed uniformly and simultaneously. Figures 3.18 is a plot of the average y-direction normal stress as a function of engineering strain obtained from the models with Matrix Material 1 and Matrix Material 2.

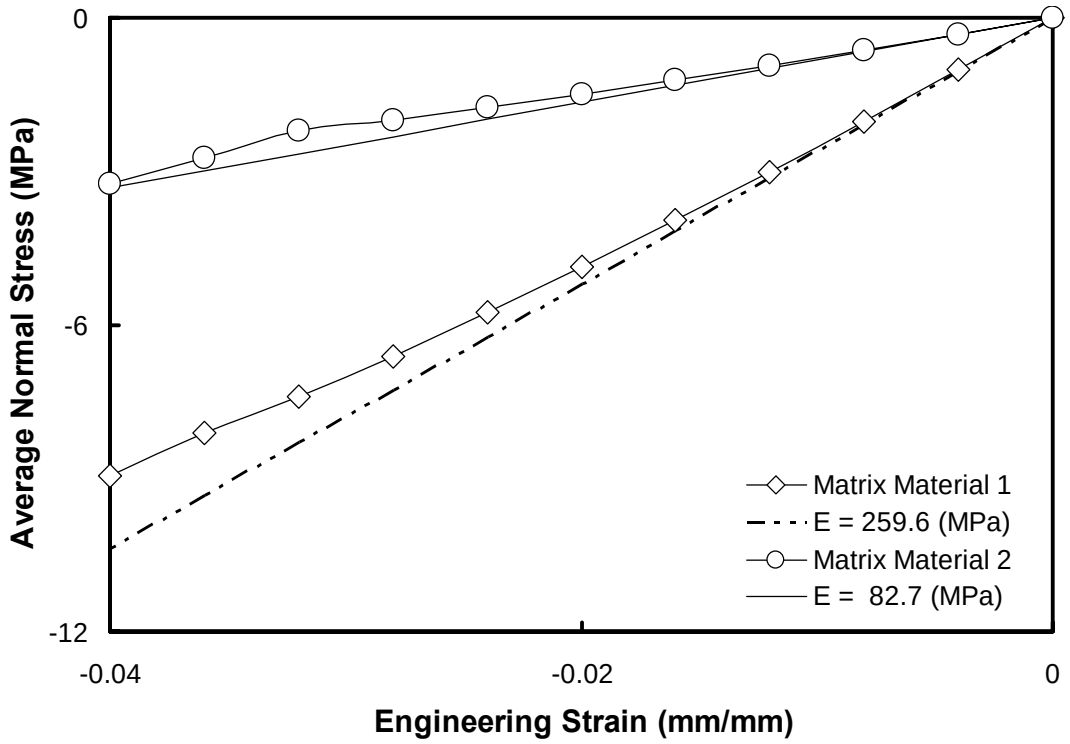

Figure 3.18. Stress-strain curves with zero percent modulus lines.

The stress values are the sum of all top surface nodal y-reaction forces divided by the top surface area. In the finite element models there is no difference in the undeformed

and deformed top surface area because of the symmetry boundary conditions at either side of the tube/matrix cell and the uniformity of the top surface y-displacement. The strain values are the top surface y-displacements divided by the original height of the model. Note that this applies for compression only. Different results will be obtained in tension because of the structure of the tube sidewalls. Reducing the shear modulus of the matrix material by 90 % causes a decrease of approximately 68 % in the apparent zero percent stiffness of a tube/matrix cell. Therefore, the apparent stiffness of a tube/matrix cell shows dependence upon the stiffness of the matrix material. The dependence does not appear to be extremely strong; a given percent change in matrix material stiffness results in a smaller percent change is tube/matrix cell stiffness.

4. INVESTIGATION OF FLUID FLOW IN AND INTERACTION WITH TUBES EMBEDDED IN A MATRIX

The discussion and study of methods for producing damping composite materials by the introduction of fluid-filled simple machines appears in five sections. All computations are carried out under the isothermal assumption and all body forces are zero.

First, in Section 4.1 the effect of inserting sealed, fluid-filled tubes into an elastomer matrix is studied. Second, in Section 4.2 the tube cavity pressure production and energy dissipation characteristics obtained by inserting tubes containing viscous fluid with zero pressure end conditions into an elastomer matrix are studied. A simplified model for determining fluid pressure is derived for an incompressible fluid using the principles of conservation of mass and conservation of linear momentum. Third, in Section 4.3 different definitions of specific damping capacity are discussed. Fourth, in Section 4.4 dimensional analysis shows the important dimensionless parameters governing the fluid-structure interaction problem. Lastly, in Section 4.5 transient, three dimensional finite element models are used to predict the damping properties of a tube/matrix cell. Comparisons are made between the results obtained from the simplified model and those from the transient, three dimensional models for identical problems. Differences are addressed and possible reasons for the differences are identified. The effects of changing the fluid cavity geometry are also explored.

4.1. Modeling Sealed Tubes Embedded in an Elastomer Matrix

One possible method of producing a damping machine augmented composite (MAC) material is to insert sealed tubes that are completely filled with viscous fluid into a matrix material. The question is: would the damping produced by this method warrant the development of such materials?

A study of the structural response of a composite lamina consisting of sealed, fluid-filled tubes embedded in an elastomer matrix subjected to harmonic excitation was

conducted using the ANSYS 6.1 finite element software in order to help answer this question. Two symmetry planes and the plane strain assumption reduced computational model size as compared to the model size necessary if these conditions were not in place.

A modal analysis determines the vibrational characteristics of a linear structure. The primary information obtained is a structure's natural frequencies and their corresponding mode shapes. For non-damped structures the natural frequencies correspond to resonant frequencies. When a structure is subjected to forced harmonic excitation, these resonant frequencies must be considered since spikes in structural response occur at resonance.

Harmonic response analysis is a special type of transient analysis. As the name suggests, harmonic response analysis is a type of transient analysis where the structure is excited by a sinusoidal applied load or displacement and the steady-state dynamic response of the structure is determined. This type of analysis, like modal analysis, is limited to linear problems, i.e. small displacement, linear elasticity problems.

First, a modal analysis was performed on a tube/matrix cell without fluid so that the effects of adding a contained fluid could be ascertained. Next, a harmonic analysis was performed on the same tube/matrix cell to verify the first natural frequency found by the modal analysis. Finally, a harmonic analysis was performed on a tube/matrix cell with contained fluid. The effects of changing the viscosity of the fluid were studied.

The sealed fluid cavity response was predicted with the assumption that the net velocity of the fluid is zero and the fluid is a liquid with a finite bulk modulus. The contained fluid was modeled as a modified elastic solid with very small shear modulus and a given bulk modulus and dynamic viscosity.

The fluid was considered a compressible liquid. The bulk moduli of common liquids are quite large. For example, the bulk modulus of motor oil is approximately 1.5 GPa. Therefore, a structure containing a sealed cavity will be considerably stiffer when filled with liquid than when the cavity is empty. If a large, compressive enforced-displacement boundary condition is applied, the structure might fail because large stresses may be produced because of the volumetric stiffness of the fluid. For this

reason applied displacement boundary conditions were limited to the small strain regime. The assumptions of small strains and no net velocity allow for the linearization of the governing differential equations, and this simplifies the solution process.

4.1.1. Governing Differential Equations

This analysis requires solving a set of coupled linear partial differential equations in space and time. The set of differential equations governing the conservation of linear momentum of a continuum are given as Equation (4.1). Equation (4.2) is the constitutive equation for a linear elastic material subjected to small strains that relates the Cauchy stress tensor ($\vec{\vec{\sigma}}$) to the infinitesimal strain tensor ($\vec{\vec{e}}$). This relationship is known as generalized Hooke's law. Equation (4.3) defines the infinitesimal strain tensor. Since the displacements are small, no distinction is made between the undeformed and deformed configurations.

$$\rho \frac{\partial^2 \vec{u}}{\partial t^2} = \vec{\nabla}_x \cdot \vec{\vec{\sigma}} + \rho \vec{f} \text{ In } \Omega \tag{4.1}$$

$$\sigma_{ij} = C_{ijkl} e_{kl} \tag{4.2}$$

$$e_{ij} = \frac{1}{2}\left(\frac{\partial u_i}{\partial x_j} + \frac{\partial u_j}{\partial x_i} \right) \tag{4.3}$$

In Equations (4.1)-(4.3), $\vec{\vec{\vec{\vec{C}}}}$ is a fourth order elasticity tensor, $\vec{u}$ is a vector-valued function of displacements, and $\vec{f}$ is a vector-valued function of body forces. All of these are defined on the domain (Ω) of the continuum.

For the liquid, the stress-strain relationship is as shown in Equation (4.4) [19].

$$\begin{Bmatrix} \varepsilon_{bulk} \\ \gamma_{xy} \\ \gamma_{yz} \\ \gamma_{xz} \\ R_x \\ R_y \\ R_z \end{Bmatrix} = \begin{bmatrix} \frac{1}{K} & 0 & 0 & 0 & 0 & 0 & 0 \\ 0 & \frac{1}{S} & 0 & 0 & 0 & 0 & 0 \\ 0 & 0 & \frac{1}{S} & 0 & 0 & 0 & 0 \\ 0 & 0 & 0 & \frac{1}{S} & 0 & 0 & 0 \\ 0 & 0 & 0 & 0 & \frac{1}{B} & 0 & 0 \\ 0 & 0 & 0 & 0 & 0 & \frac{1}{B} & 0 \\ 0 & 0 & 0 & 0 & 0 & 0 & \frac{1}{B} \end{bmatrix} \begin{Bmatrix} P \\ \tau_{xy} \\ \tau_{yz} \\ \tau_{xz} \\ M_x \\ M_y \\ M_z \end{Bmatrix} \tag{4.4}$$

where:

K = Bulk Modulus

S = K x 10^{-9} (arbitrary small number to give some shear stability)

B = K x 10^{-9} (arbitrary small number to give some rotational stability)

P = Pressure

ε_{bulk} = Volumetric Strain (e_{ii})

γ_{ij} = Shear Strain

τ_{ij} = Shear Stress

R_i = Rotation about Axis i

M_i = Twisting Force about Axis i

The stress strain rate relationship is as given in Equation (4.5) [19].

$$\begin{Bmatrix} \dot{\varepsilon}_{bulk} \\ \dot{\gamma}_{xy} \\ \dot{\gamma}_{yz} \\ \dot{\gamma}_{xz} \\ \dot{R}_x \\ \dot{R}_y \\ \dot{R}_z \end{Bmatrix} = \begin{bmatrix} 0 & 0 & 0 & 0 & 0 & 0 & 0 \\ 0 & \frac{1}{\mu} & 0 & 0 & 0 & 0 & 0 \\ 0 & 0 & \frac{1}{\mu} & 0 & 0 & 0 & 0 \\ 0 & 0 & 0 & \frac{1}{\mu} & 0 & 0 & 0 \\ 0 & 0 & 0 & 0 & \frac{1}{c} & 0 & 0 \\ 0 & 0 & 0 & 0 & 0 & \frac{1}{c} & 0 \\ 0 & 0 & 0 & 0 & 0 & 0 & \frac{1}{c} \end{bmatrix} \begin{Bmatrix} P \\ \tau_{xy} \\ \tau_{yz} \\ \tau_{xz} \\ M_x \\ M_y \\ M_z \end{Bmatrix} \tag{4.5}$$

where:

μ = Dynamic Viscosity of Fluid

$c = 1 \times 10^{-5} * \mu$

$\dot{\varepsilon}_{bulk}$ = Volumetric Strain Rate

$\dot{\gamma}_{ij}$ = Shear Strain Rate

τ_{ij} = Shear Stress

$\dot{R}_i$ = Rotation Rate about Axis i

M_i = Twisting Force about Axis i

Equation 4.4 is used by ANSYS to develop a stiffness matrix. Equation (4.5) is used by ANSYS to develop a damping matrix, and the fluid density is used by ANSYS to develop a lumped mass matrix for the elements representing the contained fluid.

4.1.2. Model Rational and Solution Procedure

For a modal analysis all displacement boundary conditions that would be specified during a corresponding transient or harmonic analysis are set to zero. As many natural frequencies and mode shapes may be determined as there are non-zero degrees of

freedom in the model. The more degrees of freedom in the model, the more accurately the natural frequencies and mode shapes may be determined. A solution pass is made to determine the natural frequencies (eigenvalues) and a second solution pass is made to expand corresponding mode shapes (eigenfunctions). A modal analysis was not performed for the models with fluid. When ANSYS FLUID79 elements, which are discussed in the next section, are used the results are polluted by low frequency modes of the interior of the fluid region [14]. For this reason, harmonic analysis was used to locate the first resonant frequency for models containing fluid.

For a harmonic analysis both the real and imaginary parts of applied boundary conditions must be specified. The tube material was modeled as an isotropic, linearly, elastic, compressible material. The matrix material was modeled as an isotropic, linearly elastic, incompressible material. The fluid was modeled as an isotropic, compressible, viscous liquid. Continuity of displacement components at the fluid-solid interface was enforced.

A frequency range of interest was chosen and frequency steps were taken in place of time steps. The output was in the form of the amplitude and phase angle of the various quantities describing the sinusoidal structural response to the sinusoidal excitation.

4.1.3. Element Selection

Table 4.1 gives information about the type and number of elements in the finite element model. The tube and matrix materials were modeled with the same element types and options as described in Section 3.2.3. FLUID79 contained-fluid elements were used to model the fluid contained in the sealed tube cavities. These elements are solid continuum elements modified to have a negligible resistance to shear strains, a volumetric stiffness, and shear strain rate proportional damping [14]. This element is a 4-node quadrilateral finite element that is bilinear in displacements. Both x- and y-displacement degrees of freedom are carried at each node. This element type only offers a lumped (diagonalized) mass matrix.

Table 4.1. Element Descriptions for Section 4.1.

Element Type	Number in Mesh	Mass Matrix	Number of Nodes	Degrees of Freedom	Sketch
PLANE42 KEYOPT(2)=0 KEYOPT(3)=2 Plane Strain, Displacement Formulation, Quadrilateral, Continuum Element	510	Consistent	4	Linear x- and y-Displacements	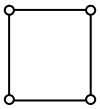
PLANE182 KEYOPT(2)=1 KEYOPT(3)=2 KEYOPT(6)=1 Plane Strain, Mixed u-p Formulation, Quadrilateral, Continuum Element	1210	Consistent	4	Linear x- and y-Displacements	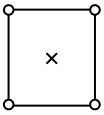
			1 Internal	Element Constant Pressure	
FLUID79 2-D, Contained Fluid, Quadrilateral, Continuum Element	240	Lumped (Diagonalized)	4	Linear x- and y-Displacements	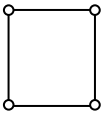

4.1.4. Model Generation and Boundary Conditions

The ANSYS 6.1 graphical user interface (GUI) was used for preprocessing. The geometry was created, the material properties were defined, and the boundary conditions were applied to the solid model. The lengths were input in millimeters. Because of this, extra care was taken when entering material properties. For example, elastic moduli were entered in MPa, viscosities in $N \cdot s/mm^2$, and densities in mega-grams/mm^3. Displacements were output in millimeters and pressures and stresses were output in MPa. These units yield conservation of linear momentum equations with units of N/mm^3.

Figure 4.1 shows the boundary conditions and material regions used for the analysis with fluid contained in the tube/matrix cell. This is a quarter-model. The plane strain assumption was used for both the modal and the harmonic analyses.

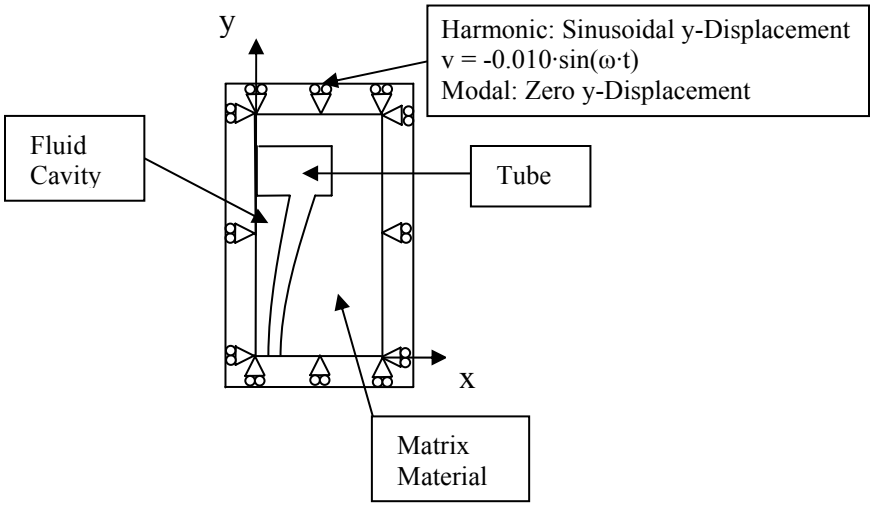

Figure 4.1. Computational domain and boundary conditions for Section 4.1.

The finite element mesh was generated and solution controls such as analysis type and options were specified. The analysis type was either MODAL or HARMONIC depending on the specific model. For both modal and harmonic analyses, the cross section of the tube/matrix cell lies in the x-y plane. Three symmetry planes are used in the models. One symmetry plane bisects the tube/matrix cell along the x-axis and the second bisects the model along the y-axis. The third symmetry condition was applied to the outer vertical boundary of the tube/matrix cell. This condition is based on the assumption that the tube/matrix cell is only one in a very large array. Therefore, the symmetry condition takes into account the interaction of adjacent, similarly loaded cells. In models containing fluid the symmetry conditions were also applied to the fluid domain.

For the modal analysis the y-displacements of the top surface of the cell were set to zero. The mode shapes were normalized to UNITY [20]. This means that the mode shape vector is normalized by a method that results in its L^2 norm being equal to one.

For the harmonic analyses the y-displacements of the top surface of the tube/matrix cell were specified by supplying the real and imaginary parts of the harmonic excitation. For both cases, fluid and no fluid, these values were set to -0.01 mm and 0.00 mm

respectively. The FULL analysis method was chosen. This means that the entire model was solved and no master degrees of freedom were defined. AMPLITUDE + PHASE was selected as the output printout format.

Once these tasks were completed, the solution was executed. ANSYS produces a model data base (.db) file and a structural output (.rst) file. The ANSYS postprocessor POST1 shows results for a given frequency. The ANSYS postprocessor POST26 shows the history of a particular degree of freedom as a function of frequency for the harmonic analysis.

4.1.5. Material Properties and Constitute Models used for the Analyses

Table 4.2 shows the material properties used for the analyses. The tube material was modeled as an isotropic, linearly elastic material subjected to small strains with a modulus of elasticity of 2000 MPa and a Poisson's ratio of 0.35. The matrix material was modeled as an isotropic, incompressible, linearly elastic material subjected to small strains. Since the material is incompressible, its Poisson's ratio is ½. The modulus of elasticity of the matrix material is 30 MPa. The densities of both the tube material and the matrix material are 1100 kg/m^3. The fluid viscosity was changed for different test situations and is identified with the respective results in Section 4.1.6. The fluid density and fluid bulk modulus were taken as 970 kg/m^3 and 1500 MPa respectively. The fluid density, bulk modulus, and viscosities for the fluid are common for various oils.

Table 4.2. Material properties for tube/matrix cell study of Section 4.1.

Material Type	**Density (kg/m^3)**	**Modulus (MPa)**	**Poisson's Ratio**
Tube Material	1100	Modulus of Elasticity-2000	0.35
Matrix Material	1100	Modulus of Elasticity-30	½
Fluid	970	Bulk Modulus-1500	N/A

4.1.6. Results of Modal and Harmonic Analysis of a Tube/matrix Cell

The first five natural frequencies found for the tube/matrix cell with no fluid present by using a modal analysis are shown in Table 4.3. The smallest natural frequency is 95.7 kHz.

Table 4.3. First five natural frequencies of tube matrix cell with no fluid.

Natural Frequency #	**Frequency (kHz)**
1	95.7
2	134.1
3	171.8
4	213.9
5	225.3

Figure 4.2 shows the first normalized mode shape. Figure 4.3 is a contour plot of the Von Mises stress distribution on the first normalized mode shape of the structure. As mentioned earlier, the mode shape is normalized. Therefore, the contour plot is only valuable for locating points of higher or lower stress values.

To verifying the first natural frequency obtained by the modal analysis and to test the effectiveness of the harmonic method, a harmonic analysis was performed on the tube/matrix cell with no fluid. Once the driving frequency range in the neighborhood of the first resonant frequency was identified, a more refined harmonic analysis was performed. Figure 4.4 is a plot of the amplitude of the y-direction reaction force per unit thickness for the left uppermost node in the finite element mesh. This node represents the center of the top surface of the tube/matrix cell. In the figure, the force is plotted versus the driving frequency. The numerical value of the peak is not the actual peak since at resonance the value is not bounded for an un-damped system. A frequency stepping procedure was used in the analysis and the resonant frequency was not exactly hit by a frequency step. Figure 4.5 is a plot of the phase angle of the reaction force versus driving frequency.

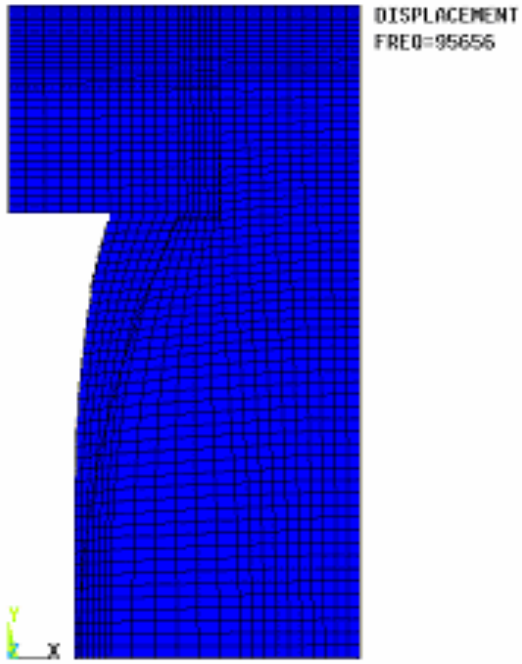

Figure 4.2. Deformed shape and undeformed edge for first mode.

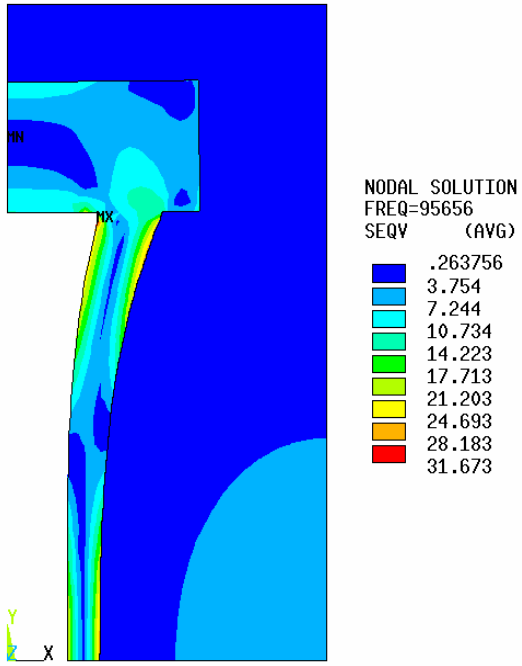

Figure 4.3. Von Mises stress (MPa) distribution on first mode shape.

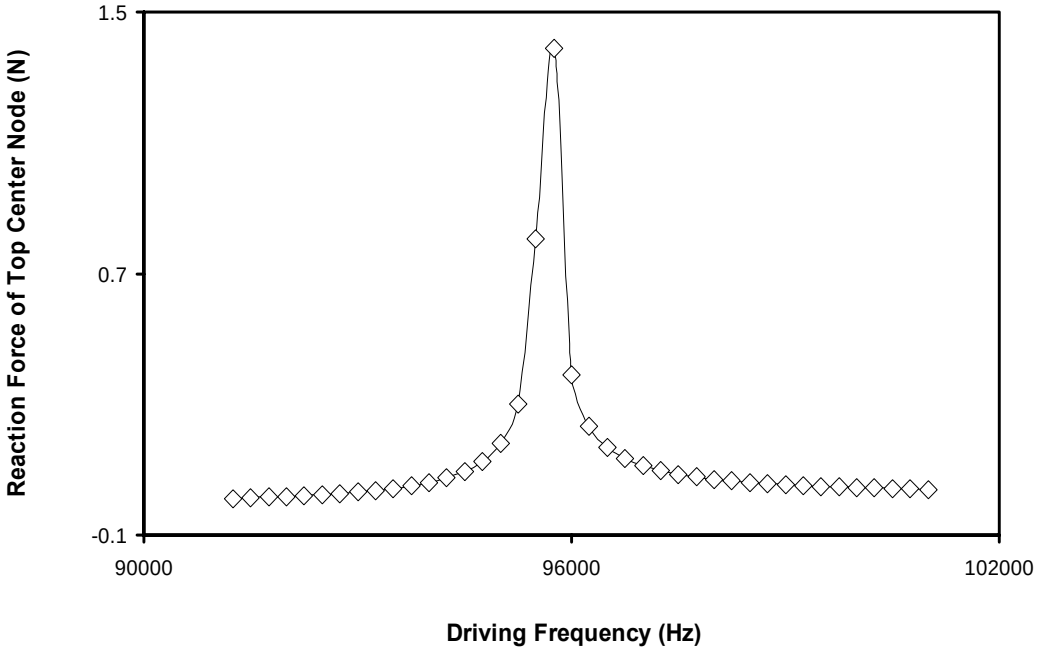

Figure 4.4. Amplitude of y-direction reaction force at center of top surface of cell.

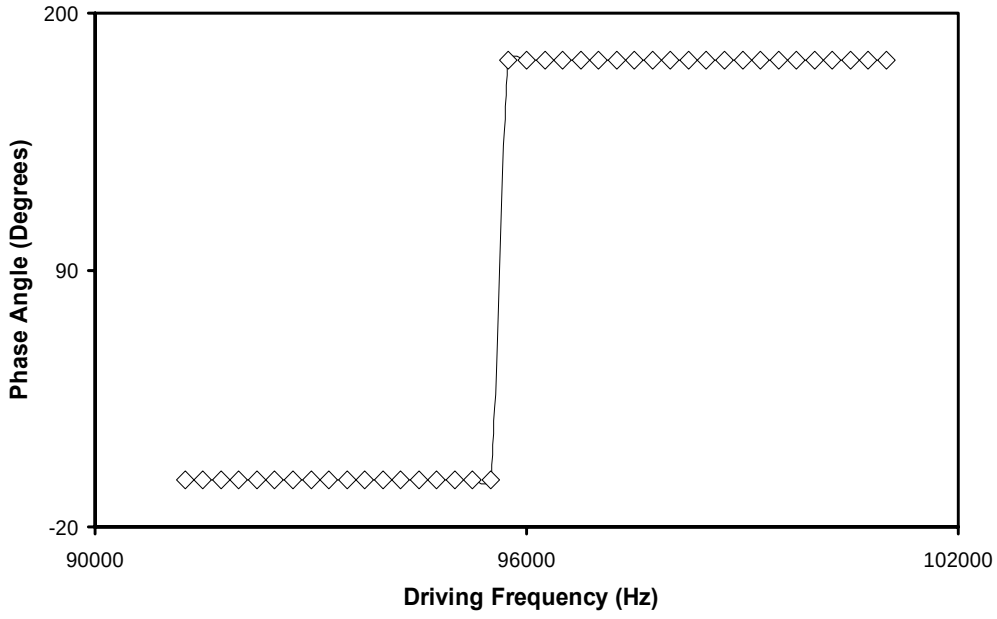

Figure 4.5. Phase Angle of y-direction reaction force at center of top surface of cell.

Figure 4.4 shows that a spike in the reaction force needed to enforce the applied sinusoidal displacement occurs at the driving frequency predicted by the modal analysis. Figure 4.5 shows that the phase angle shifts by 180º and passes through 90º at approximately 95.7 kHz.

Since the first harmonic analysis agreed with the modal analysis, a harmonic analysis was used to determine the first resonant frequency of the tube/matrix cell containing a viscous fluid. Three fluid viscosities were used. The fluid density and bulk modulus are constant. Figures 4.6 is a plot of the amplitude of the y-direction reaction force per unit thickness versus driving frequency for fluid viscosities of 1, 10, and 100 poise. Figures 4.7 is a plot of the phase angle of the reaction force versus driving frequency for fluid viscosities of 1, 10, and 100 poise.

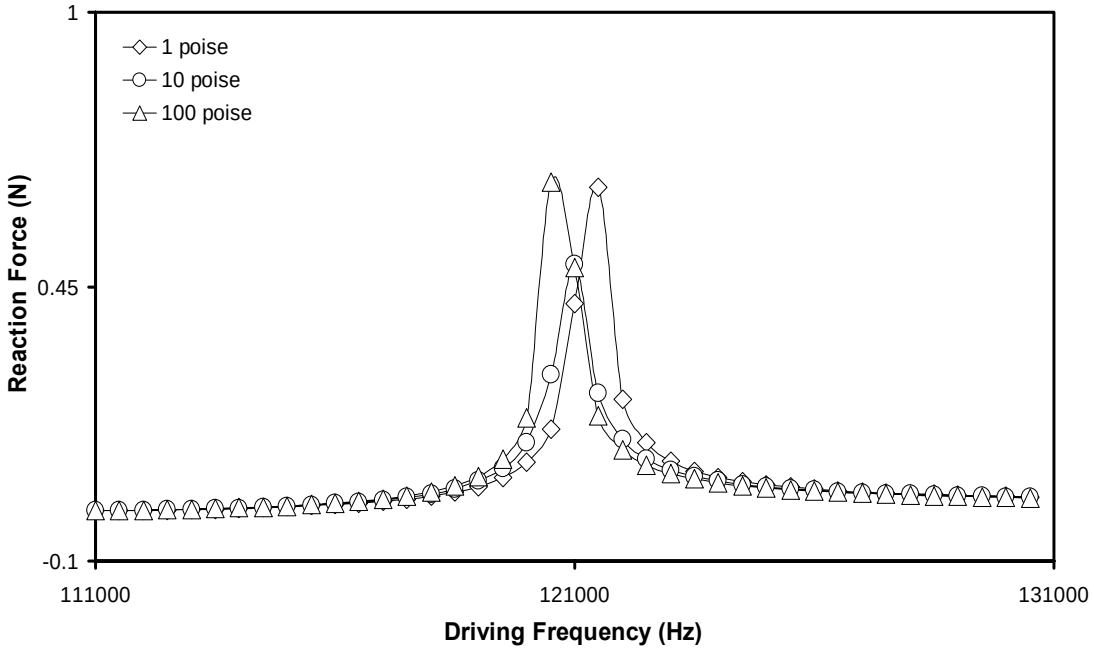

Figure 4.6. Amplitude of y-direction reaction force at node located at center of top surface of a cell.

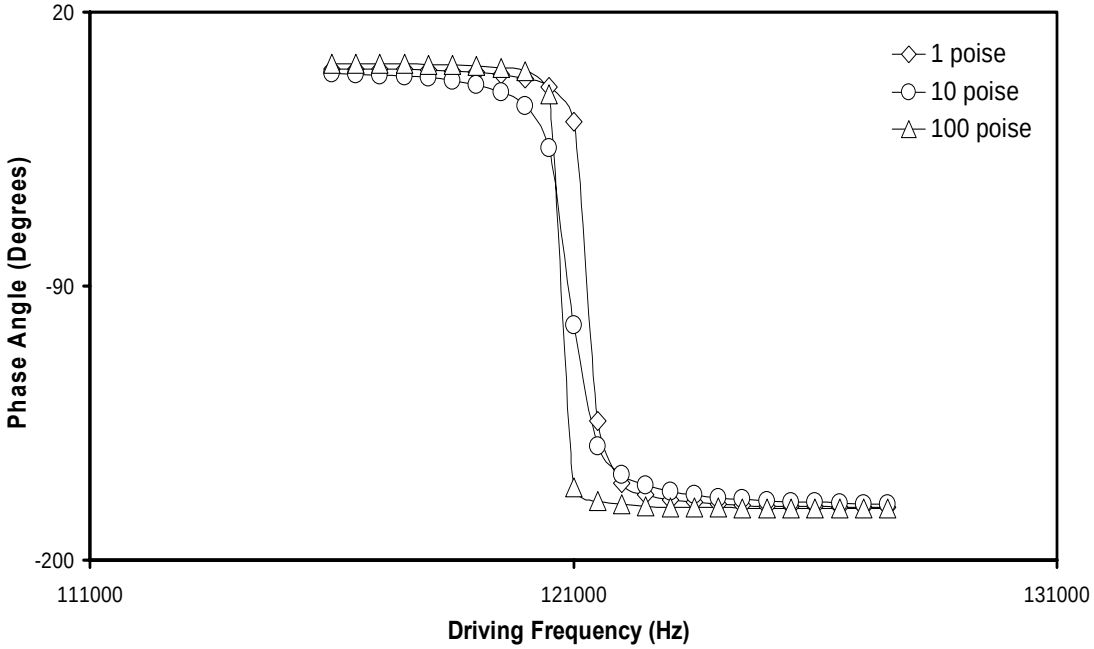

Figure 4.7. Phase angle of y-direction reaction force at center of top surface of a cell.

From Figures 4.4-4.7 it is obvious that the models with fluid have higher values for their first resonant frequency than the model without fluid. The shift is upward by approximately 25 kHz. This increase was expected since a contained fluid increases the stiffness of the structure, thus increasing the first resonant frequency.

The fluid's viscosity should produce some damping in the structure. The data presented in Figures 4.6 and 4.7 show that the structure containing viscous fluid still behaves as an under-damped system. The effect of increasing the fluid dynamic viscosity is noticeable, but small. For the model without fluid the peak in reaction force passes in a frequency band of approximately 1 kHz. With fluid the peaks pass in a frequency band of approximately 2-3 kHz. A change in fluid dynamic viscosity from 1 poise to 100 poise only shifts the resonant frequency downward by approximately 1 kHz.

At low driving frequencies the damping effect is negligible. However, the upward shift of the first resonant frequency allows for a wider operating range of driving frequency, if the first resonant frequency acts as an upper bound.

Figure 4.8 is a contour plot of Von Mises stress at a driving frequency of 50 Hz and 100 poise fluid dynamic viscosity. The stress values are lower than the strengths of materials with properties consistent with those used in the analysis. Therefore, the structure could be loaded this way and not cause failure. At this driving frequency it is found that the phase difference between force and displacement is negligible.

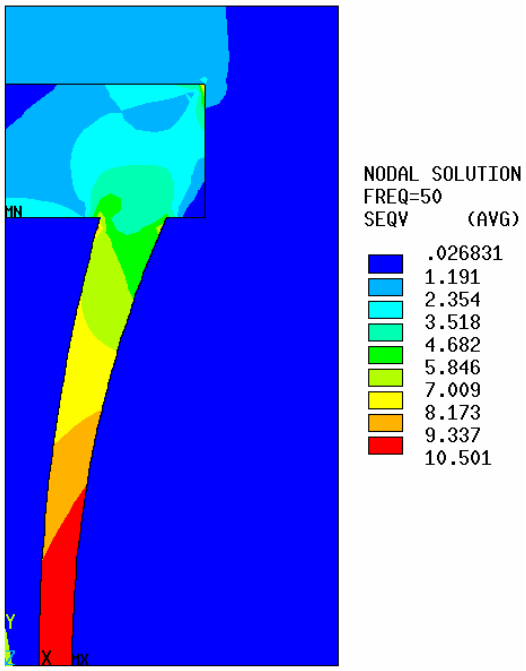

Figure 4.8. Von Mises stress (MPa) distribution for driving frequency of 50 Hz and 100 poise fluid dynamic viscosity.

These results suggest that the introduction of contained viscous fluid into this sealed tube/matrix cell does not produce a material that is highly dissipative for these values of fluid dynamic viscosity and this geometry. Therefore, other configurations are considered in the sections that follow.

4.2. Modeling of Embedded, Fluid-Filled Tubes with Zero Pressure End Conditions Using Simplified Equations

The results of the previous section imply that effective damping machine augmented composite materials will not result from placing sealed, fluid-filled tubes into a matrix material. Therefore in this section another configuration is considered. The situation considered in this section is that of long, fluid-filled tubes that are embedded in an elastomer matrix, and that have zero pressure end conditions. The loading considered is a through-the-thickness, uniform sinusoidal compression.

Modeling of fluid-structure interaction is more complex in cases where fluid velocities are large and solid strains are large than in cases where fluid velocities are small and solid strains are small. This more complex analysis requires the solving of a set of coupled nonlinear partial differential equations in space and time. Information on the governing equations appears in Section 2. Due to the complex geometry, loading, and constraints of the problems considered here, these equations were treated numerically by using the finite element method for spatial descretization and finite difference approximation for temporal descretization.

4.2.1. Development of Simplified Fluid Flow Equations

The Navier-Stokes equations can often be simplified if certain physical conditions are met. For example, in situations where the inertial forces are much smaller than viscous forces, the left hand side of Equation 2.28 may be set to zero. These equations are known as Stokes equations. Also, when modeling squeeze film damping, the Stokes equations are simplified further by using the fact that the velocity and length scales in certain directions are much larger than the velocity and length scales in other directions. These equations are known as Reynolds equations. A similar approach was taken to develop simplified equations governing flow in a long, narrow tube whose cross sectional area is deformed in order to induce flow. The cross section of the tube lies in the x-y plane and the tube extends in the z-direction.

The development began by using a deforming control volume analysis for conservation of mass of an incompressible fluid. The analysis was applied to the fluid contained within a long tube whose cross section is deformed as a sinusoidal function of time. The objective of the control volume analysis was to develop a relationship between the tube deformation and the average z-component of the fluid velocity as a function of z. Equation (4.6) gives the integral equation for conservation of mass using a deforming control volume.

$$\frac{\partial}{\partial t}\int_{cv}\rho dV + \int_{cs}\rho\vec{c}\cdot\vec{n}dA = \frac{Dm}{Dt}_{System} = 0 \tag{4.6}$$

The fluid flow was assumed to be symmetric about the plane z = 0. Therefore, the z-component of the fluid velocity is zero at locations within the fluid domain that lie on the x-y plane. A control volume was chosen such that the control surface consists of a surface on the plane z = 0, the surfaces representing the interior sidewalls of the tube, and a surface parallel to the x-y plane that has the z-coordinate of the location at which the average z- component of the fluid velocity is desired. In this situation the convective velocity ($\vec{c}$) on the portion of the control surface representing the interior walls of the tube is zero since the walls drive the flow. On the portion of the control surface that lies on the x-y plane, the dot product of the convective velocity and the unit outward normal vector to the control surface is zero. This is because the z-component of the fluid velocity is zero on the x-y plane and the control volume does not deform in the z-direction. The unit outward normal vector to the remaining portion of the control surface (the z-plane on which the velocity is desired) only has a positive z-component. The dot product of the convective velocity and the normal vector to this surface is the z-component of the fluid velocity since the control volume does not deform in the z-direction. The resulting relationship for the average velocity as a function of z obtained from Equation (4.6) is shown as Equation (4.7).

$$\overline{w}(z,t) = -\frac{\dot{V}_{tube}(z,t)}{A_{tube}(z,t)} = -\frac{\overline{\dot{A}}_{tube}(z,t)}{A_{tube}(z,t)} \cdot z \tag{4.7}$$

where

$$\overline{\dot{A}} = \frac{1}{z}\int_0^z \dot{A}(\xi,t)d\xi$$

Here $\overline{w}$ is the average z-component of fluid velocity taken on the cross sectional area of the tube cavity. The symbol $\overline{\dot{A}}_{tube}$ represents the average rate of change of tube cross sectional area of the tube cavity. The averaging is carried out from the origin to a given z-location at a given time (t). The symbol A_{tube} represents the cross sectional area of the tube cavity at a given z-location at a given time.

The continuity equation for an incompressible fluid in rectangular Cartesian coordinates is given as Equation (4.8). The ALE form of the Navier-Stokes equations for an incompressible Newtonian fluid in rectangular Cartesian coordinates is shown as Equations (4.9). These equations enforce the conservation of linear momentum and are valid on the domain of the fluid-filled tube cavity. Here u, v, and w are velocity components in the x-, y-, and z-directions respectively. In addition, c_x, c_y, and c_z are convective velocities in the x-, y-, and z-directions respectively.

$$\frac{\partial u}{\partial x} + \frac{\partial v}{\partial y} + \frac{\partial w}{\partial z} = 0 \tag{4.8}$$

$$
\begin{aligned}
&\text{x}-\text{Direction}: \left[\rho\left(\frac{\partial u}{\partial t}+c_x\frac{\partial u}{\partial x}+c_y\frac{\partial u}{\partial y}+c_z\frac{\partial u}{\partial z}\right)=-\frac{\partial p}{\partial x}+\mu\left(\frac{\partial^2 u}{\partial x^2}+\frac{\partial^2 u}{\partial y^2}+\frac{\partial^2 u}{\partial z^2}\right)\right]\\
&\text{y}-\text{Direction}: \left[\rho\left(\frac{\partial v}{\partial t}+c_x\frac{\partial v}{\partial x}+c_y\frac{\partial v}{\partial y}+c_z\frac{\partial v}{\partial z}\right)=-\frac{\partial p}{\partial y}+\mu\left(\frac{\partial^2 v}{\partial x^2}+\frac{\partial^2 v}{\partial y^2}+\frac{\partial^2 v}{\partial z^2}\right)\right] \qquad (4.9)\\
&\text{z}-\text{Direction}: \left[\rho\left(\frac{\partial w}{\partial t}+c_x\frac{\partial w}{\partial x}+c_y\frac{\partial w}{\partial y}+c_z\frac{\partial w}{\partial z}\right)=-\frac{\partial p}{\partial z}+\mu\left(\frac{\partial^2 w}{\partial x^2}+\frac{\partial^2 w}{\partial y^2}+\frac{\partial^2 w}{\partial z^2}\right)\right]
\end{aligned}
$$

The scaling in Equations (4.10) was introduced and used to form dimensionless variables. It is assumed that the tubes are long and narrow with half-length L and a tube cavity cross sectional hydraulic diameter D_h. The loading is an enforced sinusoidal displacement with frequency ω and amplitude A. Here $\overline{w}$ is the mean value of the z-component of the fluid velocity. The scaling for u and v was inferred from the continuity requirement that the divergence of the velocity field is zero. The scaling for pressure was based on the assumption that pressure forces in the z-direction are balanced by viscous shear forces in the z-direction. The cross section of the fluid domain is deformed as the tube cavity deforms. Therefore, the convective velocities of the fluid through the fluid domain in the x- and y-directions were assumed to be negligible. The fluid domain is not displaced in the z-direction. Therefore, the convective velocity in the z-direction is the fluid velocity in the z-direction.

$$
\begin{aligned}
w &\sim \overline{w} \\
u, v &\sim \frac{\overline{w} D_h}{L} \\
c_z &\sim \overline{w} \\
c_x, c_y &\sim 0 \\
x, y &\sim D_h \\
z &\sim L \\
t &\sim \frac{1}{\omega} \\
p &\sim \frac{\mu \overline{w} L}{D_h^2}
\end{aligned}
\tag{4.10}
$$

Dimensionless variables were introduced and given by Equations (4.11).

$$
\begin{aligned}
\hat{u} &= \frac{uL}{\overline{w} D_h} \\
\hat{v} &= \frac{vL}{\overline{w} D_h} \\
\hat{w} &= \frac{w}{\overline{w}} \\
\hat{x} &= \frac{x}{D_h} \\
\hat{y} &= \frac{y}{D_h} \\
\hat{z} &= \frac{z}{L} \\
\hat{t} &= \omega t \\
\hat{p} &= \frac{p D_h^2}{\mu \overline{w} L}
\end{aligned}
\tag{4.11}
$$

When the dimensionless variables (Equations (4.11)) were inserted into the Navier-Stokes equations (Equations (4.9)) and the results divided by ($\overline{w}$), the form shown below was produced. Each equation contains four individual terms separated by equal or addition symbols. In each equation the first term represents the local inertial forces, the second term represents the convective inertial forces, the third term represents the forces due to pressure, and the fourth term represents viscous shear forces.

$$\frac{\rho D_h \omega}{L}\frac{\partial \hat{u}}{\partial \hat{t}} + \frac{\rho \overline{w} D_h}{L^2}\left(\hat{w}\frac{\partial \hat{u}}{\partial \hat{z}}\right) = -\frac{\mu L}{D_h^3}\frac{d\hat{p}}{d\hat{x}} + \frac{\mu}{D_h L}\left(\frac{\partial^2 \hat{u}}{\partial \hat{x}^2} + \frac{\partial^2 \hat{u}}{\partial \hat{y}^2} + \frac{D_h^2}{L^2}\frac{\partial^2 \hat{u}}{\partial \hat{z}^2}\right)$$

$$\frac{\rho D_h \omega}{L}\frac{\partial \hat{v}}{\partial \hat{t}} + \frac{\rho \overline{w} D_h}{L^2}\left(\hat{w}\frac{\partial \hat{v}}{\partial \hat{z}}\right) = -\frac{\mu L}{D_h^3}\frac{d\hat{p}}{d\hat{y}} + \frac{\mu}{D_h L}\left(\frac{\partial^2 \hat{v}}{\partial \hat{x}^2} + \frac{\partial^2 \hat{v}}{\partial \hat{y}^2} + \frac{D_h^2}{L^2}\frac{\partial^2 \hat{v}}{\partial \hat{z}^2}\right)$$

$$\rho\omega\frac{\partial \hat{w}}{\partial \hat{t}} + \frac{\rho \overline{w}}{L}\left(\hat{w}\frac{\partial \hat{w}}{\partial \hat{z}}\right) = -\frac{\mu}{D_h^2}\frac{d\hat{p}}{d\hat{z}} + \frac{\mu}{D_h^2}\left(\frac{\partial^2 \hat{w}}{\partial \hat{x}^2} + \frac{\partial^2 \hat{w}}{\partial \hat{y}^2} + \frac{D_h^2}{L^2}\frac{\partial^2 \hat{w}}{\partial \hat{z}^2}\right)$$

As $D_h/L \rightarrow 0$, the local inertial and convective inertial terms of the x- and y-momentum conservation equations and the viscous shear force terms containing z-derivatives of the x-, y-, and z-momentum conservation equations go to zero. If $1/L << D_h$ as $D_h/L \rightarrow 0$, the entire viscous shear force terms of both the x- and y-momentum conservation equations go to zero. These conditions produce a reduced set of differential equations given as Equations (4.12) and (4.13).

$$\begin{aligned} &x - \text{Direction} : \frac{\partial p}{\partial x} = 0 \\ &y - \text{Direction} : \frac{\partial p}{\partial y} = 0 \end{aligned} \qquad (4.12)$$

$$\therefore p = p(z,t)$$

$$z-\text{Direction}:\left[\rho\omega\frac{\partial\hat{w}}{\partial\hat{t}}+\frac{\rho\overline{w}}{L}\left(\hat{w}\frac{\partial\hat{w}}{\partial\hat{z}}\right)=-\frac{\mu}{D_h^2}\frac{d\hat{p}}{d\hat{z}}+\frac{\mu}{D_h^2}\left(\frac{\partial^2\hat{w}}{\partial\hat{x}^2}+\frac{\partial^2\hat{w}}{\partial\hat{y}^2}\right)\right] \tag{4.13}$$

Since the pressure scaling used to get to this point was assumed, a set of conditions governing the validity of the pressure scaling must be extracted. The pressure scaling was based on the assumption that pressure forces in the z-direction balance viscous shear forces in the z-direction. For this to be true, the ratio of local inertial forces and convective inertial forces to viscous shear forces must be close to zero. In order to extract dimensionless parameters that represent these ratios, the coefficients of the local inertial term and the convective inertial term in the z-momentum conservation equation (Equation (4.13)) were divided by the coefficient of the viscous shear force term of Equation (4.13). This procedure produced dimensionless parameters that are called Parameter 1 and Parameter 2 in this work.

Parameter 1 is a form of the dimensionless number known as the frequency parameter. This number is known to be the product of the Reynolds number and the Strouhal number [21]. Parameter 2 is a form of the Reynolds number for the flow.

$$\text{Parameter 1}: \text{ (Local Inertial Forces) / (Viscous Forces)} = \frac{\rho\omega D_h^2}{\mu}$$

$$\text{Parameter 2}: \text{ (Convective Inertial Forces) / (Viscous Forces)} = \frac{\rho\overline{w}D^2{}_h}{\mu L}\sim\frac{\rho A\omega D_h}{\mu}$$

The second form of Parameter 2 $((\rho A\omega D_h)/\mu)$ shown above was obtained by assuming that the u and v velocities are of the magnitude of the amplitude and driving frequency product and referring to the previously stated scaling (Equations (4.10)). In the limit that both $(\rho\omega D_h^2)/\mu\to 0$ and $(\rho A\omega D_h)/\mu\to 0$, the ratio of pressure forces to

viscous forces is one. This condition is consistent with creeping or Stokes flow and is assumed from this point forward in the derivation.

If all the assumptions and conditions previously stated are satisfied, the simplified differential equation for conservation of linear momentum in the z-direction is Equation (4.14).

$$\frac{dp}{dz} = \mu\left(\frac{\partial^2 w}{\partial x^2} + \frac{\partial^2 w}{\partial y^2}\right) = \mu\nabla^2 w \tag{4.14}$$

A solution to Equation (4.14) is Equation (4.15). When this solution is inserted into Equation (4.14), it is apparent that $\nabla^2 f = -1$. The no-slip boundary condition applies on the inner surfaces of the fluid-filled cavity. Therefore, f(x,y,z,t) = 0 on these boundaries. If the pressure gradient is known, the Poisson's equation $\nabla^2 f = -1$ can be solved on a given tube cavity cross section at a given z-location and a given time, and the z-component of the fluid velocity is determined.

$$w(x,y,z,t) = -\frac{f(x,y,z,t)}{\mu}\frac{dp}{dz}(z,t) \tag{4.15}$$

When the average value theorem is applied to Equation (4.15) the expression for the average velocity in the z-direction, shown as Equation (4.16), is produced.

$$\overline{w}(z,t) = -\frac{A_{tube}(z,t)}{\mu \cdot K(z,t)}\frac{dp}{dz}(z,t)$$

$$\text{Where :} \tag{4.16}$$

$$K(z,t) = \frac{A_{tube}^2(z,t)}{\int_{A_{tube}} f(x,y,z,t)\cdot dxdy}$$

Equating Equation (4.7) and Equation (4.16) determines a relationship for the pressure gradient. This relationship appears as Equation (4.17).

$$\frac{dp}{dz}(z,t) = \frac{\mu \cdot K(z,t) \cdot \dot{\bar{A}}_{tube}(z,t)}{A^2_{tube}(z,t)} \cdot z \tag{4.17}$$

If the deformation of the tube is known, Equation (4.17) can be solved for the pressure gradient. Then, Equation (4.15) provides the z-component of the fluid velocity. If needed, the shear stresses can be calculated from the velocity. Equation (4.17) is then integrated, in conjunction with an exit pressure boundary condition, to obtain the fluid pressure as a function of z and t. If it is assumed that the deformation of the tube cavity is uniform along the length of the tube, the governing equations can be simplified further. With this assumption Equation (4.17) becomes Equation (4.18).

$$\frac{dp}{dz}(z,t) = \frac{\mu \cdot K(t) \cdot \dot{A}_{tube}(t)}{A^2_{tube}(t)} \cdot z \tag{4.18}$$

With zero pressure boundary conditions (p = 0 at z = -L and z = L), integrating Equation (4.18) produces Equation (4.19).

$$p(z,t) = -\frac{\mu \cdot K(t) \cdot \dot{A}_{tube}(t)}{2 \cdot A^2{}_{tube}(t)} \cdot \left(L^2 - z^2\right) \tag{4.19}$$

To get to this point it was assumed that 1/L is much smaller than D_h, D_h/L is very small, Parameter 1 ($(\rho\omega D_h^2)/\mu$) and Parameter 2 ($(\rho A\omega D_h)/\mu$) are very small, and that the tube deformation is uniform along the length. Inspection of Equations (4.16) and (4.18) shows that the magnitude of the fluid velocity changes along the tube length. Therefore, the fluid experiences local and convective forces. However, if the sum of

these forces is small compared to the viscous forces experienced by the fluid, these inertial effects may be neglected.

4.2.2. Finite Element Model and Numerical Results Using Simplified Equations and Two Dimensional Assumption

Equation (4.18) was used to construct a plane strain model to simulate the through-the-thickness compression of a tube/matrix cell of a composite lamina composed of fluid-filled tubes embedded in an elastomer matrix. PATRAN 2003 was the preprocessor. ABAQUS 6.3 was the processor and ABAQUS 6.3 Viewer was the postprocessor. Geometric nonlinearities were considered in the models.

4.2.3. Model Rationale

The through-the-thickness compression of a tube/matrix cell of composite lamina was modeled as a plane strain problem, since the tubes are assumed to be very long. A complementary assumption is that the composite lamina is very wide, which means that there is a very large array of cells. Therefore, the vertical sides of the tube/matrix cell are symmetry planes. Figure 4.9 points out additional tube material added on the top and bottom surface of the tube cavity geometry shown in Figure 3.4. These extensions decrease the cavity hydraulic diameter without significantly increasing the stiffness of the structure. According to the pressure scaling of Section 4.2.1, decreasing the tube hydraulic diameter increases the pressure generated. Therefore, the extra material should improve damping performance by raising the fluid pressure without increasing the structural stiffness. The exact dimensions used are shown in Figure 4.10. The tube volume fraction is 0.243 and the fluid volume fraction is 0.075.

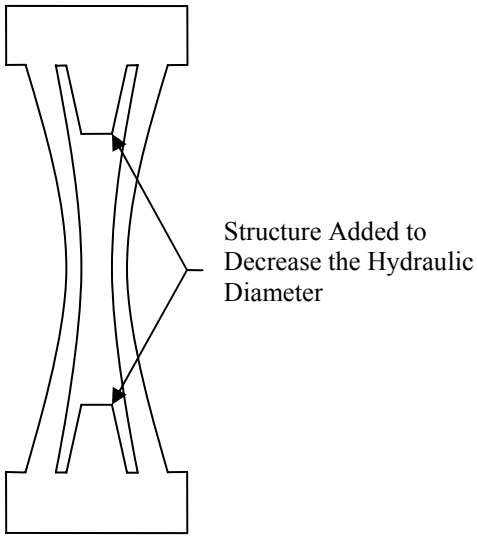

Figure 4.9. Diagram identifying additional structure used to reduce hydraulic diameter of tube cavity.

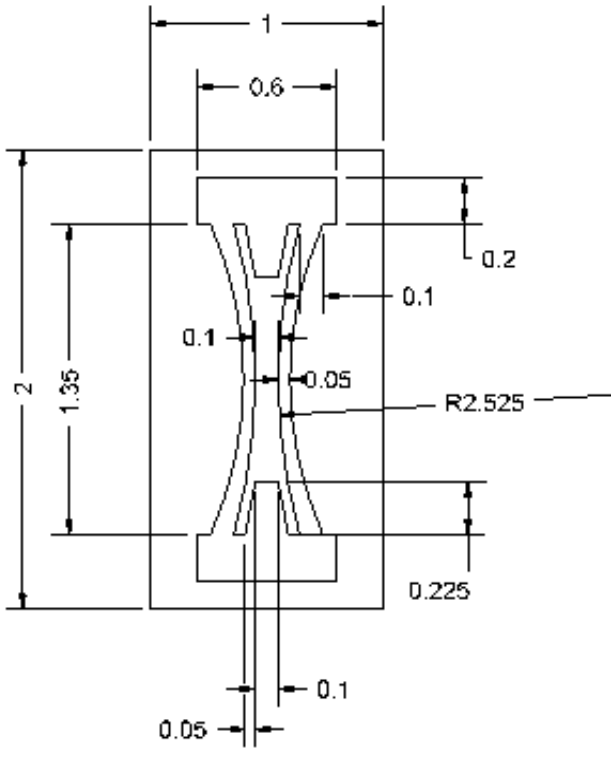

Figure 4.10. Dimensions of a tube/matrix cell in millimeters.

The assumption that the tube cross sectional area remains constant along the tube length during deformation makes a 2-D structural representation sufficient. The pressure predicted by Equation (4.19) shows a quadratic distribution along the length of the tube. The average pressure predicted is applied to the cavity surface of the plane strain model.

Determining the dimensionless parameter K in Equation (4.19) requires solving the Poisson's equation discussed in Section 4.2.1 at each time step. The geometry of the tube cross section makes this a difficult analytical problem. So, a finite element code was written in FORTRAN. The code determines K for the undeformed tube cavity cross section. The finite element code uses bi-quadratic, 9-node quadrilateral finite elements. First, the Poisson's equation $\nabla^2 f = -1$ with $f = 0$ on the boundaries of the cavity is solved. Then, the code calculates the area of the mesh and the integral of the solution using Gauss-Legendre quadrature numerical integration. Finally, these values are used to calculate K using Equation (4.16). It was assumed that this value does not change significantly during deformation, and the value calculated for the undeformed cross section was used through the entire ABAQUS computation.

4.2.4. Benchmarking for the K Parameter Determination Routine

A circular cross sectional geometry was chosen as a test case because an exact solution of the cylindrical coordinate version of Equation (4.14) is known. The velocity solution for a circular cross section is Equation (4.20) [21]. For this case the extracted function f is Equation (4.21).

$$w(r) = \left(\frac{dp}{dz} \cdot \frac{D^2}{16\mu}\right)\left[1 - \left(\frac{2r}{D}\right)^2\right] \tag{4.20}$$

$$f(r) = \left(\frac{D^2}{16}\right)\left[1 - \left(\frac{2r}{D}\right)^2\right] \tag{4.21}$$

The dimensionless parameter K for a circular geometry was determined by integrating Equation (4.21) over the area of a circle with diameter D and dividing by A^2 where A is the circle's area. When this process was carried out, it was found that for a circle the dimensionless parameter K is 8π or approximately 25.13.

The finite element model used was one quarter of the circle. The mesh contained seven 9-node, bi-quadratic finite elements and 39 nodes. For this problem any radial line is a symmetry line. The horizontal and vertical radial lines were chosen because they coincide with the x-axis and y-axis respectively. The nodal degrees of freedom on the circumference of the circle were specified as zero. The nodal degrees of freedom along the radial lines were not specified. This is the same as applying a symmetry boundary condition, since the derivative of the solution normal to the radial lines was taken as zero on the radial lines. The radius used for the computation was 1 meter. This value was chosen for simplicity. The same result would be obtained with any radius and any unit system due to the dimensionless nature of the parameter K.

The value obtained by the finite element analysis was 25.13, which matches the analytical result exactly to four significant digits. This accuracy is accomplished with a small number of elements due to the bi-quadratic order of the finite elements used. A model using bi-linear elements may require a much larger number of elements to obtain an accurate solution.

4.2.5. Determination of K Parameter and Comparison with Other Shapes

The FORTRAN program described in the previous section was used to determine the K parameter for the undeformed cavity shape of Figure 4.10. The mesh contained sixty-four 9-node bi-quadratic finite elements. The node total was 305. Only the top right quadrant of the tube cross section was modeled. Along the perimeter of the cavity, the nodal degrees of freedom were set to zero. Along the symmetry planes, no nodal degrees of freedom were specified. The K parameters for the undeformed geometries of Figure 3.1, Figure 3.4, and a square were also calculated using the program. Table 4.4 shows the values obtained along with the hydraulic diameters of each. Notice that the

geometry of Figure 4.11 has a higher value of the dimensionless parameter K than any of the other shapes considered. It also has a smaller hydraulic diameter than the geometries of Figures 3.1 and 3.4.

Table 4.4. K parameter and hydraulic diameter for various tube geometries.

Shape	K	Hydraulic Diameter
Circle	25.13	D
Square	28.46	L
Figure 3.1. Geometry	106.06	0.2208 mm
Figure 3.4. Geometry	113.17	0.2631 mm
Figure 4.11. Geometry	167.02	0.1489 mm

4.2.6. Element Selection

The element types, characteristics, and the number of each type used in the mesh are presented in Table 4.5. Details of ABAQUS elements come from Reference [22]. The element type CPE4 modeled the tube material. This is a plane strain, 4-node quadrilateral finite element. Its displacement formulation is bilinear with x- and y-displacement degrees of freedom at each node.

The element type used to model the matrix material was CPE4H. This is a plane strain, 4-node quadrilateral finite element. It uses a mixed u-p formulation that is bilinear in displacements and constant in pressure. Both x- and y-displacement degrees of freedom are carried at each node, and element constant pressure is carried as a Lagrangian multiplier.

F2D2 hydrostatic fluid elements were used as a port to apply cavity pressure and to determine fluid cavity volume. The fluid cavity volume was used to calculate the fluid cavity cross sectional area. These are 2-D line elements that model fluid cavities with uniform internal pressure. The F2D2 finite element has 2 nodes with x- and y-displacement degrees of freedom at each node. These elements are meshed around the boundary of a 2-D fluid cavity, and a reference node is defined and associated with the

fluid cavity. The software calculates the fluid cavity pressure and volume and reports these values at the fluid cavity reference node.

The element unit normal vectors for element types CPE4 and CPE4H should point in the positive z-direction. Also, the element unit normal vectors for the F2D2 element should point toward the interior of the fluid cavity to ensure the proper sign convention for cavity pressure.

Table 4.5. Element descriptions for Section 4.2.

Element Type	**Number in Mesh**	**Number of Nodes**	**Degrees of Freedom**	**Sketch**
CPE4 Plane Strain, Displacement Formulation, Quadrilateral, Continuum Element	1952	4	Linear x- and y-Displacements	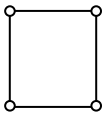
CPE4H Plane Strain, Mixed u-p Formulation, Quadrilateral, Continuum Element	3680	4	Linear x- and y-Displacements	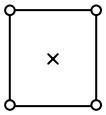
		1 Internal	Element Constant Pressure	
F2D2 Hydrostatic Fluid Cavity Element	224	2	Linear x- and y-Displacement	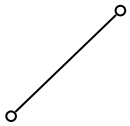
		1 Reference Node Per Fluid Cavity	Fluid Cavity Pressure and Volume	

4.2.7. Model Generation and Solution Process

The tube/matrix cell geometry, the finite element mesh, and the node sets for the applied boundary conditions were generated using PATRAN 2003. Lengths were in

millimeters. Elastic moduli were entered in MPa and viscosities in $N \cdot s/mm^2$. Displacements were in millimeters and pressures and stresses were in MPa.

Care was taken to properly connect the elements representing the tube, the matrix, and the fluid cavity. This was accomplished using PATRAN's EQIVALENCE command. This command assigns the same global node number to coincident nodes.

Next, boundary conditions were applied. Figure 4.11 shows the displacement boundary conditions. Symmetry boundary conditions (x-displacements equal to zero) were applied to the outer left and right vertical walls. A zero y-displacement boundary condition was applied to the bottom surface of the tube/matrix cell. Specified time varying top surface y-displacements and the fluid cavity pressure were applied by ABAQUS user subroutines. The *STEP, STATIC, NLGEOM command is used to define the static time step for the time incrementing process and to include nonlinear geometric effects in the analysis.

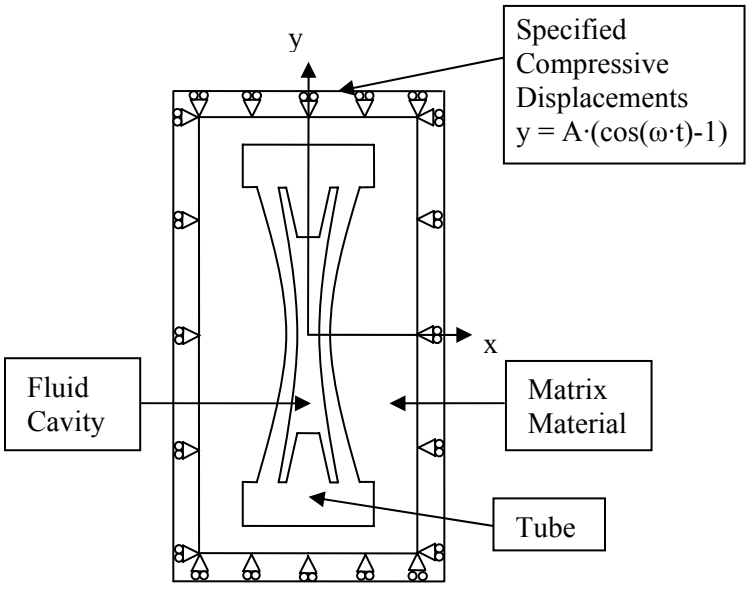

Figure 4.11. Boundary conditions and material regions for Section 4.2.

Two user subroutines adjust the internal fluid cavity pressure as a function of the deformation and deformation rate of the cavity. The subroutines also control the y-displacement for the top surface of the tube/matrix cell. These user-written subroutines are named URDFIL and DISP by ABAQUS. They are written in the FORTRAN 77 programming language. Subroutine URDFIL searches the results file (.fil) for data needed to update the model inputs. For example, the fluid cavity volume of the last completed increment is located by URDFIL. The analysis can also be terminated using URDFIL. Subroutine DISP can update the model inputs controlled by the *BOUNDARY command. In the model input file the *BOUNDARY command specifies the fluid cavity pressure and the top surface displacement.

In the model input file, the y-displacement boundary conditions move the top surface of the tube/matrix cell. The displacement versus time data is placed in a text file (dispcrv1.txt) and read by the subroutine DISP for each time step. For this model the specified top surface displacement defines a displacement rate, since the fluid model (Equation (4.19)) gives a rate-dependent response. As mentioned earlier, fluid cavity elements line the interior surfaces of the tube's fluid cavity. This fluid cavity has a single reference node where the cavity pressure and volume data are stored. The pressure is specified to apply the fluid response found by Equation (4.19), defined in Section 4.2.1. Control of both the top surface displacement and the cavity pressure are routed to subroutine DISP by using the USER option with the *BOUNDARY command for the boundary condition definition in the model input file.

Automatic time step adjustments were allowed and the length of the total step time and maximum number of increments were made very large to ensure that there were a sufficient number of increments to allow the fluid model (Equation (4.19)) to converge for every time step. Static time step increments in ABAQUS were iterations for convergence on internal cavity pressure. This means that not all of the time steps that the analysis writes to the ABAQUS solution database are valuable other than as a means to iterate for convergence of the pressure response equation. The user subroutine URDFIL terminates the analysis when the specified displacement curve is completed.

Both subroutines URDFIL and DISP were saved in a single subroutine file (sub_fluid.f).

The user must input certain data into the file sub_fluid.f for each analysis. In sub_fluid.f the undeformed cavity volume, the pressure equation coefficient K, the number of time steps, an initial pressure increment size, the reference pressure at the ends of the tube, the length of the tube, and a convergence tolerance must be supplied by the user.

The problem is analyzed by the following process that is shown in Figure 4.12: First, the top surface displacement is incremented by the first displacement step. ABAQUS solves the large displacement elasticity problem for the structure and writes the deformed fluid cavity volume. Subroutine URDFIL then searches the results file for the deformed fluid cavity volume. A COMMON block stores variables used by both URDFIL and DISP. Next, DISP increments the fluid cavity pressure by the user-specified initial pressure increment for the first iteration or the pressure increment predicted by the secant method for subsequent iterations. DISP also calculates the magnitude of the error between the last fluid cavity pressure value and the average pressure predicted by Equation (4.19). The error and the change in the error from the last iteration are used to approximate the rate of change of error with respect to average cavity pressure and to predict the next pressure increment by the secant method. If the magnitude of the change in pressure between two iterations is less than or equal to the user-specified convergence tolerance, the average pressure solution for that time step is taken as the last-used fluid cavity pressure and the solution is considered converged.

If the solution has not converged the fluid cavity pressure is incremented by the new predicted pressure change, and ABAQUS again solves the nonlinear elasticity problem. Subroutine URDFIL again reads the results file, and this process continues until convergence occurs. The equilibrium data is written to a file (good.dat) to distinguish between the actual solution and those incorrect solution attempts that are written to the ABAQUS solution database.

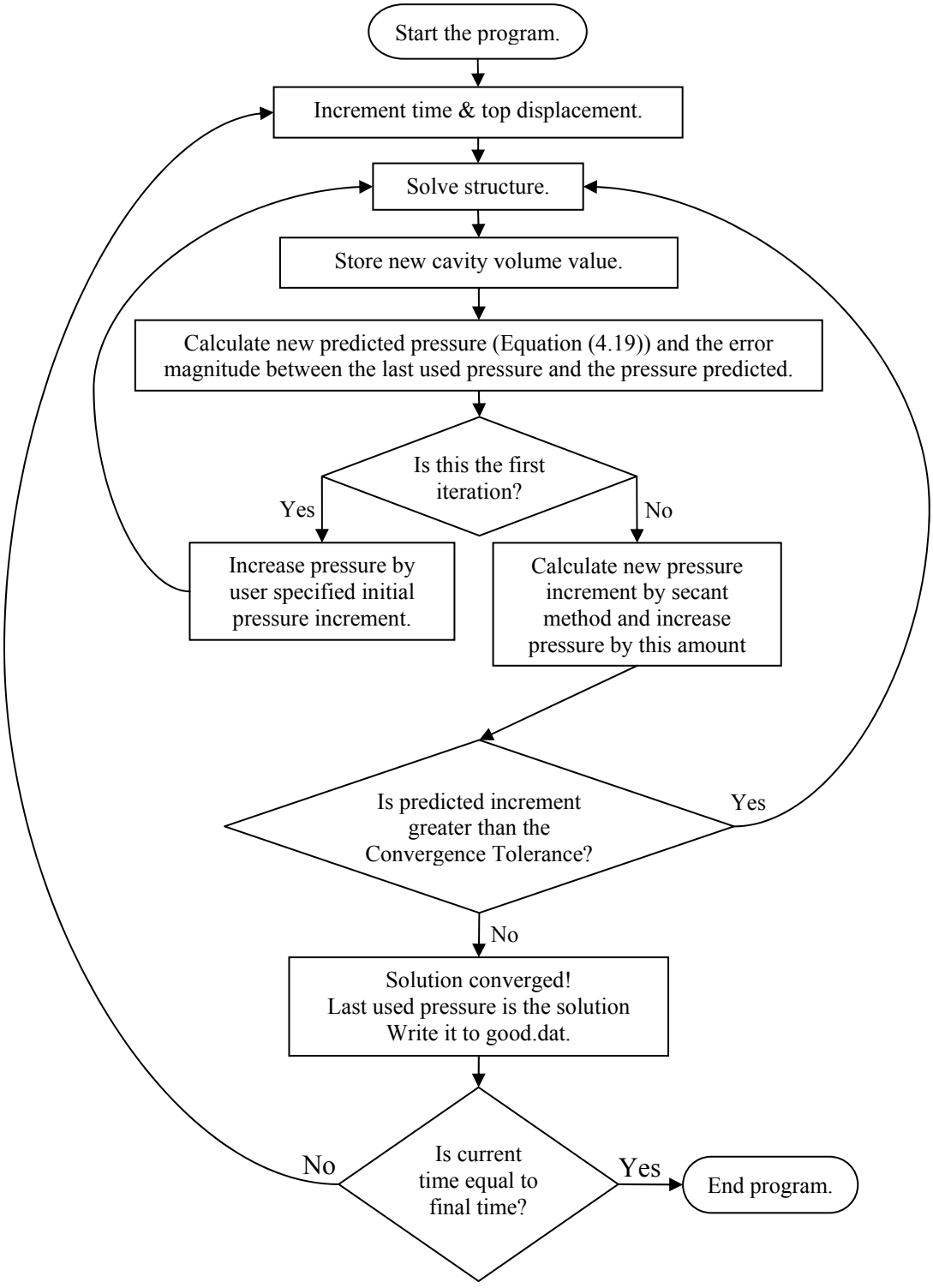

Figure 4.12. Flow chart of the solution process.

After each convergence, the current time value is then compared to the final time value. If the time values are not found to be equal, time and the top surface displacement are incremented to the value for the next time step and the process continues. Once the current and final time values are equal, the process is complete and the program is exited. Appendix A is the full subroutine file sub_fluid.f.

4.2.8. Material Properties and Constitutive Models Used in the Analyses

The tube is described with the same constitutive model and material properties as those of Section 3.2.2. The Matrix material is described with the same constitutive model and material properties as Matrix Material 1 in Section 3.2.2. The material properties appear is Table 3.3.

4.2.9. Numerical Results of Simplified Two Dimensional Models for the Study of Effects of Length and Viscosity Change

There are two questions that this section addresses. The first is: how does changing the tube length affect the pressure production in the tubes? The second is: how does changing fluid viscosity affect the pressure production in the tubes?

A numerical study was conducted using the simplified model described in Sections 4.2.1-4.2.8 to predict of the effect of changing tube length. Equation 4.19 shows a quadratic variation in pressure as a function of tube length when all other terms in the equation are constant. The pressure will only increase as the length squared if the increase in pressure does not alter the response of the structure.

The study concerns five length values: 20, 40, 60, 80, and 100 mm. A fluid dynamic viscosity of 1 poise was used, and a 0 to -1 % sinusoidal engineering strain was applied at a driving frequency of 50 Hz.

Figure 4.13 presents the pressure results at the middle of the tube. The figure shows that there is an approximately sinusoidal pressure distribution as a function of time with the maximum pressure magnitudes occurring at the time of maximum top surface downward velocity magnitude. Note the top surface displacement was applied as a

function of the form $A\cdot(\cos(\omega\cdot t)-1)$. Therefore, the top surface velocity is of the form $-A\cdot\omega\cdot\sin(\omega\cdot t)$, and the maximum velocity magnitudes occur at one quarter of a cycle and three quarters of a cycle. The amplitude of the pressure increases as the length of the tube increases. This leads into the question of what relationship exists between the upper and lower bounds and length of the tube.

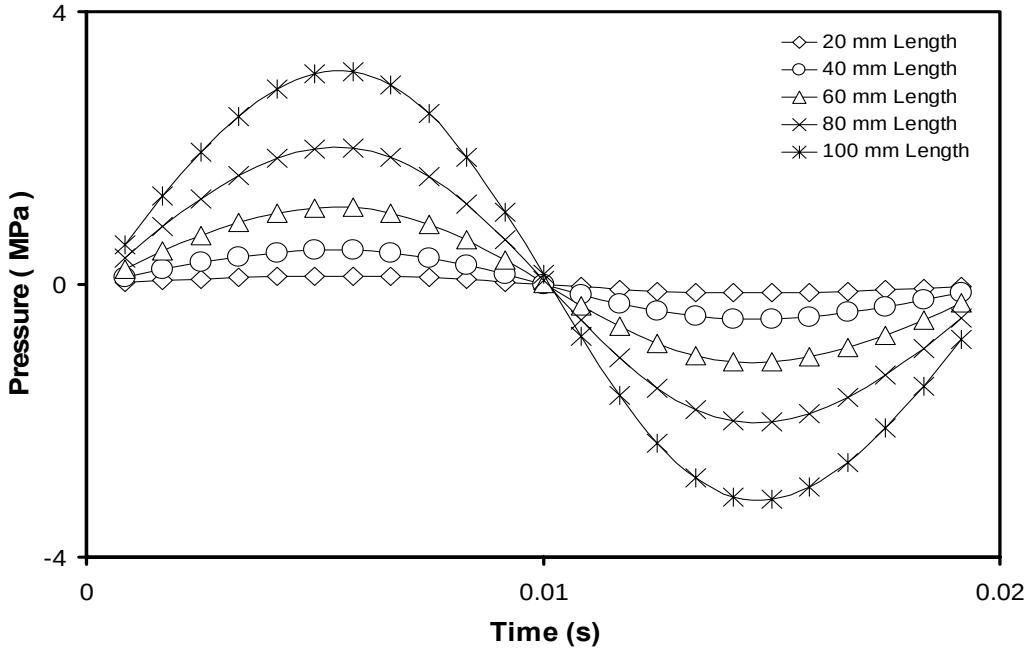

Figure 4.13. Tube center pressure for one cycle with 1 poise fluid viscosity and a 0 to -1 % sinusoidal engineering strain applied at a driving frequency of 50 Hz.

Figure 4.14 shows the variation in minimum and maximum pressure during one cycle of forced vibration. The results show a quadratic distribution of pressure as compared to tube length. A quadratic regression fits the upper curve with a R^2 value of 1. The resulting equation is $P_{MAX} = 0.0012\cdot L^2 + 0.0004\cdot L$, where L is the tube half-length. A quadratic regression fits the lower curve with a R^2 value of 1. The resulting equation is $P_{MIN} = -0.00012\cdot L^2 + 12E\text{-}05\cdot L$.

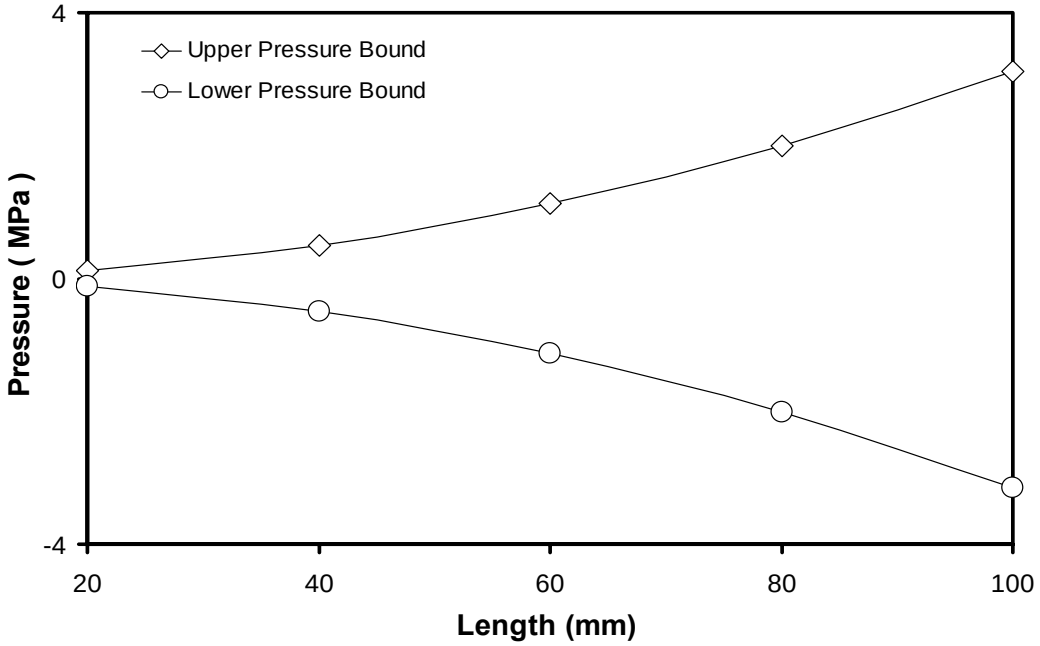

Figure 4.14. Pressure extremes for one cycle with 1 poise fluid viscosity and a 0 to -1 % sinusoidal engineering strain applied at a driving frequency of 50 Hz.

The pressure was directly predicted by Equation (4.19). From reviewing Equation (4.19) it is observed that if the tube experiences the same deformation regardless of the pressure applied to it and the fluid viscosity and time are fixed, then Equation (4.19) is of the form $C \cdot L^2$, where C is constant. The curve fits have the form $a \cdot L^2 + b \cdot L$, where a and b are constant. The existence of the constant b shows that the tube deformation is influenced to some degree by the pressure increase resulting from the length increase. Another way to show this is to take the maximum pressure calculated for a length of 20 mm and divide it by $(20 \text{ mm})^2$. This will yield C for that length. Then, in order to predict the pressure for a new length, multiply this number by the square of the tube length for which the maximum pressure prediction is desired. The deviation in the pressures predicted in this way from the values obtained from the model give a measure of the change in the response of the tube as the pressure increases. Table 4.6 shows the

values calculated in this manner as compared to the actual values obtained from the computational model.

The data of Table 4.6 show that the increase in pressure does not significantly change the deformation of the cross section of the fluid cavity in the range of length values analyzed, at least according to a computation assuming that the deformation of the tube is uniform along its length. It does make sense that this could be the case; since the matrix material is incompressible, the matrix volume must be conserved. However, more force is required to cause the deformation as the length is increased.

Table 4.6. Agreement of quadratic pressure assumption.

Length (mm)	**Quadratic Pressure (MPa)**	**Pressure from Model (MPa)**	**% Error**
40	0.502	0.502	0.000
60	1.130	1.128	0.177
80	2.009	2.001	0.400
100	3.139	3.118	0.674

The second question addressed in this study was how does changing fluid viscosity affect the pressure production in the tubes. The simplified model (Equation (4.19)) predicts a linear variation in pressure as a function of fluid dynamic viscosity when all other terms are constant. The pressure will only increase linearly with increasing fluid dynamic viscosity if the increase in pressure does not alter the response of the structure.

The study concerns five viscosity values: 2, 4, 6, 8, and 10 poise. A tube length of 40 mm was fixed, and a 0 to -1 % sinusoidal engineering strain was applied at a driving frequency of 50 Hz for all five analyses. Figure 4.15 presents the results. The figure shows that there is an approximately sinusoidal pressure distribution in time and that the pressure amplitude increases as the viscosity of the fluid in the tube increases. This leads into the question of what relationship exists between the upper and lower pressure bounds and viscosity of the fluid.

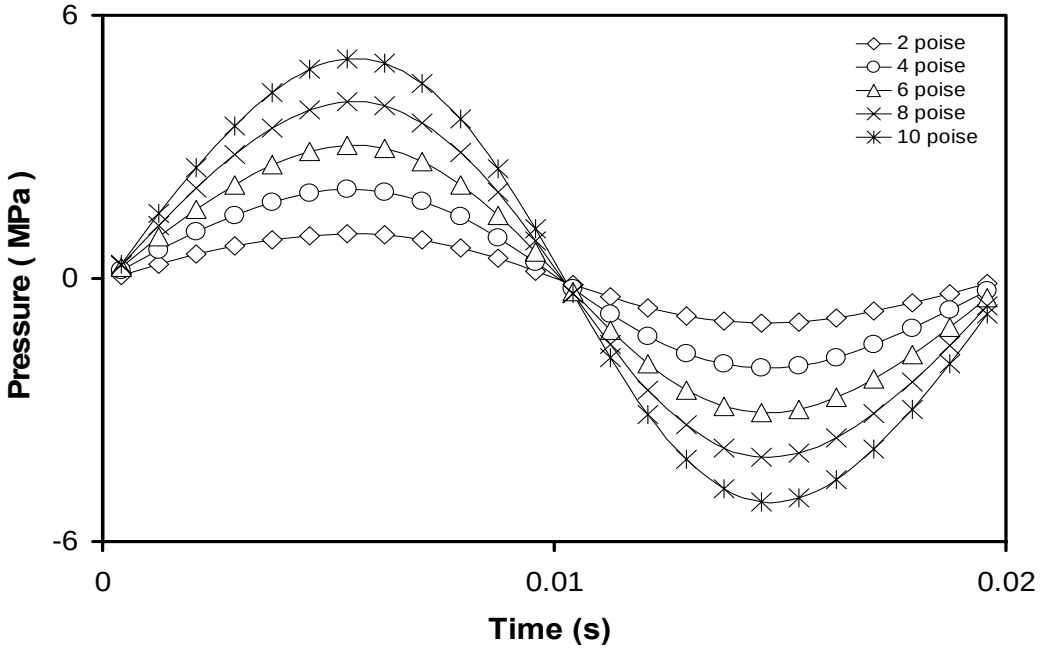

Figure 4.15. Tube center pressure for one cycle with 40 mm tube length and a 0 to -1 % sinusoidal engineering strain applied at a driving frequency of 50 Hz.

Figure 4.16 shows the variation in minimum and maximum pressure during one cycle of forced vibration. The results do show a distribution of pressure as compared to fluid viscosity that is very close to linear. A linear regression will fit the upper curve with a R^2 value of 0.9999. The resulting equation is $P_{MAX} = 0.5031 \cdot \mu$. A quadratic regression will fit the upper curve with a R^2 value of 1. The resulting equation is $P_{MAX} = -0.0011 \cdot \mu^2 + 0.5118 \cdot \mu$. The relative size of the coefficients shows that the structural deformation is only slightly affected by the increasing pressure in the range of viscosity studied. A linear regression will fit the lower curve with a R^2 value of 1. The resulting equation is $P_{MIN} = -0.5095 \cdot \mu$.

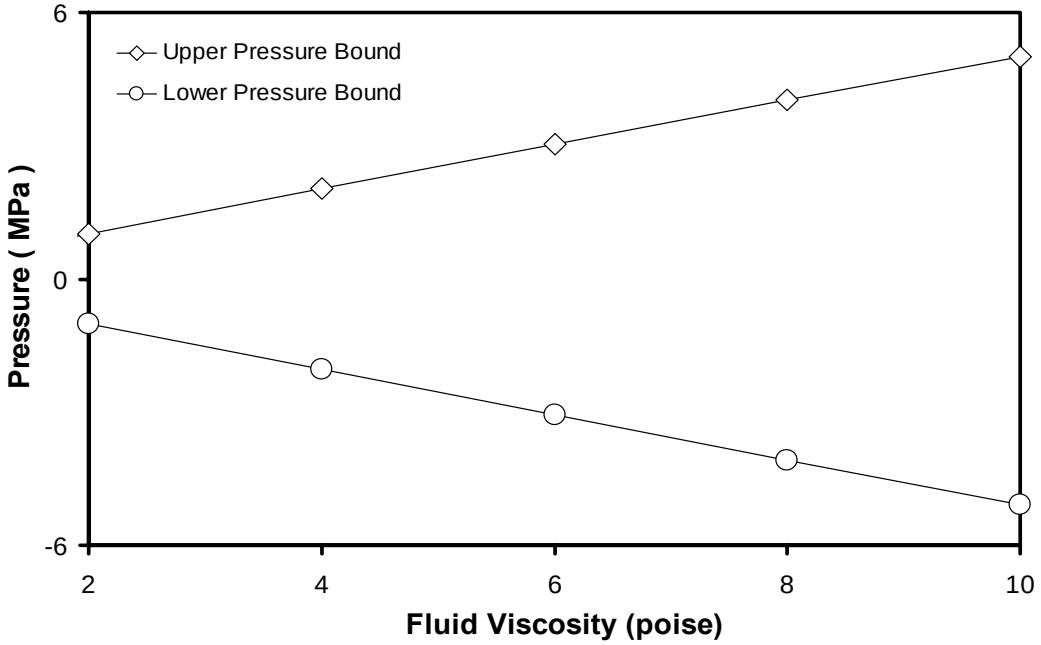

Figure 4.16. Pressure extremes for one cycle with 40 mm tube length and a 0 to -1 % sinusoidal engineering strain applied at a driving frequency of 50 Hz.

4.3. Specific Damping Capacity Definitions

Specific damping capacity is a term used in following sections to quantify the damping performance of machine augmented composite materials. The term is often used to refer to various quantities that have different physical meanings. In order to avoid confusion, it is necessary to discuss the definition of specific damping capacity used in this work as compared to another definition that is sometimes used by others.

There are several definitions of specific damping capacity in the literature. This work uses the definition developed by Lee and Hartmann [3]; it is the ratio of energy dissipated to work input through one steady-state cycle ($(\text{Efficiency})_{\text{Cycle}}$). This is the energy dissipation efficiency and the highest possible dissipation is one. The relationship between this definition of specific damping capacity and the phase lag (δ) between stress and strain when a linearly viscoelastic material is subjected to a sinusoidal excitation is expressed by Equation (4.22) [3]. This relationship is valid for

arbitrarily large δ, but it was derived for sinusoidal stress and strain curves that oscillate about zero. Therefore, it is not valid in situations where the stress and strain do not oscillate about zero.

$$(\text{Efficiency})_{\text{Cycle}} = \frac{\pi \tan(\delta)}{\left[1+\left(\frac{\pi}{2}+\delta\right)\tan(\delta)\right]} = \text{Specific Damping Capacity} \tag{4.22}$$

An alternate definition of specific damping capacity, which differs from the definition used in this work, is the ratio of energy dissipated to the maximum energy stored in a steady-state cycle of deformation. The maximum energy stored in steady-state cycle is difficult to obtain directly. As stated earlier, the energy dissipation efficiency of a material is the ratio of the dissipated energy to the total energy put into the material by boundary work per steady-state cycle; notice this is the definition of specific damping capacity used in this work. The ratio of the energy stored to the total energy input is equal to one minus the efficiency. If the efficiency is divided by this number, the ratio of the energy dissipated to the energy stored is produced; notice this is the alternate definition of specific damping capacity. Equation (4.23) shows the relationship between this alternate definition and the definition used in this work. Due to this correspondence, values presented in this study may be converted to the alternate definition. Notice that the definition used in this work has a range from 0 to 1 while the alternate definition has a range from 0 to ∞.

$$(\text{Energy Dissipated})/(\text{Energy Stored}) = \frac{(\text{Efficiency})_{\text{Cycle}}}{\left(1-(\text{Efficiency})_{\text{Cycle}}\right)} \tag{4.23}$$

4.4. Dimensional Analysis of the Fluid-Structure Interaction Problem

Dimensional analysis is attractive because it reduces the number of variables in a problem by condensing the original dimensional variables into a smaller set of dimensionless variables. These dimensionless variables can often give insight into the physics involved in a particular problem. A problem can contain up to three reference dimensions. For example, these can be force (F), length (L), and time (T), or mass (M), length (L), and time (T). The number of variables may be reduced by the number of reference dimensions present in the problem.

The energy dissipating efficiency of a composite material formed by fluid-filled tubes with zero pressure end conditions embedded inside an elastomer matrix is described by a function of the form shown as Equation (4.24).

$$\text{Efficiency} = f\left(\rho_f, \rho_i, \mu, E_i, \nu_i, H, W, l_j, L_T, A, \omega, t\right) \tag{4.24}$$

The pressure generated at a given location inside a tube is described by a function of the form shown as Equation (4.25).

$$P = q\left(\rho_f, \rho_i, \mu, E_i, \nu_i, H, W, l_j, L_T, A, \omega, t\right) \tag{4.25}$$

Also, the fluid velocity in the length direction at a given position within the tube is described by a function of the form shown as Equation (4.26).

$$V = i\left(\rho_f, \rho_i, \mu, E_i, \nu_i, H, W, l_j, L_T, A, \omega, t\right) \tag{4.26}$$

Table 4.7 contains the variable definitions and their dimensionality. The index i ranges from 1 to the number of solid materials in the composite and j ranges from 3 to the minimum number of dimensions needed to describe the tube/matrix cell cross section. If the governing differential equations have a unique solution, the validity of Equations (4.24)-(4.26) is certain because these functions contain all the independent

variables that can be changed within the governing equations, the loading, and the definition of the problem domain.

Buckingham Pi theorem states that if an equation involving k variables is dimensionally homogeneous, it can be reduced to a relationship among k – r independent dimensionless products, where r is the minimum number of reference dimensions required to describe the variables. The only requirements on these new variables are that there are a correct number of them and that they be independent and dimensionless [21]. These variables are called Pi terms. There is not a unique set of Pi terms. Many sets may exist and be equally valid.

Table 4.7. Variables and their dimensions.

Variable	Definition	Dimensions
Efficiency	Energy Dissipated / Work Input	Dimensionless
P	Pressure	$M L^{-1} T^{-2}$
V	Velocity in Length Direction	$L T^{-1}$
ρ_f	Density of Fluid	$M L^{-3}$
ρ_i	Density of Solid Material i	$M L^{-3}$
μ	Fluid Viscosity	$M L^{-1} T^{-1}$
E_i	Modulus of Elasticity of Solid Material i	$M L^{-1} T^{-2}$
ν_i	Poisson's Ratio of Solid Material i	Dimensionless
H	Height of Tube/Matrix Cell	L
W	Width of Tube/Matrix Cell	L
l_j	Length j that Describes the Cross Section of Tube/Matrix Cell (Not Including H and W)	L
L_T	Half-Length of Embedded Tubes	L
A	Amplitude of Sinusoidal Displacement	L
ω	Driving Frequency	T^{-1}
t	Time	T

Equations (4.24)-(4.26) contain three reference dimensions: M, L, and T. Therefore the number of variables in each of these equations may be reduced by three by applying the Buckingham Pi theorem. The resulting relationships are shown as Equations (4.27)-(4.29). Notice that the efficiency and Poisson's ratios are Pi terms since they are

dimensionless and represent the ratios of certain quantities without any manipulation. It should again be noted that the dimensionless variables in Equations (4.27)-(4.29) are not unique. Other valid forms exist. These particular independent variables were chosen because they have important physical meaning. For example, the first independent variable ($\rho_i H^2\omega^2/E_i$) is a measure of the ratio of inertial forces to elastic forces in the solid materials. The second ($\rho_f A\omega H/\mu$) is a measure of the ratio of convective inertial forces to viscous forces in the fluid. The third ($E_i/(\omega\mu)$) is a measure of the ratio of elastic forces in the solid to viscous forces in the fluid.

$$\text{Efficiency} = g\left(\frac{\rho_i H^2\omega^2}{E_i}, \frac{\rho_f A\omega H}{\mu}, \frac{E_i}{\omega\mu}, \nu_i, \frac{H}{L_T}, \frac{W}{H}, \frac{l_j}{L_T}, \frac{A}{H}, \omega t\right) \tag{4.27}$$

$$\frac{P}{\omega\mu} = r\left(\frac{\rho_i H^2\omega^2}{E_i}, \frac{\rho_f A\omega H}{\mu}, \frac{E_i}{\omega\mu}, \nu_i, \frac{H}{L_T}, \frac{W}{H}, \frac{l_j}{L_T}, \frac{A}{H}, \omega t\right) \tag{4.28}$$

$$\frac{V}{\omega L_T} = j\left(\frac{\rho_i H^2\omega^2}{E_i}, \frac{\rho_f A\omega H}{\mu}, \frac{E_i}{\omega\mu}, \nu_i, \frac{H}{L_T}, \frac{W}{H}, \frac{l_j}{L_T}, \frac{A}{H}, \omega t\right) \tag{4.29}$$

These equations suggest that for a fixed geometry, fixed densities, fixed solid elastic moduli, fixed displacement amplitude, and fixed time, the only parameters remaining to vary are the fluid viscosity μ and the driving frequency ω. Under these constraints Equations (4.27)-(4.29) require only one unique combination of μ and ω to produce a certain set of dependent variables.

Now consider the case where the combination of material properties, loading, and geometry is such that inertial forces are negligible. This condition is attained when the forces due to inertial effects are very small compared to the elastic and viscous forces. This is consistent with quasi-static solid deformation and creeping fluid flow. One set of conditions under which it is reasonable to assume this is when the solid materials have

low densities in addition to high stiffness and the fluid has low density in addition to high viscosity. This assumption makes all Pi terms containing densities in Equations (4.27)-(4.29) zero. Furthermore, if Equation (4.27) is integrated in the variable $\omega \cdot t$ through the closed bound of one steady-state cycle, the single cycle efficiency is obtained. In this work this value is called the specific damping capacity. This integration results in the dependence on the variable $\omega \cdot t$ being removed from Equation (4.27). After these simplifications and assumptions, Equations (4.27)-(4.29) reduce to Equations (4.30)-(4.32).

$$(\text{Efficiency})_{\text{Cycle}} = h\left(\frac{E_i}{\omega \cdot \mu}, \nu_i, \frac{H}{L_T}, \frac{W}{H}, \frac{l_j}{L_T}, \frac{A}{H}\right) = \text{Specific Damping Capacity} \qquad (4.30)$$

$$\frac{P}{\omega\mu} = s\left(\frac{E_i}{\omega \cdot \mu}, \nu_i, \frac{H}{L_T}, \frac{W}{H}, \frac{l_j}{L_T}, \frac{A}{H}, \omega t\right) \qquad (4.31)$$

$$\frac{V}{\omega L_T} = k\left(\frac{E_i}{\omega \cdot \mu}, \nu_i, \frac{H}{L_T}, \frac{W}{H}, \frac{l_j}{L_T}, \frac{A}{H}, \omega t\right) \qquad (4.32)$$

Consider the case of fixed geometry, fixed fluid density, fixed displacement amplitude, and fixed solid material moduli. Equation (4.30) shows that the same efficiency is obtained for two systems if $\omega \cdot \mu$ is the same for these systems. Therefore, when inertial forces are negligible, there are infinitely many combinations of ω and μ that will produce a certain value of specific damping capacity; the only constraint is that their product is the same.

The first dimensionless parameter listed in functions h, s, and k ($E_i/(\omega \cdot \mu)$) is a measure of the ratio of elastic forces to viscous forces. It is logical for this parameter to influence the damping performance of the machine augmented composite material. The validity of these assumptions will be evaluated through computational experiments in Section 4.5.1.

4.5. Transient, Three Dimensional Modeling of Embedded, Fluid-Filled Tubes with Zero Pressure End Conditions

In this section it is desired to model a tube/matrix cell of a machine augmented composite (MAC) material by using finite element models that solve the full transient, three dimensional Navier-Stokes equations and the transient, three dimensional equations of elasticity with large deformations. This is worthwhile because no assumptions are introduced other than those associated with choosing the appropriate constitutive models. This was accomplished by the use of ANSYS 6.1 finite element software. These finite element models were used to determine the validity of the scaling rules developed in Section 4.4. The transient, three dimensional models were also used to determine the effect of changing material properties, loading, and tube geometry. Results from these models were also compared to results obtained from the simplified model developed in Section 4.2.

ANSYS 6.1 and higher versions have a specialized fluid-structure interaction solver. A mesh partitioning method is used, and the structural and fluid domains are solved separately. A Picard iterative method is used to find equilibrium between the two domains. The ANSYS fluid-structure interaction solver allows the structural and the fluid domains to have dissimilar meshes. This means that direct connectivity is not enforced across the fluid-solid interfaces.

Performing a fluid-structure interaction analysis consists of five main steps:

1.) Build fluid and solid finite element models, and apply boundary conditions.
2.) Flag the fluid-solid interfaces using the ANSYS FSI boundary condition.
3.) Specify fluid-structure interaction analysis options, such as which domain is solved first.
4.) Obtain solution.
5.) Post-process fluid and solid results. This must be done separately. A separate output file is produced for each domain. The fluid results are stored in the (.rfl) file, and the solid results are stored in the (.rst) file.

Figure 4.17 is a block diagram of the solution process. Because the fluid and solid meshes are not connected directly, a search procedure locates nodes on the fluid-solid interface. Nodal values from one domain are then distributed onto the appropriate nodes across the interface. The fluid forces, solid displacements, and solid velocities are transferred across the interface. The algorithm loops through the solid and fluid analyses until convergence is reached for each time step or the user-specified maximum number of stagger iterations is reached. Convergence is based on the quantities transferred across the interface. This process is repeated until convergence is obtained for all time steps. More information about this process can be found in Reference [23].

A Lagrangian mesh discretizes the structural domain and an arbitrary Lagrangian-Eulerian mesh discretizes the fluid domain. The fluid mesh deforms based on the structural domain deformation, or the fluid mesh deformation can be prescribed directly through fluid element displacement degrees of freedom. When the fluid mesh motion is not directly prescribed, an elasticity based morphing system deforms the fluid mesh based on structural displacements and velocities. Note the fluid element displacement degrees of freedom represent the displacements of nodes in the fluid mesh, not necessarily the displacements of the fluid. The fluid velocity degrees of freedom at a given node are not directly affected by specifying displacement degrees of freedom at that node. Implicit finite difference methods provide the temporal descretization.

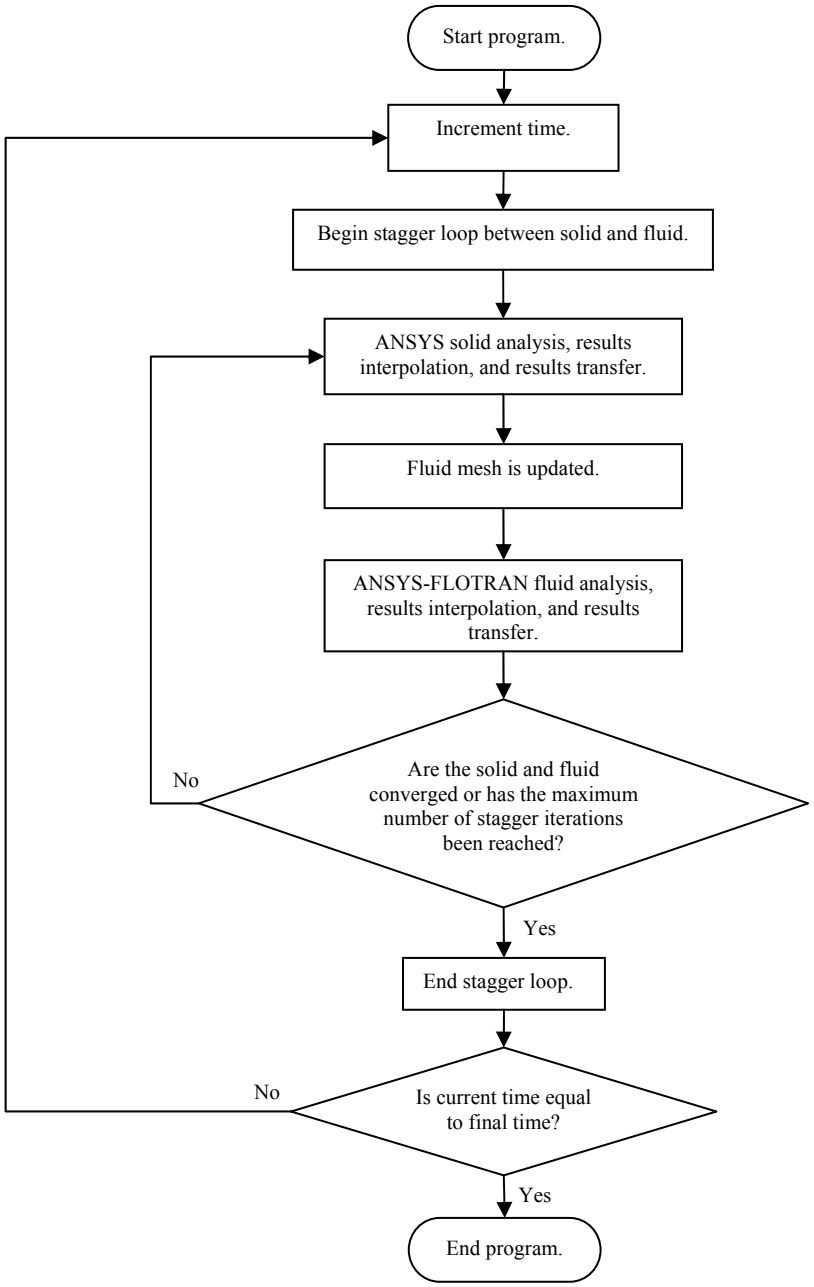

Figure 4.17. Block diagram of ANSYS FSI sequential weak coupling solution process.

4.5.1. Boundary Conditions

The cross sectional geometry shown in Figure 4.10 was used in all analyses in Section 4 unless otherwise stated. Figure 4.18 shows a three dimensional view of the domain used for the computations. The center of the tube resides at the origin of a rectangular Cartesian coordinate system. The cross section lies on planes parallel to the x-y plane and the cross sectional geometry is extruded along the z-axis. In order to take advantage of all available symmetry, only the top right quarter of the cross section was meshed. Normal displacements and velocities were set to zero along the symmetry planes which are formed by cuts made by the planes $x = 0$ and $y = 0$.

The total tube/matrix cell length modeled is 20 millimeters. The top surface is depressed uniformly by a sinusoidal function of time that differs in amplitude and frequency in different analyses. The form of the function is $y = A\cdot(\cos(\omega\cdot t)-1)$ where A is the amplitude and ω is the driving frequency. For the remainder of the discussion, if it is stated that a certain percent strain is applied at a certain frequency, it is to be assumed that this means that the strain is varied from zero to the stated percent strain by a function of the form previously mentioned. If the tube is loaded symmetrically about the plane $z = 0$, the solution will be symmetric about this plane as well. Since the top surface displacement is constant, it is symmetric about the plane $z = 0$. This symmetry condition was used in the finite element analysis, and normal (z-direction) displacements and velocities were set to zero on this plane. Therefore, only 10 millimeters of the length was meshed. The tube/matrix cell is assumed to only be one in a large array of repeated cells. Therefore, the outer face of the tube/matrix cell, which lies parallel to the y-z plane, is also a symmetry plane. The convective velocities of the fluid on the inner surfaces of the tube cavity were taken as zero. This is consistent with no-slip boundary conditions.

The exit end of the tube/matrix cell is located at a z-location of 10 millimeters. At this location a zero pressure boundary condition was applied to the fluid elements, and the z-displacements of both the fluid mesh and the solid mesh were set to zero. Setting the z-displacement degrees of freedom of the fluid mesh to zero does not affect the

velocity degrees of freedom of the fluid; the constraint only restricts the elasticity based mesh morphing system from moving the constrained nodes in the z-direction.

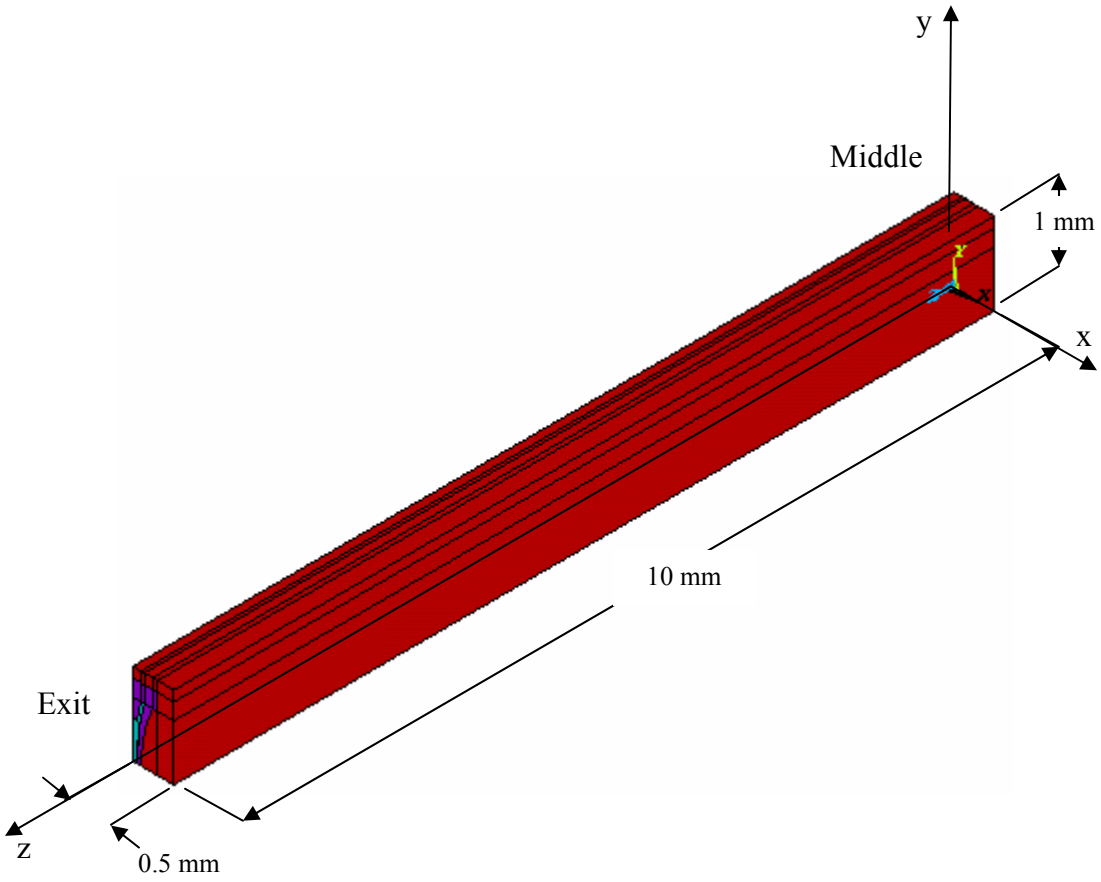

Figure 4.18. Three dimensional domain used for the finite element mesh.

4.5.2. Material Properties and Constitutive Models Used in the Analyses

The material properties used for the transient, three dimensional fluid-structure interaction models were those described in Section 4.2.8 except that the matrix material was modeled as nearly incompressible instead of fully incompressible. The matrix material's Poisson's ratio was set to 0.4995. This value makes the ratio of the bulk

modulus to shear modulus approximately 10^3. A ratio in the range 10^3-10^4 is appropriate for modeling nearly incompressible materials [13]. The density of both the tube and matrix material in the undeformed state was 1100 kg/m^3. The fluid is incompressible and is of the Newtonian type. The fluid density used is 970 kg/m^3 in all analysis and the fluid viscosity was varied. Non-linear geometric effects were included in all models.

4.5.3. Element Selection

Table 4.8 gives details of each element type and number of each type used in the models. The element used to model the tube material was the SOLID45 continuum element. Extra displacement shapes were included to improve bending behavior (KEYOPT(1) = 0) [14]. With these options selected, SOLID45 is an 8-node hexahedral finite element. The element uses an incompatible-modes displacement formulation that is tri-linear in displacements with x-, y-, and z-displacement degrees of freedom carried at each node. A lumped mass matrix helped reduce runtime.

The element used to model the matrix material was the SOLID185 continuum element with pure displacement formulation and uniform reduced integration with hourglass controls (KEYOPT(2) = 1). The mixed u-p formulation was not used since this would introduce a large number of additional unknowns into the three dimensional model. Also, reduced integration lowered runtime because fewer loops were required to integrate the stiffness matrix of these elements. With these options selected, SOLID185 is an 8-node hexahedral finite element that is tri-linear in displacements with x-, y-, and z-displacement degrees of freedom carried at each node. Again, a lumped mass matrix was used to help reduce runtime.

The FLUID142 continuum element was used to model the fluid domain. The flow was assumed to be laminar, since the flows of interest are those where the ratio of inertial forces to viscous forces is small. Displacement degrees of freedom were included (KEYOPT(4) = 1) to accommodate the arbitrary Lagrangian-Eulerian formulation used in the analyses. This is an 8-node hexahedral finite element. It uses a mixed v-p formulation that is tri-linear in displacement and velocity and constant in

pressure. The x-, y-, and z-displacement and velocity degrees of freedom are carried at each node with the constant element pressure carried as a Lagrangian multiplier. These elements use stabilized Galerkin formulations and a consistent mass matrix [14]. Appendix B is an example input file.

Table 4.8. Element descriptions for Section 4.4.

Element Type	Number in Mesh	Mass Matrix	Number of Nodes	Degrees of Freedom	Sketch
SOLID45 KEYOPT(1)=0 Displacement Formulation, Hexahedral, Continuum Element	7268	Lumped	8	Linear x-, y-, and z-Displacements	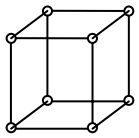
SOLID185 KEYOPT(2)=1 Displacement Formulation, Hexahedral, Continuum Element	12420	Lumped	8	Linear x-, y-, and z-Displacements	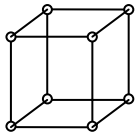
FLUID142 KEYOPT(4)=1 Laminar Flow, Mixed v-p Formulation, Hexahedral, Continuum Element	6912	Consistent	8	Linear x-, y-, and z-Displacements and Velocities	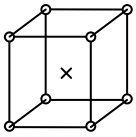
			1 Internal	Element Constant Pressure	

4.5.4. Numerical Results

The numerical results of the transient, three dimensional fluid-structure interaction finite element models are presented in the following sections. A convergence tolerance of 2.5e-5 was used for all quantities in the transient, three dimensional analyses. The maximum number of stagger iterations was set to a sufficiently large number to ensure convergence for each time step. Unless otherwise stated, thirty-six time steps were used for all analyses.

Section 4.5.4.1. Tests of Derived Scaling Rules

In this section transient, three dimensional models are used to test the validity of Equations (4.30)-(4.32) that were developed in Section 4.4 by assuming that inertial forces are negligible. The equations are used as scaling rules, and the effectiveness of the scaling for determining similarity between different systems is assessed.

First, a study was conducted where all variables except driving frequency (ω) and fluid dynamic viscosity (μ) were held constant. The material properties discussed in Section 4.5.2 were used for these analyses. A 0 to -2.5 % sinusoidal through-the-thickness engineering strain was used for the analyses of this section. Referring to Equation (4.30) it is observed that if the mass effects are negligible, the same specific damping capacity should be obtained for any number of systems if the same $\omega \cdot \mu$ is used with all other quantities held constant. To test this, a set of values of $\omega \cdot \mu$ was chosen and the specific damping capacity was calculated for three values of driving frequency, namely 10 Hz, 50 Hz, and 100 Hz.

The definition of specific damping capacity described in Section 4.3 was used in this section. This definition is equivalent to the MAC material's energy dissipation efficiency. The models were executed for one and one half cycles. The transient of the solution appeared to have dissipated after the first half cycle. Therefore, the data for the first half cycle were not used since startup effects were present. Average stress values were calculated by summing reaction forces on the top surface of the tube/matrix cell and dividing the sum by the top surface area. These values were then plotted against engineering strain, and a stress-strain curve with a hysteresis loop was formed for each model. Figures 4.19 and 4.20 are representative of the curves obtained by this procedure. It is seen from Figure 4.19 that the stress does not lag the strain by a constant phase angle. Therefore, there is not a constant tan δ value for the MAC composite lamina. This implies that the mechanical response is not linearly viscoelastic.

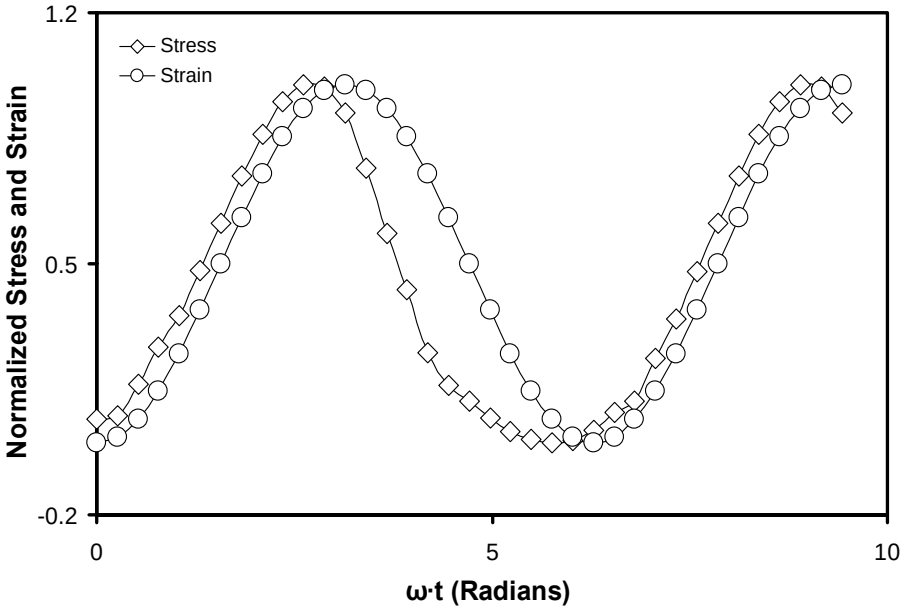

Figure 4.19. Normalized average top surface stress and strain for 45 poise fluid viscosity, and a 0 to -2.5 % sinusoidal engineering strain at a 10 Hz frequency.

Stress-strain curves such as Figure 4.20 were integrated through one cycle, and the energy dissipated through one cycle was found. The specific damping capacity was calculated by numerically integrating the stress-strain curves using the trapezoidal rule and dividing the energy inside the hysteresis loops of each curve by the total energy input by boundary forces in a cycle for each problem.

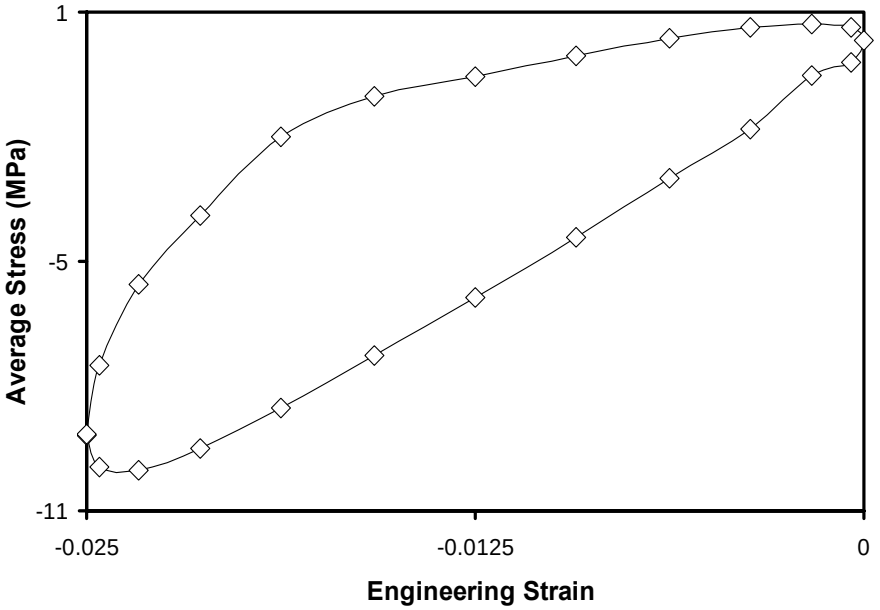

Figure 4.20. Average top surface stress vs. engineering strain for 45 poise fluid viscosity, and a 0 to -2.5 % sinusoidal engineering strain at a 10 Hz frequency.

Figure 4.21 is a plot of the specific damping capacity as a function of $\omega \cdot \mu$ in units of Hertz multiplied by poise. The data is presented in Table 4.9. The three data sets match very closely. Small differences in the solution were expected due to the degree of approximation induced by the sequence of numerical methods used to obtain the approximate solutions. The results agree well and support the proposed scaling rules for the cases considered.

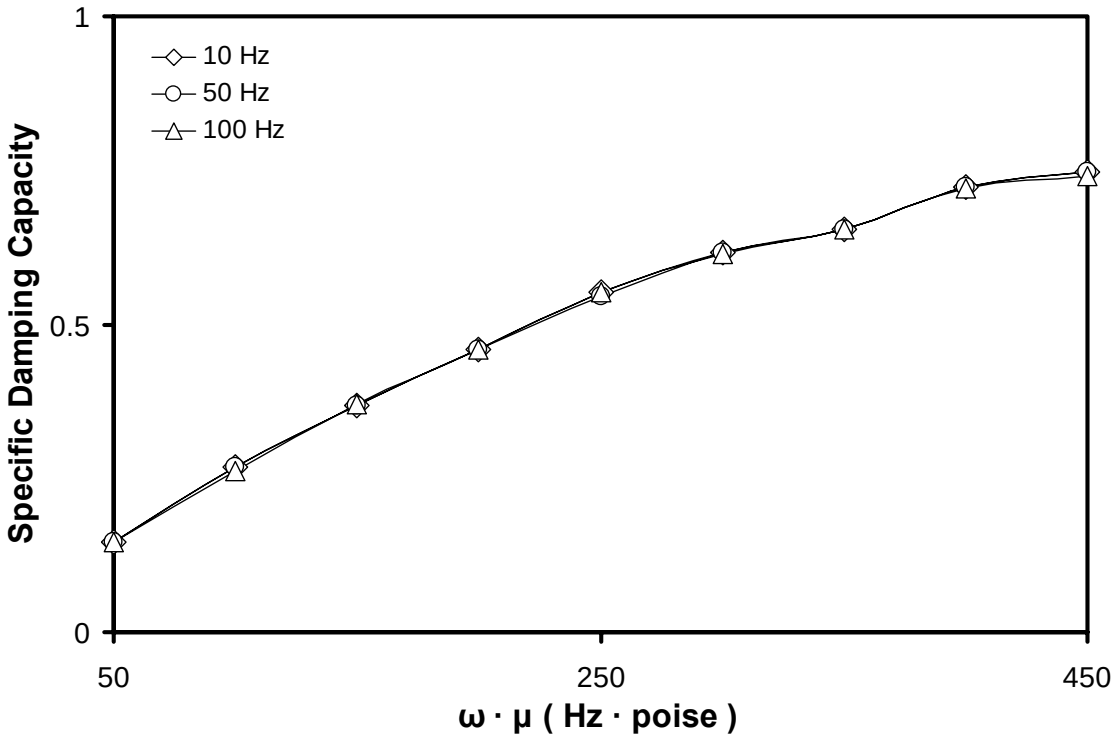

Figure 4.21. Specific damping capacity vs. product of driving frequency and fluid dynamic viscosity.

Table 4.9. Specific damping capacity vs. (ω·μ) at 10, 50, and 100 Hz.

ω·μ (Hz·p)	Specific Damping Capacity 10 Hz	Specific Damping Capacity 50 Hz	Specific Damping Capacity 100 Hz
50	0.147	0.147	0.147
100	0.268	0.268	0.262
150	0.367	0.367	0.370
200	0.459	0.459	0.458
250	0.551	0.546	0.552
300	0.617	0.617	0.614
350	0.654	0.654	0.654
400	0.723	0.723	0.720
450	0.747	0.747	0.741

Second, two analyses are conducted with the same geometry, loading, and $E_i/(\omega \cdot \mu)$ values. According to Equations (4.28) and (4.29), the two analyses should yield the same $P/(\omega \cdot \mu)$ and $V/(L \cdot \omega)$ values as functions of the product of driving frequency and time ($\omega \cdot t$). For simplicity of identification, these two dimensionless parameters are referred to as Dimensionless Parameter A and Dimensionless Parameter B respectively.

The geometry and material densities used are the same as those discussed in Section 4.5.2. The loading is a 0 to -2 % sinusoidal through-the-thickness engineering strain applied at a driving frequency of 50 Hz. Table 4.10 contains the data used for the two analyses. For simplicity of identification, these analyses are referred to as Analysis 1 and Analysis 2.

Table 4.10. Material properties used for Analysis 1 and Analysis 2.

Material Type	**Property Type**	**Analysis 1**	**Analysis 2**
Tube Material	Modulus of Elasticity (MPa)	2000	1500
	Poisson's Ratio	0.35	0.35
Matrix Material	Shear Modulus (MPa)	10	7.5
	Poisson's Ratio	0.4995	0.4995
Fluid	Dynamic Viscosity (poise)	10	7.5

Figures 4.22 and 4.23 are plots of the dimensionless variables obtained from Analysis 1 and Analysis 2 versus $\omega \cdot t$. In Figure 4.22, the value of Dimensionless Parameter A occurs at the center of the tube. As the figure shows, the results in Figure 4.22 match very closely. In Figure 4.23, the value of Dimensionless Parameter B occurs at the location of maximum magnitude of fluid velocity at the tube exit. The results shown in this figure also match very closely.

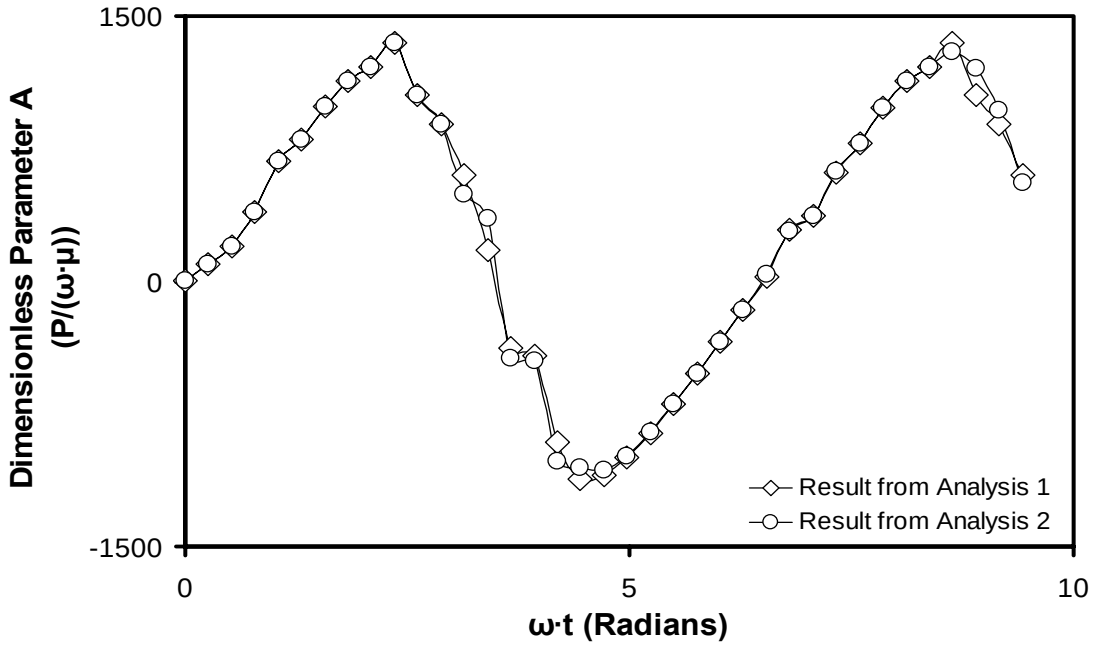

Figure 4.22. Dimensionless Parameter A vs. ω·t.

The results obtained from the fluid pressure do not agree quite as well as the results obtained from the velocity field. This is not surprising since the pressure is only found as a constant on each finite element, while the velocity field is tri-linear on each finite element and constitutes primary degrees of freedom in the finite element analysis. Since the tube length and driving frequency for Analysis 1 and Analysis 2 are the same, the value of V should match for the two analyses. The average velocity values at the tube exit for Analysis 1 and Analysis 2 are 391.45 mm/s and 391.22 mm/s respectively. The percent difference with respect to the average of two values is 0.06 %. This is a very close match. The results of this section support the validity of the scaling rules developed in Section 4.4 for the problems considered.

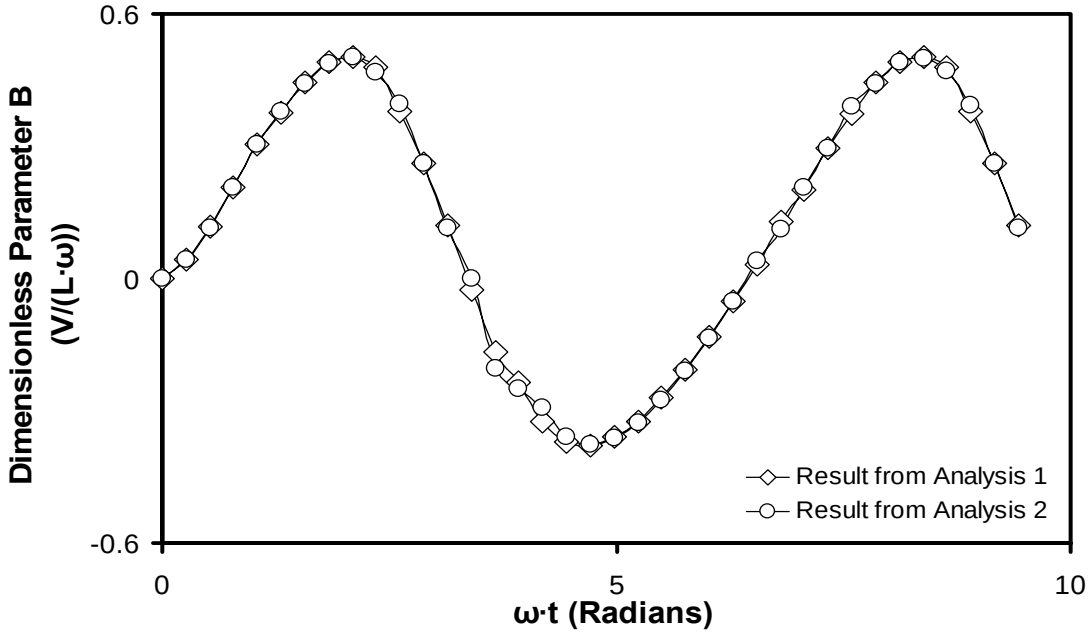

Figure 4.23. Dimensionless Parameter B vs. ω·t.

4.5.4.2. Effect of Changing Loading Amplitude, Driving Frequency, and Fluid Dynamic Viscosity on Specific Damping Capacity (Energy Dissipation Efficiency)

A series of numerical experiments was carried out to determine the effect of changing displacement amplitude, driving frequency, and fluid dynamic viscosity while holding geometry and other material properties constant. The loading was a sinusoidal through-the-thickness engineering strain applied at a driving frequency of 50 Hz. The high strain bound through a cycle was 0 %, and the low bound varied from -0.5 % to -3 % at -0.5 % increments. The product of the driving frequency and fluid dynamic viscosity was varied from 10-1000 (Hz·poise) at 50 (Hz·poise) increments. Based on the results of Section 4.5.4.1, the product of driving frequency and fluid dynamic viscosity was used as an independent variable instead of the two being used separately. The results are plotted in Figure 4.24. The numerical values are presented in Table 4.11.

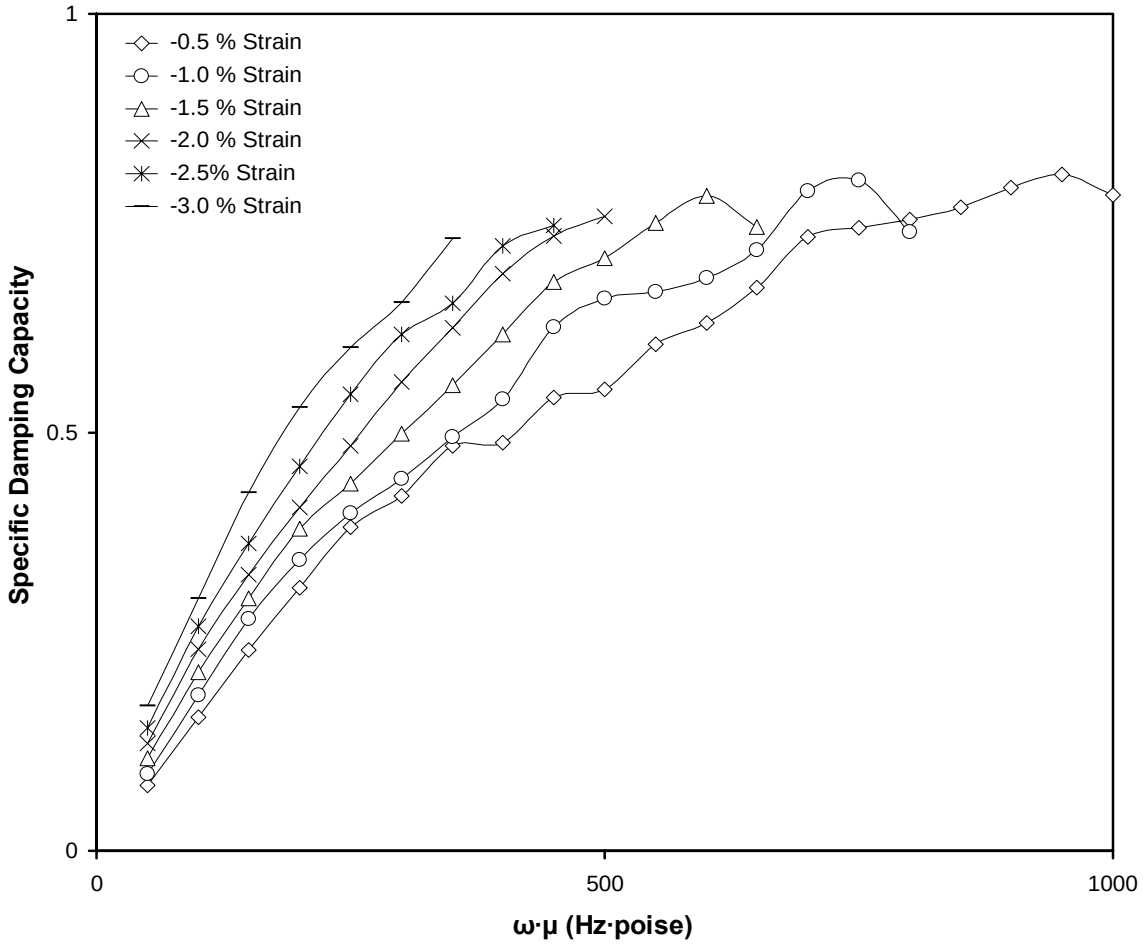

Figure 4.24. Specific damping capacity vs. the product of driving frequency and fluid dynamic viscosity.

Table 4.11. Specific damping capacity data.

	%Strain	-0.5	-1.0	-1.5	-2.0	-2.5	-3.0
ω·μ (Hz·poise)		**Specific Damping Capacity**					
50		0.078	0.092	0.111	0.128	0.147	0.173
100		0.160	0.186	0.214	0.241	0.268	0.302
150		0.240	0.277	0.302	0.330	0.367	0.428
200		0.314	0.348	0.385	0.410	0.459	0.530
250		0.387	0.404	0.439	0.484	0.546	0.601
300		0.424	0.445	0.499	0.560	0.617	0.655
350		0.484	0.495	0.556	0.625	0.654	0.732
400		0.488	0.540	0.617	0.690	0.723	----------
450		0.542	0.626	0.680	0.735	0.747	********
500		0.551	0.660	0.708	0.758	----------	********
550		0.605	0.668	0.750	----------	********	********
600		0.631	0.685	0.783	********	********	********
650		0.673	0.718	0.745	********	********	********
700		0.734	0.788	********	********	********	********
750		0.744	0.801	********	********	********	********
800		0.754	0.739	********	********	********	********
850		0.769	********	********	********	********	********
900		0.792	********	********	********	********	********
950		0.808	********	********	********	********	********
1000		0.784	********	********	********	********	********
* Solution Not Attempted				- No Solution Due to Fluid Element Failure			

The data in Table 4.11, for all but the lowest three strain magnitude values, end abruptly when the inner surfaces of the tube sidewalls near the tube exit make contact with one another. At the same instant the inner surfaces of the tube sidewalls near the middle of the tube length are displaced from their original position by very little. This is due to a pressure gradient. The magnitude of the pressure is highest at the tube center, preventing the tube sidewalls from closing as much as at the tube exit during the compression phase of the loading. Only one quarter of the cross section of the tube/matrix cell was meshed. Therefore, the tube sidewall may pass through the fluid mesh, causing the fluid elements in this area to have zero or negative volume. At this point these fluid elements fail. This is a failure of the numerical methods used to obtain an approximate solution.

Figure 4.25 is a contour plot of the x-displacements of the fluid domain for the last converged solution with a 0 to -3 % sinusoidal engineering strain. The data are taken at

the time of maximum fluid pressure during compression. The fluid dynamic viscosity was 7 poise. The view in this figure is looking from the exit of the tube toward the tube center. From the figure it is observed that the passage is significantly wider at the tube center than at the tube exit although the sidewall is displaced inwardly at both locations. The maximum magnitude of x-displacement at the middle of the tube length is 0.014 millimeters, while the value at the exit of the tube is 0.042 millimeters. These values occur at the inner surface halfway up the sidewalls of the physical tube. When the tube is undeformed, the x-distance from the centerline of the tube to both locations is 0.05 millimeters. The percent closure at the middle of the tube length and at the exit of the tube are 27.98% and 84.80% respectively. Therefore, the closure at the tube exit is 3.03 times as large as the value at the middle of the tube length. This result shows the three dimensional nature of the problem considered. Also, at this time there is only a 0.008 millimeter x-distance between the centerline of the tube and the sidewall at the tube exit. This means that the elements in this area are very compressed. When a solution was attempted with an 8 poise dynamic viscosity, the gap completely closed and the tube sidewall passed through the fluid mesh, causing element failure.

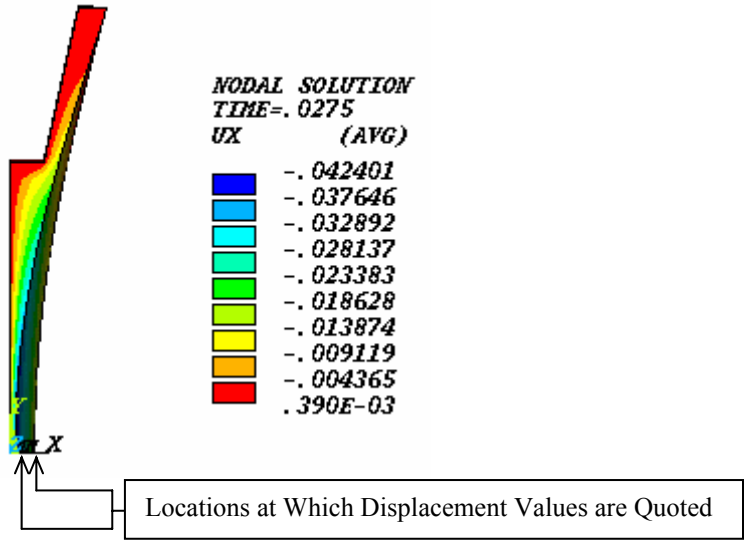

Figure 4.25. Contour plot of x-displacements for 7 poise fluid and a 0 to -3 % sinusoidal engineering strain applied at a driving frequency of 50 Hz.

An interesting observation from Figure 4.24 is that the rate of change of specific damping capacity with respect to ω·μ approaches zero as ω·μ is increased. Since the specific damping capacity is unknown past the cutoff value for situations with higher strain magnitudes, it cannot be concluded that the observed cutoff value is a maximum value, but it does have physical significance. The cutoff is due to sidewall contact.

For the models with maximum strain magnitudes less than 2 %, the specific damping capacity actually attains a maximum value and then begins to decrease. The problem of interior sidewall contact is not present for the lower strain magnitudes. For the models with -0.5, -1.0, and -1.5% lower strain bounds, one data point past the observed maximum for each strain value was obtained. After this solutions were not attempted. From examining the data in Table 4.11, it is observed that the cutoff values seen for higher cyclic strain magnitudes are in a similar range as the maxima observed for lower cyclic strain magnitudes. However, the highest specific damping capacity value obtained (0.808), occurs for a 0 to -0.5 % sinusoidal engineering strain.

It is reasonable that the specific damping capacity is bounded. In order to maintain conservation of energy the maximum value that the specific damping capacity may attain is one. For the geometry under consideration it is advantageous to operate at lower strain magnitudes because sidewall contact is not observed, the induced stresses are lower than those induced for larger strain magnitudes, and high specific damping capacity values are obtained for small strain values.

4.5.4.3. Study of Relationship of Matrix Material Stiffness to Damping Properties

A study is performed to determine the effect of changing matrix stiffness on specific damping capacity of a machine augmented composite lamina. The problems studied use a 0 to -2 % sinusoidal engineering strain applied at a driving frequency of 50 Hz, a 5 poise fluid dynamic viscosity, and the geometry and mesh described in Sections 4.5.1-4.5.3. The material properties discussed in Section 4.5.2 are also used, except that the shear modulus of the matrix material is varied. The data are presented in Table 4.12.

Figure 4.26 shows the values of specific damping capacity obtained from the analysis versus matrix material shear modulus.

Table 4.12. Effect of matrix material shear modulus on damping properties.

Matrix Material Shear Modulus (MPa)	**Specific Damping Capacity**
7.5	0.546
8.0	0.536
8.5	0.509
9.0	0.500
9.5	0.491
10.0	0.484

In this range of shear modulus, Table 4.12 and Figure 4.26 indicate that the specific damping capacity decreases slightly with increasing shear modulus. It is important to note that it is desirable for a material to not only possess good damping properties, but to also possess high stiffness. Although smaller matrix stiffness produces a slightly higher specific damping capacity in this range, the decrease in matrix stiffness also causes a decrease in composite stiffness. The latter is a negative consequence. Also, if a stiffer matrix is used, a slightly more viscous fluid may also be used to compensate for the increased stiffness. In contrast, a negative consequence of continuing to increase the matrix stiffness is that, as is shown in Section 3.2.4 for cases without fluid, the stresses in both the tube material and the matrix material will increase with increasing matrix material stiffness. A situation with high stiffness, high damping characteristics, and low induced stress is the most desirable. Determining the optimum combination of material properties is a complex task and depends on the loading and the type of response required from the MAC composite material for a given application.

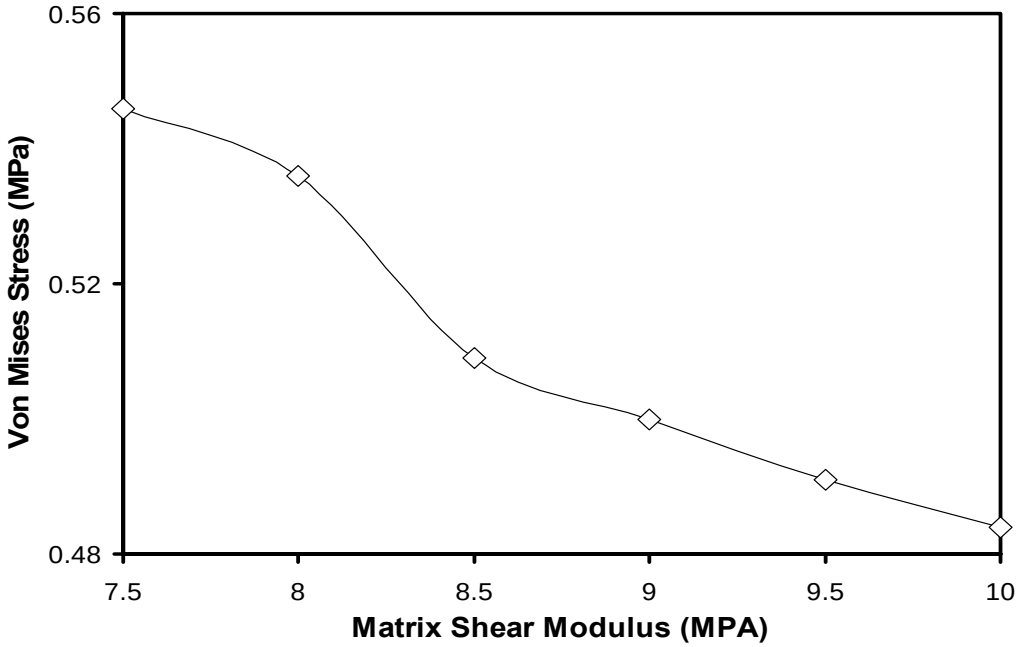

Figure 4.26. Specific damping capacity vs. matrix material shear modulus.

4.5.4.4. Comparison of Results Obtained from Simplified Model and Transient, Three Dimensional Models

Numerical analyses were performed to compare the results for the pressure field obtained from transient, three dimensional models and those obtained from the simplified model developed in Section 4.2. The first set of numerical tests was for a tube length of 20 mm with a 0 to -3 % engineering strain applied at a driving frequency of 50 Hz. The geometry and material properties used for the analyses of Section 4.5.4.2 were also used for all analyses of this section. Two values of fluid dynamic viscosities were used. Figures 4.27 and 4.28 are plots of the average fluid pressure versus time through one steady-state cycle with fluid dynamic viscosity of 1 poise and 7 poise respectively.

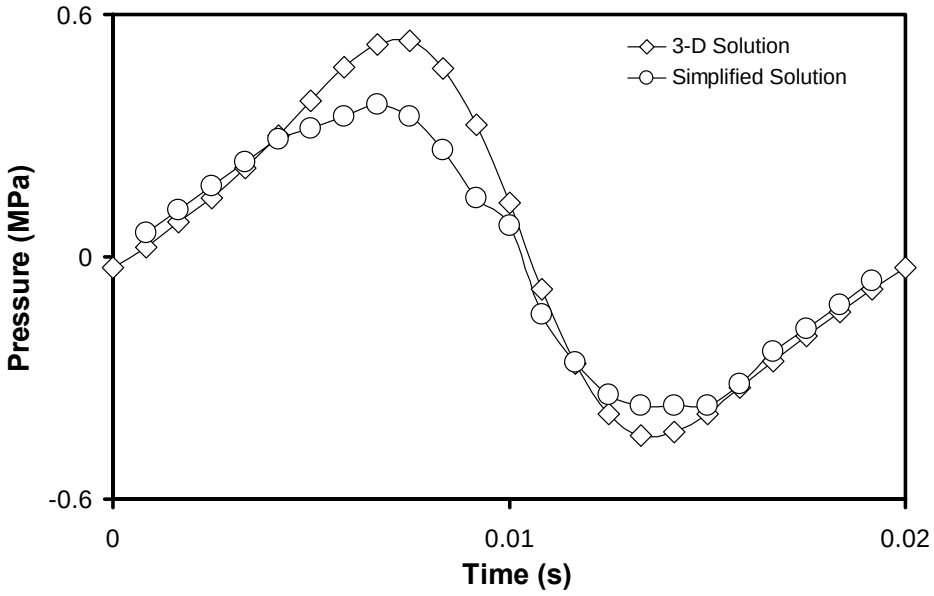

Figure 4.27. Average tube pressure through one steady-state cycle for a tube length of 20 mm, 0 to -3 % sinusoidal engineering strain at a driving frequency of 50 Hz, and 1 poise fluid dynamic viscosity.

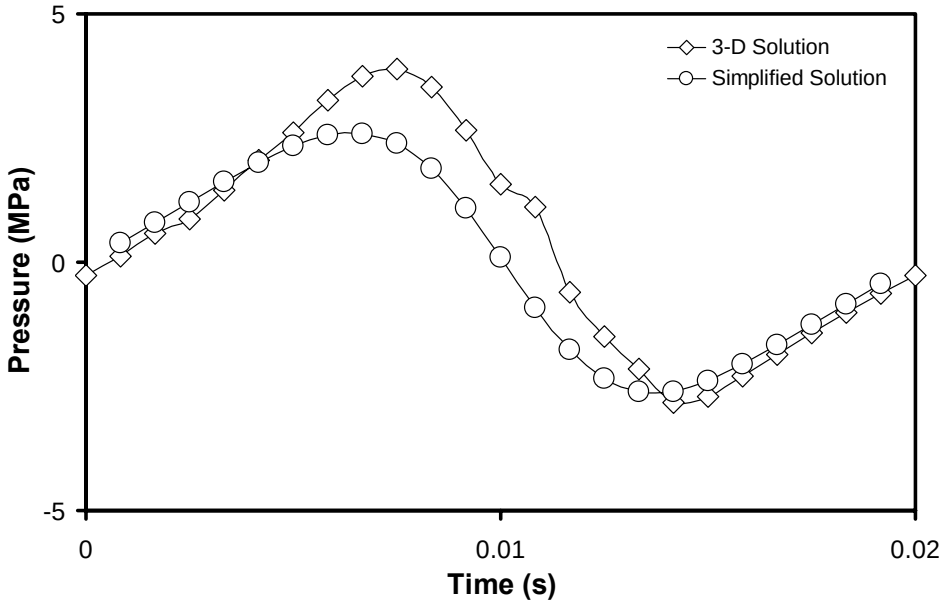

Figure 4.28. Average tube pressure through one steady-state cycle for a tube length of 20 mm, 0 to -3 % sinusoidal engineering strain at a driving frequency of 50 Hz, and 7 poise fluid dynamic viscosity.

The plots show that the simplified solution predicts the general shape of the pressure curve as a function of time, but the peak pressures are drastically underestimated. There are several possible reasons for the large discrepancy. The most likely source is error introduced into the simplified solution by the assumption that the dimensionless parameter K doesn't change significantly during the deformation. The parameter is shape dependent. For example, if the tube cross section begins as a square and remains a square, regardless of actual dimensions, the K parameter does not change. This is not the type of deformation experienced by the tube geometry used in the analyses. The shape of the tube does change significantly when a large through-the-thickness strain is applied to a tube/matrix cell.

The K parameter increases as the fluid passage narrows. This means that using the value for an undeformed tube is an underestimate in cases that involve large strains. This is consistent with the underestimation of pressure shown in Figures 4.27 and 4.28. Therefore, the assumption of constant K in cases of large applied strain is invalid.

There is closer agreement between the results in the case with a lower fluid dynamic viscosity. This is because lower pressure is produced when a lower viscosity fluid is used as the working fluid. In contrast, when higher viscosity fluids are used, a higher pressure and pressure gradient along the length of the tube are produced. The higher pressure gradient causes the deformation of the tube to be less uniform along the length of the tube. This phenomenon is discussed in Section 4.5.4.2. Figure 4.25 shows an example of this situation.

The second set of numerical tests was for a tube length of 20 mm with a 0 to -1 % sinusoidal engineering strain at a driving frequency of 50 Hz. Two values of fluid dynamic viscosities were used. Figures 4.29 and 4.30 are plots of the average tube pressure versus time through one cycle with a fluid dynamic viscosity of 1 poise and 10 poise respectively.

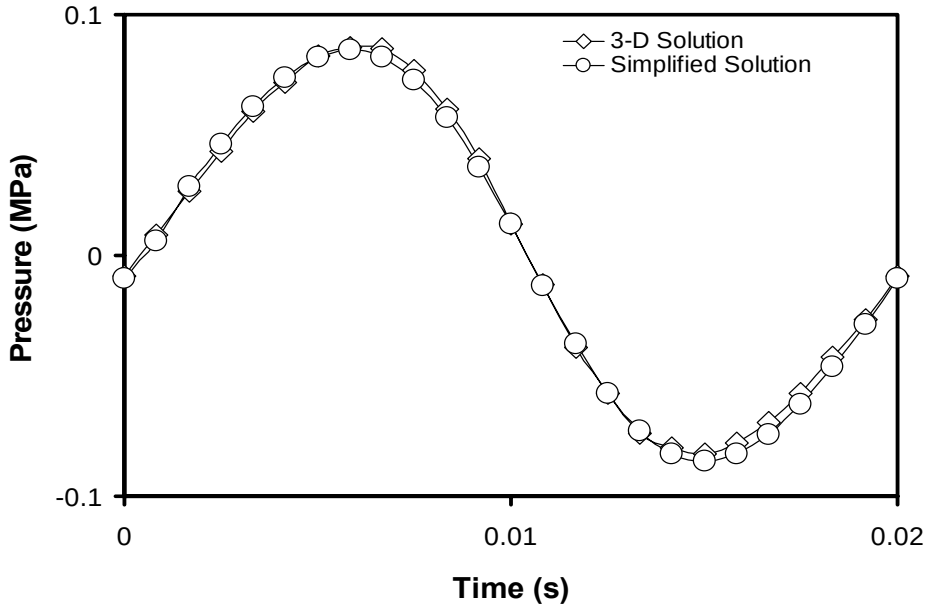

Figure 4.29. Average tube pressure through one steady-state cycle for a tube length of 20 mm, 0 to -1 % sinusoidal engineering strain at a driving frequency of 50 Hz, and 1 poise fluid dynamic viscosity.

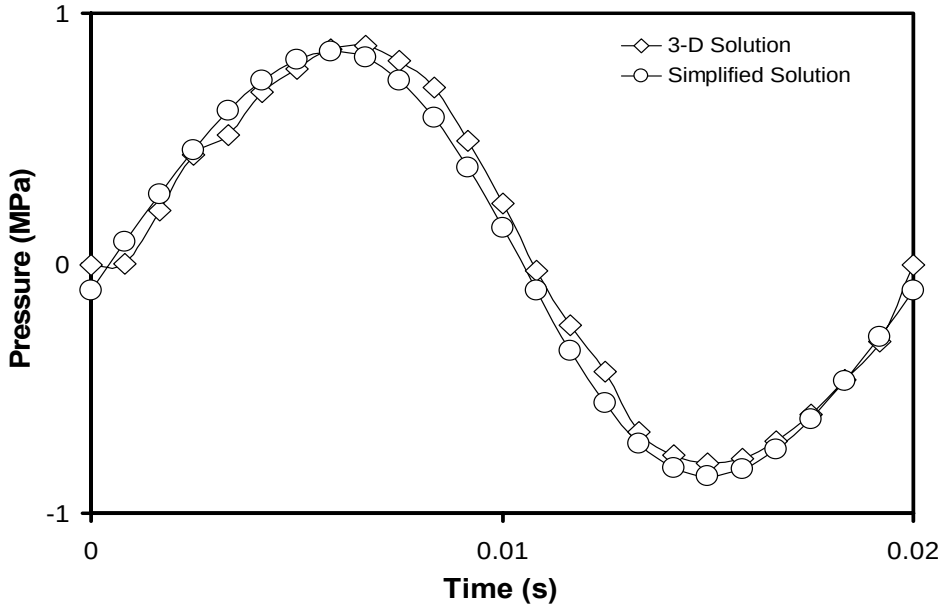

Figure 4.30. Average tube pressure through one steady-state cycle for a tube length of 20 mm, 0 to -1 % sinusoidal engineering strain at a driving frequency of 50 Hz, and 10 poise fluid dynamic viscosity.

The results for this value of strain agree much more closely than those obtained for the larger strain. This is consistent with the assumption that the major source of error in the simplified solution is that associated with not updating the value of the K parameter. This is because the K parameter is shape dependent, and the change in shape associated with a -1 % engineering strain is much smaller than that associated with a -3 % engineering strain.

The results for the lower viscosity fluid match more closely than the results for the higher viscosity fluid. This is due to the increasingly three dimensional nature of the problem as the pressure generated increases.

Figures 4.31 is a plot of the extreme values of pressure through one cycle versus time for a 1 poise fluid dynamic viscosity. Figures 4.32 is a plot of the extreme values of pressure through one cycle versus time for a 10 poise fluid dynamic viscosity. These pressure values occur at the middle of the tube.

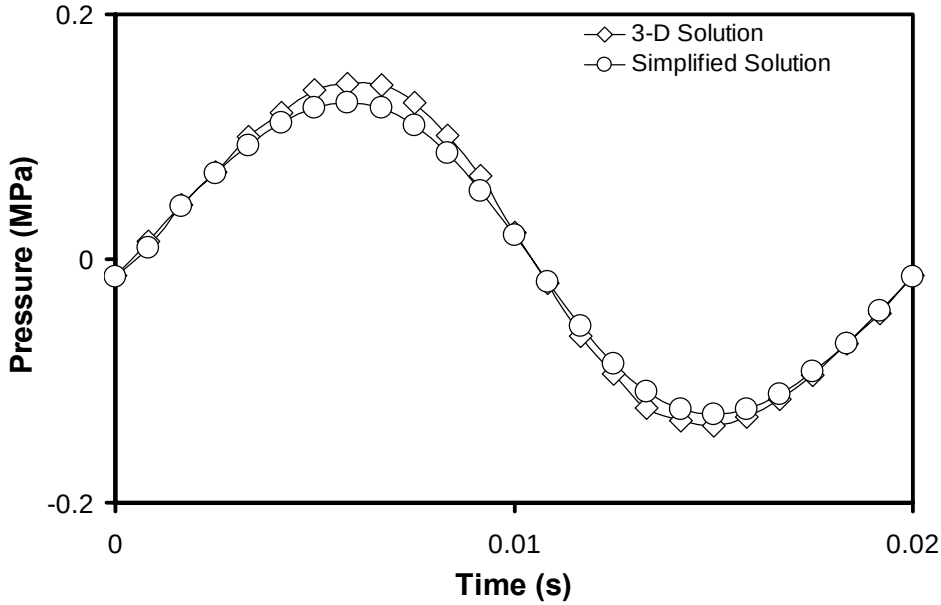

Figure 4.31. Pressure extremes through one steady-state cycle for a tube length of 20 mm, 0 to -1 % sinusoidal engineering strain at a driving frequency of 50 Hz , and 1 poise fluid dynamic viscosity.

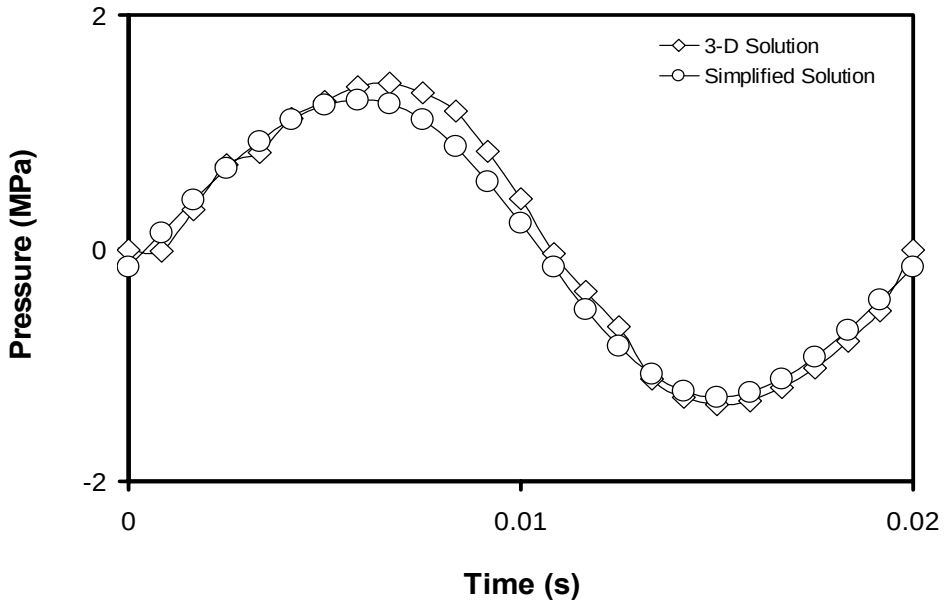

Figure 4.32. Pressure extremes through one steady-state cycle for a tube length of 20 mm, 0 to -1 % sinusoidal engineering strain at a driving frequency of 50 Hz, and 10 poise fluid dynamic viscosity.

The observations made about the results for the average pressure apply to the results for the extreme pressure that occurs at the middle of the tube. The only difference is that the results for the average pressure are in slightly closer agreement than the results for the extreme pressure.

Table 4.13 contains the minimum and maximum values obtained from the analyses discussed in this section. As can be seen, the differences between the results can be quite high even at low strain magnitudes.

Table 4.13. Pressure values from comparison study of simplified and 3-D models.

Engineering Strain		-1 %		-3 %	
Fluid Dynamic Viscosity		1 poise	10 poise	1 poise	7 poise
Average Pressure from Simplified Model (MPa)	**Minimum**	-8.52E-02	-8.52E-01	-3.68E-01	-2.62E+00
	Maximum	8.52E-02	8.48E-01	3.79E-01	2.59E+00
Average Pressure from 3-D Model (MPa)	**Minimum**	-8.26E-02	-8.02E-01	-4.43E-01	-2.83E+00
	Maximum	8.65E-02	8.68E-01	5.35E-01	3.89E+00
Pressure Extremes from Simplified Model (MPa)	**Minimum**	-1.28E-01	-1.28E+00	----------	----------
	Maximum	1.28E-01	1.27E+00	----------	----------
Pressure Extremes from 3-D Model (MPa)	**Minimum**	-1.37E-01	-1.34E+00	----------	----------
	Maximum	1.43E-01	1.42E+00	----------	----------

Table 4.14 contains the percent differences of the results obtained from the simplified solution method as compared to those obtained from the transient, three dimensional models. Most of the percent difference values are high. If the results from the transient, three dimensional models are assumed to be closer to the correct solution, the usefulness of the simplified model, with all of the assumptions made, is brought into question.

Table 4.14. Percent differences with respect to 3-D solution for model comparison.

Engineering Strain		-1 %		-3 %	
Fluid Dynamic Viscosity		1 poise	10 poise	1 poise	7 poise
% Difference for Average Pressure	**Minimum**	3.15	6.23	16.93	7.42
	Maximum	1.50	2.30	29.16	33.42
% Difference for Extreme Pressure Values	**Minimum**	6.57	4.48	----------	----------
	Maximum	10.49	10.56	----------	----------

As is discussed in Section 4.2, the simplified model predicts a linear z-direction velocity distribution and a quadratic pressure distribution along the length of the tube. It also predicts that if the z-component of the fluid velocity is zero at the center of the tube, then this velocity attains its maximum magnitude at the tube exit. In addition, the simplified model predicts that the fluid pressure attains its maximum magnitude at the middle of the tube.

A set of results was taken from transient, three dimensional models with a 0 to -2 % sinusoidal engineering strain with a driving frequency of 50 Hz and a 10 poise fluid

dynamic viscosity. The results were analyzed to determine their agreement with the predicted characteristics.

The first data set comes from the time of maximum fluid velocity and fluid pressure. This occurs near halfway through the compression phase of the applied sinusoidal displacements. Figures 4.33 and 4.34 are plots of the maximum z-component of the fluid velocity and centerline fluid pressure, respectively. A linear regression was performed on the data in Figure 4.33, and a quadratic regression was performed on the data in Figure 4.34. The regressions are plotted as solid lines along with there respective data. The R^2 correlation values obtained for the data of Figures 4.33 and 4.34 are 0.9962 and 0.9997 respectively.

It is observed that the maximum velocity magnitude occurs at the tube exit, and the maximum fluid pressure magnitude occurs at the middle of the tube. For this instant in time, these specific predictions made by the simplified model are supported by the results of the transient, three dimensional models.

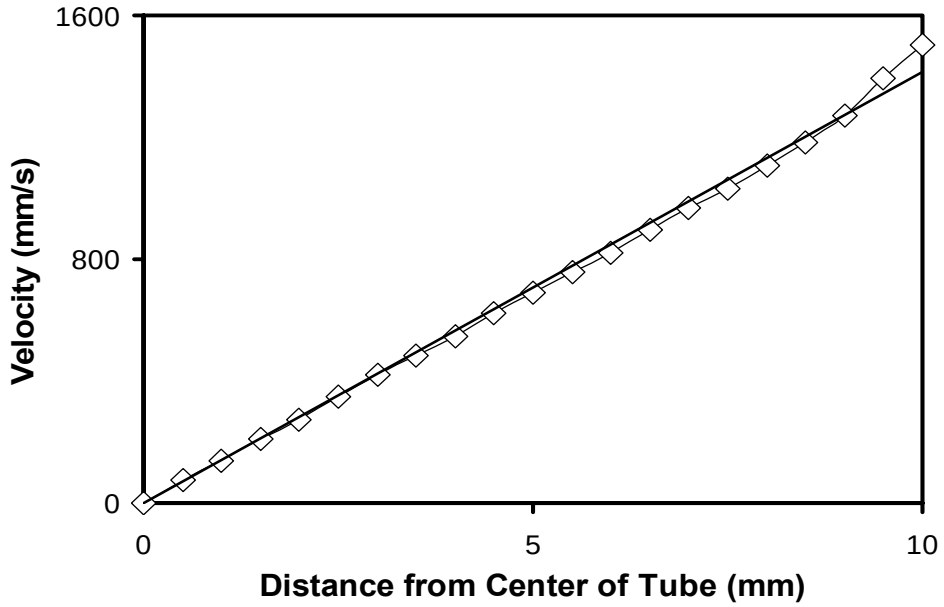

Figure 4.33. Maximum z-velocity vs. distance from middle of tube half through the compression phase of the sinusoidal applied displacements.

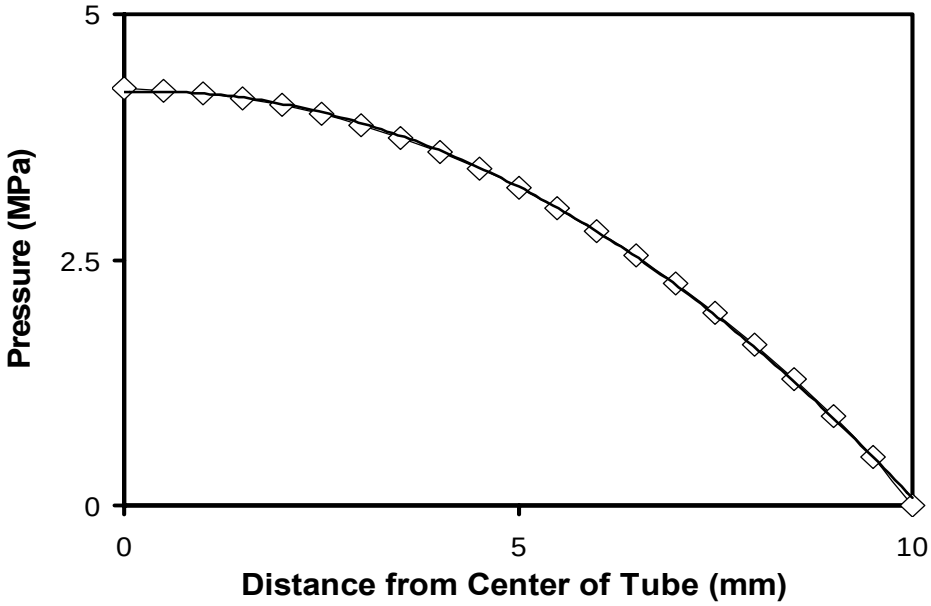

Figure 4.34. Centerline fluid pressure vs. distance from middle of tube half through the compression phase of the sinusoidal applied displacements.

A second data set was taken at the time step just past full compression, when the fluid flow was in the process of changing from flowing out of the tube to flowing into the tube. Figures 4.35 and 4.36 are plots of the maximum z-component of fluid velocity and centerline fluid pressure respectively. A linear regression was performed on the data presented in Figure 4.35, and the regression is also plotted. The R^2 correlation value for the linear regression is 0.7736. A quadratic regression was performed on the data presented in Figure 4.36, and the regression is also plotted. The R^2 correlation value for the quadratic regression is 0.9984.

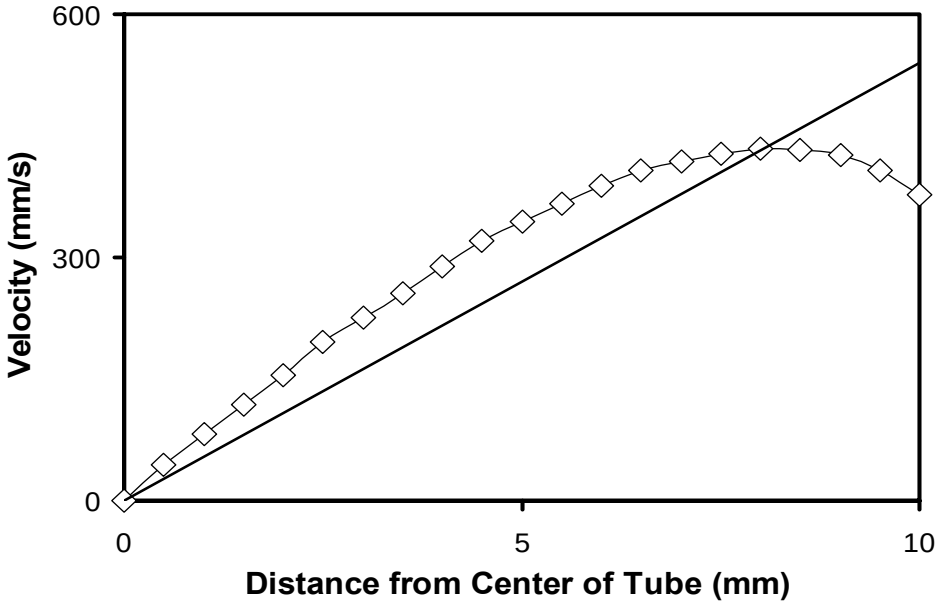

Figure 4.35. Maximum z-velocity vs. distance from middle of tube at time just past full compression.

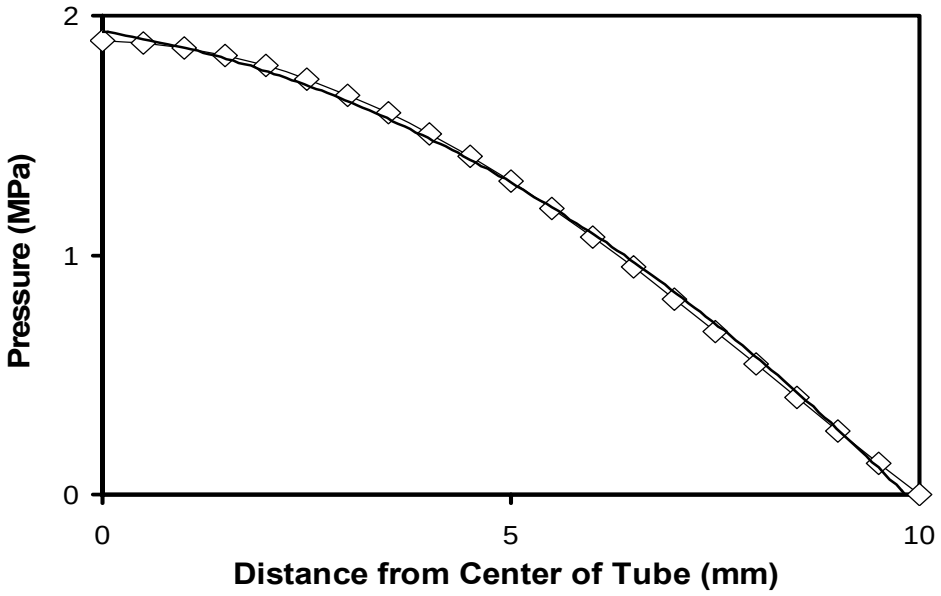

Figure 4.36. Centerline fluid pressure vs. distance from middle of tube at time just past full compression.

For this instant in time, the predictions of the simplified model concerning the general shape of the pressure distribution and location of maximum pressure magnitude agree well with the results of the transient, three dimensional model. However, the simplified model predicts that the maximum magnitude of the z-component of the fluid velocity always occurs at the tube exit, except when the fluid flow changes direction. It predicts that when the flow changes direction the velocity is zero everywhere. Neither of the aforementioned predictions about the velocity field is supported by the results of the transient, three dimensional models. Therefore, the predictions made by the simplified model do not seem to be valid for this instant in time. It is believed that the reason for this discrepancy is non-uniformity of the tube deformation along its length. Perhaps the uniform deformation assumption is too constraining to the structure and needs to be relaxed. The drawback to doing this is that the structural problem then becomes three dimensional and requires a much longer solution time.

4.5.4.5. Study of Effect of Changing Tube Geometry on Damping Performance

Two analyses were performed and their respective results compared. The models have identical material properties and loading. However, the tube cross sectional geometry differs between the two models. In each model the tube is centered in a matrix cell with the dimensions shown in Figure 4.10. The material properties discussed in Section 4.5.2 were used for both analyses in this section. The fluid dynamic viscosity used for both analyses in this section was 2 poise. The loading was a 0 to -2.5 % sinusoidal engineering strain applied at a driving frequency of 50 Hz. The tube half-length used for these analyses was 10 millimeters.

The first model discussed uses the tube geometry shown in Figure 3.4. For this geometry the undeformed tube cavity hydraulic diameter is 0.2631 millimeters. The specific damping capacity value obtain from the analysis was 0.065. Figure 4.37 is a contour plot of the maximum z-component of the fluid velocity at the tube exit that occurs in a cycle of loading. Figure 4.38 is a contour plot of the maximum fluid pressure that occurs in a cycle of loading. The view for Figure 4.38 is looking at the side of the

tube. The tube exit is to the right and the tube middle is at the left. From figures 4.37 and 4.38, the maximum z-component of the fluid velocity and the maximum fluid pressure occurring in a cycle are 995.9 mm/s and 0.2422 MPa respectively. Also note from Figure 4.37 that the maximum fluid velocity on the cross section occurs at the point farthest away from the tube sidewall. Figure 4.38 shows that the pressure variation on a given cross section of the tube is not large as compared to the pressure variation along the length.

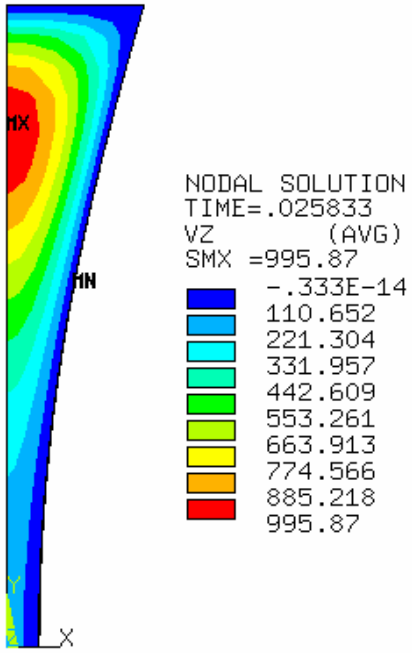

Figure 4.37. Maximum z-component of fluid velocity (mm/s) in a cycle for tube geometry of Figure 3.4.

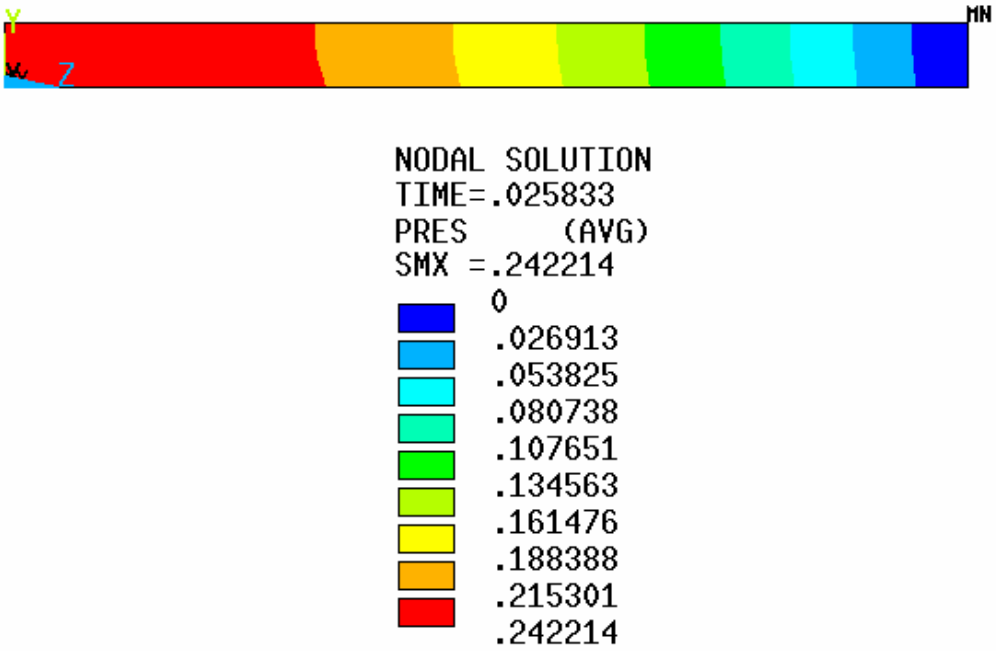

Figure 4.38. Maximum fluid pressure (MPa) in a cycle of loading for tube geometry of Figure 3.4.

The second model discussed is one of the models from Section 4.5.4.2. For this geometry the undeformed tube cavity hydraulic diameter is 0.1489 millimeters. The specific damping capacity value obtain from this analysis was 0.268. Figure 4.39 is a contour plot of the maximum z-component of the fluid velocity at the tube exit that occurs in a cycle of loading. Figure 4.40 is a contour plot of the maximum fluid pressure that occurs in a cycle of loading. The view for Figure 4.40 is looking at the side of the tube. The tube exit is to the right and the tube middle is at the left. The figures show that the maximum z-component of the fluid velocity and the maximum fluid pressure occurring in a cycle are 1993 mm/s and 1.194 MPa respectively.

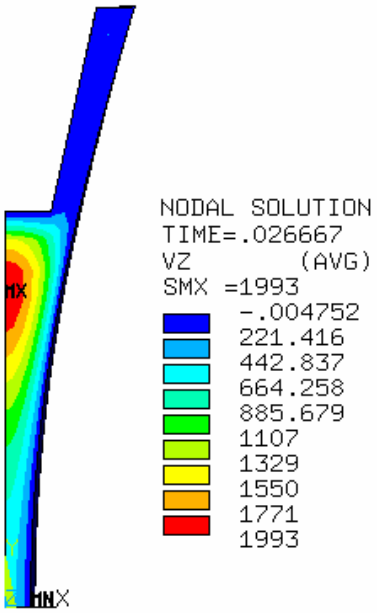

Figure 4.39. Maximum z-component of fluid velocity (mm/s) in a cycle for tube geometry of Figure 4.10.

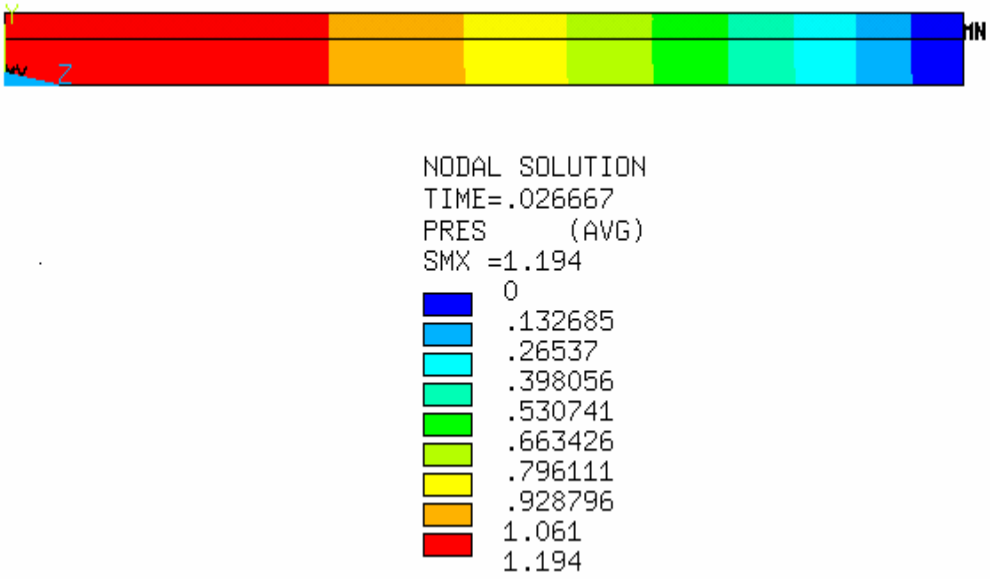

Figure 4.40. Maximum fluid pressure (MPa) in a cycle of loading for tube geometry of Figure 4.10.

A 43.41% decrease in hydraulic diameter resulted in a 312.3% increase in the specific damping capacity. The maximum z-component of the fluid velocity increased by 100.1%. The maximum fluid pressure increased by 393.1%. The results demonstrate that the damping performance of a tube/matrix cell, and thus a machine augmented composite material, is highly dependent on the geometry of the tube cavity. It is also clear that the addition of the extra material shown in Figure 4.9 causes a large improvement in damping performance. It should be noted that in this comparison the reduction of the hydraulic diameter was done by adding tube material in such a way as not to significantly increase the through-the-thickness stiffness of the tube/matrix cell. If the hydraulic diameter is reduced but the stiffness is increased, the damping performance of the tube/matrix cell may not improve. This is because the specific damping capacity is improved by increased energy dissipation but is harmed by the addition of stiffness. Also, the addition was chosen so the material resides in the location where the maximum fluid velocity occurs without the addition. This causes a redistribution of the fluid flow into a smaller passage. This is seen by comparing Figures 4.37 and 4.39. Again the fluid pressure appears to be very close to constant on a given cross section.

5. SUMMARY AND CONCLUSIONS

Various numerical and dimensional analysis techniques were employed to gain insight into the geometry, the material property combinations, and the boundary conditions that are effective in producing high damping machine augmented composite (MAC) materials. The results of Section 3.1.4 demonstrate that lower stress values are produced during through-the-thickness compression for the tube cross sectional geometry of Figure 3.4 than for the originally proposed geometry shown in Figure 3.1.

The results of Section 3.2.4 demonstrate that higher stress values are induced during through-the-thickness compression when a tube is in a matrix cell for the matrix properties studied. The induced stress values are lower for less stiff matrix material.

The results of Section 4.1.6 imply that inserting completely filled and sealed tubes into a matrix material is not a good method for developing an effective damping MAC material, at least for the tube designs studied. Increasing the fluid dynamic viscosity does influence the first resonant frequency of these models, but the influence is small. In addition, no damping is detectable at low frequencies.

Dimensionless parameters and reduced differential equations governing fluid flow in a long, narrow tube containing viscous, incompressible fluid are developed and presented in Section 4.2. The development assumes zero pressure end conditions. A simplified model that assumes the tube deformation is uniform along the tube length is also presented.

In Section 4.2.9, the simplified model shows an approximately linear increase in fluid pressure with an increase in fluid dynamic viscosity in the range studied. Also, the simplified model shows an approximately quadratic increase in fluid pressure with increase in tube half-length in the length range studied.

Further dimensional analysis is presented in Section 4.4. It is proposed that, for effective damping MAC materials, inertial effects of the solid and fluid are negligible as compared to elastic and viscous forces. Dimensional analysis is carried out with fluid and solid densities removed from the variable list. With this assumption, it is shown that

an important dimensionless parameter is the ratio of solid material elastic moduli to the product of fluid dynamic viscosity and driving frequency ($E_i/(\omega \cdot \mu)$). Numerical tests carried out in Section 4.5.4.1 demonstrate the effectiveness of the dimensional analysis of Section 4.4 as a scaling rule for the problems considered.

The results of Section 4.5.4.2 show that increasing strain magnitude, with all other variables held constant, can result in an increase in the specific damping capacity of a MAC material lamina. In addition, increasing the product of fluid dynamic viscosity and driving frequency ($\omega \cdot \mu$), with all other variables held constant, can favorably affect the specific damping capacity of a MAC material lamina. In some cases a local maximum is reached.

The maximum specific damping capacity value obtained from any analysis of Section 4.5.4.2 is 0.808. This seems to be a maximum value of the geometry and solid moduli used in the study of that section. The value is quite high when considering that a value of one corresponds to a material which is completely viscous. The results are encouraging and indicate that effective damping material may be produced via machine augmentation if the appropriate combination of materials and boundary conditions is chosen. Further study is necessary to determine if higher values may be obtained by changing tube geometry. Also, the effects of changing tube length have not been addressed by 3-D models. The matrix volume fraction is another variable that may significantly influence the performance of a MAC material. Also, since high specific damping capacity values were obtained with small strain amplitudes, it may be possible to use stiffer solid constituents in conjunction with a more viscous fluid in order to obtain equivalent damping performance along with higher stiffness. It is reasonable to assume that improvements are possible.

It should be pointed out that the solid materials in all models in this study are treated as hyperelastic materials. Therefore, no viscoelastic properties that the solid material may possess are taken into account. Many elastomers have viscoelastic properties. For example, a polyurethane elastomer with the same shear modulus at room temperature as that used in Section 4.5.4.2 has a tan δ value in the range of 0.15-0.20 at room

temperature [18]. The driving frequency at which this was measured was not provided. According to Equation (4.22), this range of tan δ corresponds to a specific damping capacity range of 0.38-0.46 if the loading oscillates about zero. If a matrix material with dissipative properties similar to those discussed above is used, it is reasonable to assume that values predicted using hyperelastic constitutive models may be underestimates of the performance of the actual physical system. However, the physical system cannot have a specific damping capacity greater than one, and due to the nonlinearity of the problem and the fact that an energy ratio is the quantity of interest, superposition may not be applied.

The results of Section 4.5.4.3 show that specific damping capacity is a function of matrix material stiffness. The specific damping capacity decreases with increasing matrix stiffness while all other variables are held constant.

The results of Section 4.5.4.4 show that in some cases the results obtained from the simplified model do not agree well with results obtained from transient, three dimensional models. The results match most closely in cases where the fluid dynamic viscosity is small and the compressive strain magnitude is small as well. In these cases, the damping is small. It is believed that the discrepancies have two major sources. The first is the fact a geometry dependent parameter K was not updated during the analysis. The undeformed value was used during the entire computation.

The second is the assumption that the tube deformation does not vary along its length. This assumption makes the computation much faster and easier because the three dimensional problem is then reduced to a two dimensional problem. However, the assumption also over constrains the structural deformation. As is mentioned in Section 4.5.4.2, the results of a transient, three dimensional models show that in some cases the tube deformation at the tube exit is very different than the deformation at the middle of the tube. Therefore, the simplified model with all the assumptions is not especially useful and may lead to false conclusions when pressure values are large. It seems to perform more poorly around the time that the fluid flow changes direction.

In fairness to the simplified model, the comparisons of Section 4.5.4.4 use models that are not especially long. This is because of a node limit in the ANSYS university release. In the development of the simplified equations in Section 4.2.1, it was assumed that the ratio of the hydraulic diameter of the tube cavity to the length dimension of the tube is very small. In Section 4.5.4.4 the ratio of the undeformed hydraulic diameter to tube half-length is 0.015. It was also assumed in Section 4.2.1 that the inverse of the length was much smaller than the hydraulic diameter. However, in Section 4.5.4.4 these two values are of the same order of magnitude. This fact may contribute to the differences in the solutions produced by the two methods.

Another approach that may yield better results than the simplified model with all assumptions, is to solve a three dimensional structural problem and use Equation (4.17) to calculate the pressure gradient at a number of points along the tube length. Then, the pressure gradient may be numerically integrated in order to calculate the pressure distribution. Equation (4.15) may be used to obtain the velocity gradients and shear stresses. An iterative procedure may then be used to find equilibrium between the solid and fluid. For this method, a three dimensional structural problem is solved and the pressure gradient is found at chosen points along the length of the tube by solving a two dimensional problem at each of these locations. Further study is needed to determine the effectiveness of this method. It should be noted that this method may not be much, if any, more attractive than solving a three dimensional structural problem and solving the three dimensional Stokes Equations.

The results of Section 4.5.4.5 show that the response of a MAC material is very sensitive to the tube cavity geometry. The smaller hydraulic diameter produces better results. The sensitivity may prove to be an undesirable effect due to uncertainties in manufacturing.

Future study is needed to understand the effects of placing MAC lamina into hybrid composites. Recall the initial through-the-thickness stiffness shown in Figure 3.18 (259.6 MPa) and the maximum specific damping capacity found in Section 4.5.4.2 (0.808). A MAC material with the aforementioned stiffness and damping properties is

more dissipative than it is stiff. However, if the dissipative MAC material lamina is used in low volume fraction with a stiff lamina phase, it is believed that the resulting composite will retain much of the through-the-thickness stiffness of the stiff phase and much of the dissipative properties of the MAC lamina [4, 5]. Future studies are needed to test these predictions.

Another possibility for future study is the use of non-Newtonian fluids. The rate of change of fluid cavity volume is not constant through a cycle. Shear thinning or thickening fluids may interact with the rate of structural deformation in such a way as to dissipate more energy through a cycle than a Newtonian fluid.

REFERENCES

1. Hawkins G. F. Augmenting the mechanical properties of materials by embedding simple machines. *Journal of Advanced Materials* 2002; **34**:16-20.
2. Christensen R. M. *Theory of Viscoelasticity* (2nd edn). Academic Press, Inc.: New York, 1982.
3. Lee G. F., Hartman B. Specific damping capacity for arbitrary loss angle. *Journal of Sound and Vibration* 1998; **211**:265-272.
4. Chen C. P., Lakes R. S. Analysis of high loss viscoelastic composites. *Journal of Materials Science* 1993; **28**:4299-4304.
5. Brodt M., Lakes R. S. Composite materials which exhibit high stiffness and high viscoelastic damping. *Journal of Composite Materials* 1995; **29:**1823-1833.
6. Lakes R. S. Viscoelasticity, accessed 2004, http://silver.neep.wisc.edu/~lakes/VE.html.
7. Felippa C., Park K. C., Farhat C. Partitioned analysis of coupled mechanical systems. *Comput. Methods Appl. Mech. Engr.* 2001; **190**:3247-3270.
8. Deparis S., Fernandez M. A., Formaggia L., Nobile F. Modified fixed point algorithm in fluid-structure interaction. *C. R. Mecanique* 2003; **331**:525-530.
9. Kuhl E., Hulshoff S., de Borst R. An arbitrary Lagrangian Eulerian finite-element approach for fluid-structure interaction phenomena. *Int. J. Numer. Meth. Eng.* 2003; **57**:117-142.
10. Heil M. Stokes flow in collapsible tubes: computation and experiment. *J. Fluid Mech.* 1997; **353:**285-312.
11. Xu Z., Accorsi M. Finite element mesh update methods for fluid-structure interaction simulations. *Finite Elements in Analysis and Design* 2004; **40**:1259-1269.
12. Belytschko T., Liu K. W., Moran B. *Nonlinear Finite Elements for Continua and Structures*. Wiley: New York, 2000.
13. Bonet J., Wood R. D. *Nonlinear Continuum Mechanics for Finite Element Analysis*. Cambridge University Press: New York, 1997.

14. *ANSYS Element Reference*, ANSYS Release 6.1, April 2002. (Available at website <http://www.ansys.com>)
15. Boenig H. V. *Structure and Properties of Polymers*. John Wiley & Sons: New York, 1973.
16. Ogden R. W. Large deformation elasticity-on the correlation of theory and experiment for incompressible rubberlike solids. *Proceedings of the Royal Society of London*. *Series A, Mathematical and Physical Sciences.* 1972; **326**:565-584.
17. Matweb Material Property Data, Properties of Nylon 6/6, accessed 2004, http://www.matweb.com.
18. BSAF Mechanical Properties Data Sheet, Properties of Elastomers, accessed 2004, http://www.basf.com/businesses/polymers/urethanes/pdfs/tpu/mechanprop.pdf.
19. *ANSYS Theory Reference*, ANSYS Release 6.1, April 2002. (Available at website <http://www.ansys.com>)
20. *ANSYS Structural Analysis Guide*, ANSYS Release 6.1, April 2002. (May be purchased at website <http://www.ansys.com>)
21. Munson B. R., Young D. F., Okiishi T. H. *Fundamentals of Fluid Mechanics.* Wiley: New York, 1998.
22. Hibbit, Karlsson, & Sorensen, Inc. *ABAQUS/Standard User's Manual, Version 6.2* (vol. 5). Hibbit, Karlsson, & Sorensen, Inc.: Pawtuckett, RI, 2001.
23. *ANSYS Coupled-Field Analysis Guide*, ANSYS Release 6.1, April 2002. (Available at website <http://www.ansys.com>)

APPENDIX A

```
C    SUB_FLUID.F
C-----------------------------------------------------------------------------------------------------------------------
C    CONK=(K) PARAMETER FOR UNDEFORMED TUBE CAVITY SHAPE
C    LENGTH=TUBE LENGTH
C    VINITIAL=UNDEFORMED CAVITY VOLUME
C    DYNAMVIS=DYNAMIC VISCOSITY OF FLUID
C    PHO=DENSITY OF FLUID
C    PREF=INITIAL PRESSURE
C    PINCI=INITIAL PRESSURE INCREMENT
C    TOLER=CONVERGENCE TOLERANCE
C    INCR=NUMBER OF LOAD OR TIME INCREMENTS
C-----------------------------------------------------------------------------------------------------------------------
C
C
C    SUBROUTINE TO IMPLEMENT FLUID CAVITY EQUATION
C
C
      SUBROUTINE DISP(U,KSTEP,KINC,TIME,NODE,NOEL,JDOF,COORDS)
C
      INCLUDE 'ABA_PARAM.INC'
C
      PARAMETER (CONK=167.0,LENGTH=20.0,HYDDIAM=0.1468,VINITIAL=0.299238E+01)
           PARAMETER (DYNAMVIS=1.0e-7,PHO=0.97E-9)
      PARAMETER (PREF=-0..0
      PARAMETER (PINCI=0.0010,TOLER=1.0e-4,INCR=24)
C
       DIMENSION U(3),TIME(2),COORDS(3),DSPCRV(INCR+1,2)
C
           COMMON/KPRESS/DT,ACTT,DV,VOLD,VNEW,DIFP,DELTPO,DELTPN,PNEW,POLD,PI
           NC,PAPP,TOL,
           1DISPLACE,CONX,REH,,VELMAX,IQUIT,ICALL1,ICALL2,ICOUNT,IFIRST,ICOUNT1,IP
           OINTS
C
      TOL=TOLER
C
      CONX=CONK*DYNAMVIS*LENGTH**3/12
C
      IPOINTS=INCR+1
C
C******************SET INITIAL CONDITIONS FOR INCREMENT 0 AND 1*************
C
      OPEN (UNIT=150,STATUS='OLD',FILE= '/tmp/dmm1346/dispcrv1.txt')
C
      REWIND 150
C
      DO I=1,IPOINTS
C
           READ (150,*) (DSPCRV(I,J), J=1,2)
C
```

```
      END DO
C
C*****************************PRESSURE CONTROL SECTION************************
C
      IF (JDOF.EQ.8) THEN
C
          IF (KINC.EQ.0.OR.KINC.EQ.1) THEN
C
              PAPP=PREF
C
              PINC=PINCI
C
              ACTT=DSPCRV(1,1)
C
              TO=ACTT
C
              TN=TO
C
              VOLD=VINITIAL
C
              VNEW=VOLD
C
              DELTPO=0.0
C
              DELTPN=DELTPO
C
              DV=0.0
C
              IFIRST=0
C
              ICOUNT=1
C
              ICOUNT1=ICOUNT+1
C
              IQUIT=0
C
          ELSE
C
              ICOUNT1=ICOUNT+1
C
              IF (ICALL2.EQ.0) THEN
C
                  DT=DSPCRV(ICOUNT1,1)-DSPCRV(ICOUNT,1)
C
                  PNEW=-CONX*(DV/DT)/(VNEW)**2
C
                  DIFP=PNEW-POLD
C
                  DELTPO=DELTPN
C
                  DELTPN=ABS(DIFP)
C
                  VELMAX=-(DV/DT)/VNEW*LENGTH/2
```

```
C
                REH=PHO*abs(VELMAX)*HYDDIAM/DYNAMVIS
C
                IF (KINC.EQ.2) THEN
C
                    OPEN(UNIT=15,FILE='/tmp/dmm1346/good.dat')
C
                                        WRITE(15,*) 'INC  Pressure  ChangeP  Volume  ChangeV
                                Max-Velocity  Max-Reynolds#  Mises  Time'
C
                    OPEN(UNIT=18,FILE='/tmp/dmm1346/presscrv.txt')
C
                    WRITE(18,*) PREF,',',ACTT,','
C
                END IF
C
                IF (IFIRST.EQ.0) THEN
C
                        IF (DIFP.GE.0) PINC=PINCI
C
                        IF (DIFP.LT.0) PINC=-PINCI
C
                        PAPP=PAPP+PINC
C
                        IFIRST=1
C
                    ELSE
C
                        DEDP=(DELTPN-DELTPO)/PINC
C
                        PINC=-DELTPN/DEDP
C
                        PAPP=PAPP+PINC
C
                                    IF (PINC.LE.TOL) THEN
C
                    IF (ICOUNT.EQ.INCR) THEN
C
                        IQUIT=1
C
                    OPEN (UNIT=125,FILE='/tmp/dmm1346/dispcrv.txt')
C
                        DO I=1,IPOINTS
C
                        WRITE(125,*) DSPCRV(I,2),',',DSPCRV(I,1),','
C
                        END DO
C
                    ELSE
C
                        IQUIT=0
C
```

```
                    END IF
C
C
                    ACTT=ACTT+DT
C
                    ICOUNT=ICOUNT+1
C
                    IFIRST=0
C
      WRITE(15,81)KINC-1,PAPP,DIFP,VNEW,DV,VELMAX,REH,CURRMAX,ACTT
C
81    FORMAT(I4,2X,E12.4,2X,E12.4,2X,E12.6,2X,E12.4,2X,E12.4,2X,E12.4,2X,E12.4,2X,E12.4)
C
                    WRITE(18,*) PAPP,',',ACTT,','
C
                END IF
C
                        END IF
C
            END IF
C
            ICALL2=1
C
        END IF
C
        U(1)=PAPP
C
    END IF
C
    IF (JDOF.EQ.2) THEN
C
        IF (KINC.EQ.0) THEN
C
            DISPLACE=DSPCRV(1,2)
C
        ELSE IF (KINC.EQ.1) THEN
C
            DISPLACE=DSPCRV(2,2)
        ELSE
C
            ICOUNT1=ICOUNT+1
C
            IF (ICALL1.EQ.0) THEN
C
                IF (ICOUNT.EQ.IPOINTS) THEN
C
                    DISPLACE=DSPCRV(ICOUNT,2)
C
                ELSE
C
                    DISPLACE=DSPCRV(ICOUNT1,2)
C
```

```
                    END IF
C
                    ICALL1=1
C
                END IF
C
            END IF
C
            U(1)=DISPLACE
C
        END IF
C
        RETURN
C
        END
C
C*****************SUBROUTINE URDFIL TO READ THE RESULTS FILE(.FIL)*************
C
        SUBROUTINE URDFIL(LSTOP,LOVRWRT,KSTEP,KINC,DTIME,TIME)
C
        INCLUDE 'ABA_PARAM.INC'
C
        DIMENSION ARRAY(513),JRRAY(NPRECD,513),TIME(2)
C
        EQUIVALENCE(ARRAY(1),JRRAY(1,1))
C
            COMMON/KPRESS/DT,ACTT,DV,VOLD,VNEW,DIFP,DELTPO,DELTPN,PNEW,POLD,
            PINC,PAPP,TOL,
          1 DISPLACE,CONX,REH,CURRMAX,VELMAX,IQUIT,ICALL1,ICALL2,ICOUNT,IFIRST,
            ICOUNT1,IPOINTS
C
C       EQUIVALENCE OLD VALUES OF VARIABLES WITH THE LAST UPDATED VALUES
C
        CURRMAX=0.0
C
        LSTOP=IQUIT
C
        LOVRWRT=1
C
        ICALL1=0
C
        ICALL2=0
C
        TO=TN
C
        TN=TIME(2)
C
        IF (DELTPN.LE.TOL) VOLD=VNEW
C
        POLD=PAPP
C
        CALL POSFIL(KSTEP,KINC,ARRAY,JRCD)
C
```

```
      DO K1=1,999999
C
           CALL DBFILE(0,ARRAY,JRCD)
C
           IF (JRCD.NE.0) GO TO 100
C
           KEY=JRRAY(1,2)
C
C***************RECORD 137 CONTAINS CURRENT CAVITY VOLUME******************
C
           IF (KEY.EQ.137)  VNEW=ARRAY(4)
C
      END DO
C
100 CONTINUE
C
      DV=VNEW-VOLD
C
      RETURN
      END
```

APPENDIX B

```
/BATCH
/FILNAME,new1p1v50hz,1
/NOPR
/PMETH,OFF,0
KEYW,PR_SET,1
KEYW,PR_STRUC,1
KEYW,PR_THERM,0
KEYW,PR_FLUID,0
KEYW,PR_ELMAG,0
KEYW,MAGNOD,0
KEYW,MAGEDG,0
KEYW,MAGHFE,0
KEYW,MAGELC,0
KEYW,PR_MULTI,1
KEYW,PR_CFD,1
/GO
/PREP7
ET,1,FLUID142
KEYOPT,1,1,0
KEYOPT,1,3,0
KEYOPT,1,4,1
ET,2,SOLID45
KEYOPT,2,1,0
KEYOPT,2,2,0
KEYOPT,2,4,0
KEYOPT,2,5,0_
KEYOPT,2,6,0
ET,3,SOLID185
KEYOPT,3,2,1
KEYOPT,3,4,0
KEYOPT,3,6,0
KEYOPT,3,10,0
K,1,.3,0,0,
K,2,0.5,0,0,
K,2,0.05,0,0,
K,2,0.5,0,0,
K,3,0.05,0,0,
K,4,0.1,0,0,
K,5,0.0,0.675,0,
K,6,0.1418947,0.675,0,
K,7,0.2418947,0.675,0,
K,7,0.2418947,0.675,0,
K,8,0.3,0.675,0,
K,9,0.5,0.675,0,
K,10,0.1,0.675,0,
FLST,3,6,3,ORDE,2
FITEM,3,5
FITEM,3,-10
KGEN,2,P51X, , , ,.2, , ,0
```

```
FLST,3,6,3,ORDE,2
FITEM,3,11
FITEM,3,-16
KGEN,2,P51X, , , ,0.125, , ,0
FLST,3,2,3,ORDE,2
FITEM,3,6
FITEM,3,-7
KSYMM,Y,P51X, , , ,0,0
LARC,       6,      23,       3
LARC,       7,      24,       4
LSTR,       3,       4
FLST,2,2,4,ORDE,2
FITEM,2,1
FITEM,2,-2
LSBL,P51X,       3
FLST,2,2,4,ORDE,2
FITEM,2,5
FITEM,2,7
LDELE,P51X, , ,1
LSTR,       5,      10
LSTR,      10,       6
LSTR,       6,       7
LSTR,       7,       8
LSTR,      13,       7
LSTR,      13,      14
LSTR,      14,       8
LSTR,      13,      12
LSTR,      12,      16
LSTR,      16,      11
LSTR,      11,       5
LSTR,      16,      10
LSTR,      12,       6
LSTR,       3,       4
LSTR,       4,       1
LSTR,       8,       1
LSTR,       1,       2
LSTR,       8,       9
LSTR,       9,       2
LSTR,      14,      15
LSTR,      15,       9
LSTR,      11,      17
LSTR,      16,      22
LSTR,      12,      18
LSTR,      13,      19
LSTR,      14,      20
LSTR,      15,      21
LSTR,      17,      22
LSTR,      22,      18
LSTR,      18,      19
LSTR,      19,      20
LSTR,      20,      21
FLST,3,1,4,ORDE,1
FITEM,3,4
```

```
LGEN,2,P51X, , ,-1, , , ,0
FLST,3,1,3,ORDE,1
FITEM,3,5
KGEN,2,P51X, , ,-1, , , ,0
FLST,3,1,3,ORDE,1
FITEM,3,25
KGEN,2,P51X, , , ,-.675, , ,0
LSTR,      25,      24
LSTR,      25,      26
LSTR,      26,      23
K,27,0,0.45,0,
K,28,0.05,0.45,0,
LSTR,       5,      27
LSTR,      27,      28
LSTR,      28,      10
FLST,2,4,4
FITEM,2,37
FITEM,2,38
FITEM,2,35
FITEM,2,36
AL,P51X
FLST,2,4,4
FITEM,2,39
FITEM,2,40
FITEM,2,41
FITEM,2,1
AL,P51X
FLST,3,1,5,ORDE,1
FITEM,3,2
AGEN,2,P51X, , ,-1, , , ,0
ASBA,       1,       3
FLST,2,4,4
FITEM,2,13
FITEM,2,1
FITEM,2,14
FITEM,2,12
AL,P51X
FLST,2,4,4
FITEM,2,24
FITEM,2,12
FITEM,2,25
FITEM,2,30
AL,P51X
FLST,2,4,4
FITEM,2,2
FITEM,2,15
FITEM,2,11
FITEM,2,14
AL,P51X
FLST,2,4,4
FITEM,2,25
FITEM,2,26
FITEM,2,11
```

```
FITEM,2,31
AL,P51X
FLST,2,4,4
FITEM,2,15
FITEM,2,3
FITEM,2,7
FITEM,2,10
AL,P51X
FLST,2,4,4
FITEM,2,26
FITEM,2,10
FITEM,2,27
FITEM,2,32
AL,P51X
FLST,2,4,4
FITEM,2,27
FITEM,2,8
FITEM,2,28
FITEM,2,33
AL,P51X
FLST,2,4,4
FITEM,2,7
FITEM,2,5
FITEM,2,9
FITEM,2,8
AL,P51X
FLST,2,4,4
FITEM,2,9
FITEM,2,20
FITEM,2,23
FITEM,2,22
AL,P51X
FLST,2,4,4
FITEM,2,28
FITEM,2,22
FITEM,2,29
FITEM,2,34
AL,P51X
FLST,2,4,4
FITEM,2,18
FITEM,2,19
FITEM,2,21
FITEM,2,20
AL,P51X
FLST,2,4,4
FITEM,2,6
FITEM,2,17
FITEM,2,18
FITEM,2,5
AL,P51X
FLST,2,4,4
FITEM,2,4
FITEM,2,16
```

```
FITEM,2,6
FITEM,2,3
AL,P51X
FLST,3,1,4,ORDE,1
FITEM,3,43
LGEN,2,P51X, , ,.05, , , ,0
ASBL,      4,     36
FLST,2,16,5,ORDE,4
FITEM,2,1
FITEM,2,-3
FITEM,2,5
FITEM,2,-17
VEXT,P51X, , ,0,0,10,,,,
FLST,2,2,6,ORDE,2
FITEM,2,15
FITEM,2,-16
VGLUE,P51X
FLST,2,14,6,ORDE,2
FITEM,2,1
FITEM,2,-14
VGLUE,P51X
FLST,2,1,5,ORDE,1
FITEM,2,77
SFA,P51X, ,FSIN,1,
FLST,2,1,5,ORDE,1
FITEM,2,71
SFA,P51X, ,FSIN,2,
FLST,2,1,5,ORDE,1
FITEM,2,70
SFA,P51X, ,FSIN,3,
FLST,2,2,5,ORDE,2
FITEM,2,69
FITEM,2,76
SFA,P51X, ,FSIN,4,
FLST,5,1,5,ORDE,1
FITEM,5,74
CM,_Y,AREA
ASEL,R, , ,P51X
CM,_Y1,AREA
CMSEL,S,_Y
CMDELE,_Y
DA,_Y1,UX,0,1
CMDELE,_Y1
FLST,5,1,5,ORDE,1
FITEM,5,75
CM,_Y,AREA
ASEL,R, , ,P51X
CM,_Y1,AREA
CMSEL,S,_Y
CMDELE,_Y
DA,_Y1,UY,0,1
CMDELE,_Y1
FLST,5,4,5,ORDE,4
```

```
FITEM,5,16
FITEM,5,-17
FITEM,5,68
FITEM,5,73
CM,_Y,AREA
ASEL,R, , ,P51X
CM,_Y1,AREA
CMSEL,S,_Y
CMDELE,_Y
DA,_Y1,UZ,0,1
CMDELE,_Y1
FLST,5,1,5,ORDE,1
FITEM,5,74
CM,_Y,AREA
ASEL,R, , ,P51X
CM,_Y1,AREA
CMSEL,S,_Y
CMDELE,_Y
DA,_Y1,VX,0,1
CMDELE,_Y1
FLST,5,1,5,ORDE,1
FITEM,5,75
CM,_Y,AREA
ASEL,R, , ,P51X
CM,_Y1,AREA
CMSEL,S,_Y
CMDELE,_Y
DA,_Y1,VY,0,1
CMDELE,_Y1
FLST,5,5,5,ORDE,4
FITEM,5,69
FITEM,5,-71
FITEM,5,76
FITEM,5,-77
CM,_Y,AREA
ASEL,R, , ,P51X
CM,_Y1,AREA
CMSEL,S,_Y
CMDELE,_Y
DA,_Y1,VX,0,1
DA,_Y1,VY,0,1
DA,_Y1,VZ,0,1
DA,_Y1,ENKE,-1,1
CMDELE,_Y1
FLST,5,2,5,ORDE,2
FITEM,5,16
FITEM,5,-17
CM,_Y,AREA
ASEL,R, , ,P51X
CM,_Y1,AREA
CMSEL,S,_Y
CMDELE,_Y
DA,_Y1,VZ,0,1
```

```
CMDELE,_Y1
FLST,5,2,5,ORDE,2
FITEM,5,68
FITEM,5,73
CM,_Y,AREA
ASEL,R, , ,P51X
CM,_Y1,AREA
CMSEL,S,_Y
CMDELE,_Y
DA,_Y1,PRES,0,1
CMDELE,_Y1
FLDATA12,PROP,DENS,0
FLDATA13,VARY,DENS,0
FLDATA12,PROP,VISC,0
FLDATA13,VARY,VISC,0
FLDATA12,PROP,COND,0
FLDATA13,VARY,COND,0
FLDATA12,PROP,SPHT,0
FLDATA13,VARY,SPHT,0
FLDATA7,PROT,DENS,CONSTANT
FLDATA8,NOMI,DENS,0.97e-9,
FLDATA9,COF1,DENS,0
FLDATA10,COF2,DENS,0
FLDATA11,COF3,DENS,0
FLDATA7,PROT,VISC,CONSTANT
FLDATA8,NOMI,VISC,1.0e-7,
FLDATA9,COF1,VISC,0
FLDATA10,COF2,VISC,0
FLDATA11,COF3,VISC,0
FLDATA12,PROP,IVIS
FLDATA7,PROT,COND,CONSTANT
FLDATA8,NOMI,COND,-1,
FLDATA9,COF1,COND,0
FLDATA10,COF2,COND,0
FLDATA11,COF3,COND,0
FLDATA7,PROT,SPHT,CONSTANT
FLDATA8,NOMI,SPHT,-1,
FLDATA9,COF1,SPHT,0
FLDATA10,COF2,SPHT,0
FLDATA11,COF3,SPHT,0
TYPE,   1
MAT,
REAL,
ESYS,      0
SECNUM,
FLST,2,1,5,ORDE,1
FITEM,2,24
SFA,P51X, ,FSIN,1,
FLST,2,1,5,ORDE,1
FITEM,2,25
SFA,P51X, ,FSIN,2,
FLST,2,1,5,ORDE,1
FITEM,2,31
```

```
SFA,P51X, ,FSIN,3,
FLST,2,1,5,ORDE,1
FITEM,2,66
SFA,P51X, ,FSIN,4,
FLST,2,3,5,ORDE,3
FITEM,2,18
FITEM,2,23
FITEM,2,27
FLST,2,6,5,ORDE,6
FITEM,2,18
FITEM,2,23
FITEM,2,27
FITEM,2,53
FITEM,2,57
FITEM,2,61
DA,P51X,UX,0
FLST,2,3,5,ORDE,3
FITEM,2,60
FITEM,2,64
FITEM,2,67
/GO
DA,P51X,UY,0
FLST,2,5,5,ORDE,5
FITEM,2,28
FITEM,2,35
FITEM,2,42
FITEM,2,45
FITEM,2,56
FLST,2,28,5,ORDE,15
FITEM,2,1
FITEM,2,-15
FITEM,2,22
FITEM,2,26
FITEM,2,30
FITEM,2,34
FITEM,2,37
FITEM,2,41
FITEM,2,44
FITEM,2,48
FITEM,2,51
FITEM,2,55
FITEM,2,58
FITEM,2,62
FITEM,2,65
FLST,2,28,5,ORDE,15
FITEM,2,1
FITEM,2,-15
FITEM,2,22
FITEM,2,26
FITEM,2,30
FITEM,2,34
FITEM,2,37
FITEM,2,41
```

```
FITEM,2,44
FITEM,2,48
FITEM,2,51
FITEM,2,55
FITEM,2,58
FITEM,2,62
FITEM,2,65
DA,P51X,UZ,0
*DEL,_FNCNAME
*DEL,_FNCMTID
*SET,_FNCNAME,'load'
! /INPUT,altshpload.func
*DIM,%_FNCNAME%,TABLE,6,10,1
! Begin of equation: 0.005*cos(100*{PI}*{TIME})-0.005
*SET,%_FNCNAME%(0,0,1), 0.0, -999
*SET,%_FNCNAME%(2,0,1), 0.0
*SET,%_FNCNAME%(3,0,1), 0.0
*SET,%_FNCNAME%(4,0,1), 0.0
*SET,%_FNCNAME%(5,0,1), 0.0
*SET,%_FNCNAME%(6,0,1), 0.0
*SET,%_FNCNAME%(0,1,1), 1.0, -1, 0, 100, 0, 0, 0
*SET,%_FNCNAME%(0,2,1), 0.0, -2, 0, 3.14159265358979310, 0, 0, -1
*SET,%_FNCNAME%(0,3,1),   0, -3, 0, 1, -1, 3, -2
*SET,%_FNCNAME%(0,4,1), 0.0, -1, 0, 1, -3, 3, 1
*SET,%_FNCNAME%(0,5,1), 0.0, -1, 10, 1, -1, 0, 0
*SET,%_FNCNAME%(0,6,1), 0.0, -2, 0, 0.005, 0, 0, -1
*SET,%_FNCNAME%(0,7,1), 0.0, -3, 0, 1, -2, 3, -1
*SET,%_FNCNAME%(0,8,1), 0.0, -1, 0, 0.005, 0, 0, -3
*SET,%_FNCNAME%(0,9,1), 0.0, -2, 0, 1, -3, 2, -1
*SET,%_FNCNAME%(0,10,1), 0.0, 99, 0, 1, -2, 0, 0
! End of equation: 0.005*cos(100*{PI}*{TIME})-0.005
FLST,2,5,5,ORDE,5
FITEM,2,28
FITEM,2,35
FITEM,2,42
FITEM,2,45
FITEM,2,56
DA,P51X,UY, %LOAD%
FLST,5,4,4,ORDE,4
FITEM,5,42
FITEM,5,46
FITEM,5,108
FITEM,5,110
CM,_Y,LINE
LSEL, , , ,P51X
CM,_Y1,LINE
CMSEL,,_Y
LESIZE,_Y1, , ,4, , , , ,1
FLST,5,2,4,ORDE,2
FITEM,5,43
FITEM,5,118
CM,_Y,LINE
LSEL, , , ,P51X
```

```
CM,_Y1,LINE
CMSEL,,_Y
LESIZE,_Y1, , ,3, , , , ,1
FLST,5,2,4,ORDE,2
FITEM,5,38
FITEM,5,116
CM,_Y,LINE
LSEL, , , ,P51X
CM,_Y1,LINE
CMSEL,,_Y
LESIZE,_Y1, , ,7, , , , ,1
FLST,5,4,4,ORDE,4
FITEM,5,45
FITEM,5,47
FITEM,5,115
FITEM,5,117
CM,_Y,LINE
LSEL, , , ,P51X
CM,_Y1,LINE
CMSEL,,_Y
LESIZE,_Y1, , ,16,1.75, , , ,1
FLST,5,4,4,ORDE,4
FITEM,5,37
FITEM,5,44
FITEM,5,107
FITEM,5,109
CM,_Y,LINE
LSEL, , , ,P51X
CM,_Y1,LINE
CMSEL,,_Y
LESIZE,_Y1, , ,8, , , , ,1
FLST,5,7,4,ORDE,4
FITEM,5,111
FITEM,5,-114
FITEM,5,119
FITEM,5,-121
CM,_Y,LINE
LSEL, , , ,P51X
CM,_Y1,LINE
CMSEL,,_Y
LESIZE,_Y1, , ,48,.5, , , ,1
TYPE,   1
MAT,
REAL,
ESYS,       0
SECNUM,
FLST,5,2,6,ORDE,2
FITEM,5,15
FITEM,5,-16
CM,_Y,VOLU
VSEL, , , ,P51X
CM,_Y1,VOLU
CHKMSH,'VOLU'
```

```
CMSEL,S,_Y
VSWEEP,_Y1
CMDELE,_Y
CMDELE,_Y1
CMDELE,_Y2
MPTEMP,,,,,,,,
MPTEMP,1,0
MPDATA,EX,1,,2000.0
MPDATA,PRXY,1,,0.35
MPTEMP,,,,,,,,
MPTEMP,1,0
MPDATA,DENS,1,,1.1e-9
TB,HYPE,2,1,2,NEO
TBTEMP,0
TBDATA,,10.0,2e-4,,,,
MPTEMP,,,,,,,,
MPTEMP,1,0
MPDATA,DENS,2,,1.1e-9
FLST,5,8,4,ORDE,8
FITEM,5,3
FITEM,5,10
FITEM,5,16
FITEM,5,32
FITEM,5,72
FITEM,5,74
FITEM,5,77
FITEM,5,105
CM,_Y,LINE
LSEL, , , ,P51X
CM,_Y1,LINE
CMSEL,,_Y
LESIZE,_Y1, , ,4, , , , ,1
FLST,5,8,4,ORDE,8
FITEM,5,5
FITEM,5,8
FITEM,5,17
FITEM,5,33
FITEM,5,80
FITEM,5,82
FITEM,5,85
FITEM,5,102
CM,_Y,LINE
LSEL, , , ,P51X
CM,_Y1,LINE
CMSEL,,_Y
LESIZE,_Y1, , ,3, , , , ,1
FLST,5,8,4,ORDE,8
FITEM,5,19
FITEM,5,-20
FITEM,5,22
FITEM,5,34
FITEM,5,88
FITEM,5,90
```

```
FITEM,5,93
FITEM,5,97
CM,_Y,LINE
LSEL, , , ,P51X
CM,_Y1,LINE
CMSEL,,_Y
LESIZE,_Y1, , ,5, , , , ,1
FLST,5,6,4,ORDE,6
FITEM,5,2
FITEM,5,11
FITEM,5,31
FITEM,5,64
FITEM,5,66
FITEM,5,69
CM,_Y,LINE
LSEL, , , ,P51X
CM,_Y1,LINE
CMSEL,,_Y
LESIZE,_Y1, , ,1, , , , ,1
FLST,5,12,4,ORDE,11
FITEM,5,7
FITEM,5,9
FITEM,5,13
FITEM,5,-15
FITEM,5,23
FITEM,5,35
FITEM,5,48
FITEM,5,65
FITEM,5,73
FITEM,5,86
FITEM,5,89
CM,_Y,LINE
LSEL, , , ,P51X
CM,_Y1,LINE
CMSEL,,_Y
LESIZE,_Y1, , ,6, , , , ,1
FLST,5,12,4,ORDE,8
FITEM,5,24
FITEM,5,-29
FITEM,5,59
FITEM,5,61
FITEM,5,70
FITEM,5,78
FITEM,5,81
FITEM,5,94
CM,_Y,LINE
LSEL, , , ,P51X
CM,_Y1,LINE
CMSEL,,_Y
LESIZE,_Y1, , ,5, , , , ,1
FLST,5,8,4,ORDE,8
FITEM,5,1
FITEM,5,12
```

```
FITEM,5,30
FITEM,5,36
FITEM,5,40
FITEM,5,49
FITEM,5,55
FITEM,5,60
CM,_Y,LINE
LSEL, , , ,P51X
CM,_Y1,LINE
CMSEL,,_Y
LESIZE,_Y1, , ,3, , , , ,1
FLST,5,4,4,ORDE,4
FITEM,5,39
FITEM,5,41
FITEM,5,54
FITEM,5,56
CM,_Y,LINE
LSEL, , , ,P51X
CM,_Y1,LINE
CMSEL,,_Y
LESIZE,_Y1, , ,4, , , , ,1
FLST,5,8,4,ORDE,8
FITEM,5,4
FITEM,5,6
FITEM,5,18
FITEM,5,21
FITEM,5,96
FITEM,5,98
FITEM,5,101
FITEM,5,104
CM,_Y,LINE
LSEL, , , ,P51X
CM,_Y1,LINE
CMSEL,,_Y
LESIZE,_Y1, , ,20, , , , ,1
FLST,5,24,4,ORDE,22
FITEM,5,50
FITEM,5,-53
FITEM,5,57
FITEM,5,-58
FITEM,5,62
FITEM,5,-63
FITEM,5,67
FITEM,5,-68
FITEM,5,71
FITEM,5,75
FITEM,5,-76
FITEM,5,79
FITEM,5,83
FITEM,5,-84
FITEM,5,87
FITEM,5,91
FITEM,5,-92
```

```
FITEM,5,95
FITEM,5,99
FITEM,5,-100
FITEM,5,103
FITEM,5,106
CM,_Y,LINE
LSEL, , , ,P51X
CM,_Y1,LINE
CMSEL,,_Y
LESIZE,_Y1, , ,46, , , , ,1
TYPE,   2
MAT,      1
REAL,
ESYS,      0
SECNUM,
FLST,5,6,6,ORDE,6
FITEM,5,1
FITEM,5,-2
FITEM,5,4
FITEM,5,6
FITEM,5,9
FITEM,5,14
CM,_Y,VOLU
VSEL, , , ,P51X
CM,_Y1,VOLU
CHKMSH,'VOLU'
CMSEL,S,_Y
VSWEEP,_Y1
CMDELE,_Y
CMDELE,_Y1
CMDELE,_Y2
TYPE,   3
MAT,      2
REAL,
ESYS,      0
SECNUM,
FLST,5,8,6,ORDE,6
FITEM,5,3
FITEM,5,5
FITEM,5,7
FITEM,5,-8
FITEM,5,10
FITEM,5,-13
CM,_Y,VOLU
VSEL, , , ,P51X
CM,_Y1,VOLU
CHKMSH,'VOLU'
CMSEL,S,_Y
VSWEEP,_Y1
CMDELE,_Y
CMDELE,_Y1
CMDELE,_Y2
/UI,MESH,OFF
```

```
ALLSEL,ALL
FLST,3,2,6,ORDE,2
FITEM,3,15
FITEM,3,-16
VGEN, ,P51X, , ,1, , , , ,1
FINISH
/SOLU
ANTYPE,4
LUMPM,1
NLGEOM,1
TIME,0.03
DELTIM,0.00083333333333333333333,0,0
OUTRES,NSOL,ALL
OUTRES,STRS,ALL
OUTRES,RSOL,ALL
AUTOTS,0
FLDATA1,SOLU,TRAN,1
FLDATA1,SOLU,FLOW,1
FLDATA1,SOLU,TEMP,0
FLDATA1,SOLU,TURB,0
FLDATA1,SOLU,COMP,0
FLDATA1,SOLU,VOF,0
FLDATA1,SOLU,SFTS,0
FLDATA1,SOLU,IVSH,0
FLDATA1,SOLU,SWRL,0
FLDATA1,SOLU,SPEC,0
FLDATA1,SOLU,ALE,1
FLDATA,ALGR,SEGR,SIMPLEN
FLDATA25,RELX,VX,0.95
FLDATA25,RELX,VY,0.95
FLDATA25,RELX,VZ,0.95
FLDATA25,RELX,PRES,1.0
*SET,_z4,-999
*SET,_z14,1
FLDATA4,TIME,STEP,0.000833333333333333333333,
FLDATA4,TIME,ISTEP,0
FLDATA4,TIME,NUMB,36,
FLDATA4,TIME,TEND,1.0e06
FLDATA4,TIME,GLOB,60,
FLDATA4,TIME,VX,0.01,
FLDATA4,TIME,VY,0.01,
FLDATA4,TIME,VZ,0.01,
FLDATA4,TIME,PRES,1e-06,
FLDATA4,TIME,TEMP,1e-06,
FLDATA4,TIME,ENKE,0.01,
FLDATA4,TIME,ENDS,0.01,
FLDATA4A,STEP,OVER,0,
FLDATA4,TIME,OVER,0
FLDATA4A,STEP,APPE,0,
FLDATA4,TIME,APPE,1.0e6
FLDATA4A,STEP,SUMF,1,
FLDATA4,TIME,SUMF,1.0e6
FLDATA4,TIME,BC,0
```

```
FLDATA4,TIME,TEND,1000000,
FSAN,1
FSOR,SOLID
FSTR,FLUID,TRAN
FSTR,SOLID,TRAN
FSIN,CONS
FSTI,0.03,
FSDT,0.00083333333333333333333,
FSIT,125,
FSCO,UX,2.5e-5,
FSOU,1
FSCO,UY,2.5e-5,
FSOU,1
FSCO,UZ,2.5e-5,
FSOU,1
FSCO,FX,2.5e-5,
FSOU,1
FSCO,FY,2.5e-5,
FSOU,1
FSCO,FZ,2.5e-5,
FSOU,1
FSRE,ALL,0.10,
SAVE
SOLVE
SAVE
FINISH
```

VITA

David Matthew McCutcheon was born to Carl David and Darlene McCutcheon in Harrison, Arkansas on March 5, 1979. He attended high school in Mt. Judea, Arkansas until 1997 when he entered the Department of Mechanical Engineering at Arkansas Tech University. During the pursuit of his bachelor's degree, David held an internship at Dassault Falcon Jet. Upon graduation he worked as a co-op for Entergy at Arkansas Nuclear One in Russellville, Arkansas. He began research for his Master of Science degree with Dr. J.N. Reddy and Dr. Terry Creasy at Texas A&M University. David received his Bachelor of Science degree in Mechanical Engineering from Arkansas Tech University in December 2001 along with an Associate of Science degree in Nuclear Technology. He received his Master of Science in Mechanical Engineering from Texas A&M University in December 2004. David can be reached at HC 32 Box 288 Mt. Judea, Arkansas 72655.